UNIVERSITÀ
DEGLI STUDI
DI PADOVA

UNIVERSITA’ DEGLI STUDI DI PADOVA

**Dipartimento di Ingegneria Industriale DII**

Corso di Laurea Magistrale in Ingegneria Aerospaziale

# S-Duct Aerodynamics: Optical Distortion Correction Methods for the Application of Particle Image Velocimetry Techniques in Convoluted Aero Engine Intakes

Relatore: Prof. Ernesto Benini

Stefano Merlini, 1155551

Anno Accademico 2018/2019

# ABSTRACT

Nuovi velivoli altamente integrati richiedono un accoppiamento complesso tra la presa d'aria (Intake) e il fan del sistema propulsivo, rendendo necessario l'utilizzo di condotti dalle forme non convenzionali. La natura turbolenta del flusso aerodinamico e le instabilità generate da queste superfici possono condurre a separazione dello strato limite con conseguente riduzione delle performance generali del motore. L'attività sperimentale basata sul sistema S-PIV (Stereoscopic Particle Image Velocimetry) condotta all'Università di Cranfield ha come scopo lo studio dell'aerodinamica interna di sistemi di aspirazione avanzati per nuovi possibili aeromobili. Precedenti studi hanno dimostrato che queste superfici curve producono immagini distorte del piano di misura, costituendo la principale fonte di errore nella tecnica S-PIV.

Il seguente progetto di ricerca introduce un nuovo metodo di correzione delle distorsioni ottiche basato sull'identificazione di punti di calibrazione, insieme ad un'esaustiva analisi dell'impatto delle non linearità ottiche sull'accuratezza delle misure di velocità di un fluido subsonico. Dopo un iniziale sviluppo dell'algoritmo di riconoscimento di punti a partire da immagini sintetiche e da tecniche di post-produzione, una campagna di validazione viene definita sulla base di esempi di immagini distorte generate da modelli parametrici e simulazioni numeriche.

I risultati di questa analisi mostrano l'efficacia di questo metodo nel correggere correttamente immagini PIV affette da distorsioni ottiche locali, riducendo l'errore fino al 100% nelle misure del profilo di velocità del flusso. Inoltre, successive valutazioni sul campo di velocità a due e a tre componenti ha rivelato che errori dovuti ad effetti ottici in PIV sono maggiormente imputabili al processo di correlazione piuttosto che a quello di calibrazione.

Per concludere, l'analisi condotta su immagini reali ha dimostrato la capacità di questo metodo di poter essere utilizzato in condizioni sperimentali, permettendo l'impiego del sistema S-PIV nello studio aerodinamico di nuovi sistemi propulsivi altamente integrati.

**Keywords:** Feature identification, S-PIV, PIV Velocity Error, Optical distortion.

# ABSTRACT

Highly integrated aircraft architectures require advanced coupling between the intake and the fan which drives toward more complex and shorter intakes for novel propulsion systems architectures. The complex flow phenomena and the high unsteadiness introduced by convoluted inlet ducts can lead to intake flow separations and swirl distortions which compromise the performance of the downstream turbomachinery. The experimental facility based on Stereoscopic Particle Image Velocimetry has been successfully employed at Cranfield University to investigate the internal flow aerodynamics of unconventional intakes. Previous studies reveal that optical distortions are the major source of errors in the S-PIV measurements when imaging through transparent convoluted ducts.

In the present study an optical distortions correction method based on calibration markers identification was developed, including an assessment of the impact of optical non-linearities on the S-PIV measurements accuracy. First, the feature identification algorithm was created using image processing methodologies applied to synthetic calibration images. Then, the optical distortion correction pipeline was established and performance assessment analyses were conducted based on a range of different localised distorted synthetic PIV images, such as seeding particles and calibration target.

The results show the effectiveness of the method to successfully correct optical distortions on PIV images reducing the error by up to 100% in the flow field velocity profile. Furthermore, the assessment of the two and three components PIV velocity reveals that the errors introduced by optical non-linearities are mainly related to correlation bias rather than the calibration procedure.

Finally, the analysis on experimental calibration images proves the applicability of the general correction strategy in actual experimental conditions which can lead to new possible investigations in the research of internal complex intakes aerodynamics.

**Keywords:** Feature identification, S-PIV, PIV Velocity Error, Optical distortion.

# ACKNOWLEDGEMENTS

*I would like to express my gratitude to my supervisors, Dr. Pavlos Zachos and Prof. David MacManus for their advising and for giving me the chance to be part of the S-duct research group.*

*A special acknowledgment goes to Research Fellow Grant McLelland for his continuous support and guidance throughout the development of the project.*

*A sincere thank you to Associate Professor Ernesto Benini from University of Padova for the given opportunity to live this amazing experience.*

*A big thank you to all of the friends that I met this year, in particular I must acknowledge Miguel, Ernesto, Aitor and Alessia without them the year in Cranfield would not have been the same. A special acknowledgment goes to Maria. Thank you for all the patience and love that reserves me every day.*

*Finally, there are no words to describe the gratitude I ought to my parents, my sister Indira, my childhood friends and in general to all my family. Their unconditional love and support are the force that keeps me going.*

*Stefano Merlini*

*December 2019*

# TABLE OF CONTENTS

# LIST OF FIGURES

# LIST OF TABLES

# NOMENCLATURE

| **Roman symbols** | | **Units** |
|---|---|---|
| $a_{\max}$ | Maximum peak displacement | [px] |
| $a$ | Distortion amplitude | [px] |
| $c$ | Distortion extent | [px] |
| $D_{S-Duct.in}$ | S-Duct inlet diameter | [m] |
| $D_{S-Duct.out}$ | S-Duct outlet diameter | [m] |
| $\Delta z_0$ | Light sheet thickness | [m] |
| $F^c$ | Ideal mapping function for camera c | [-] |
| $\hat{F}^c$ | Estimation of mapping function for camera c | [-] |
| $f^{\#}$ | Camera lens aperture f-number | [-] |
| $Re$ | Reynolds number | [-] |
| $M$ | Mach number | [-] |
| $\vec{d}$ | Optical displacement vector | [px] |
| $\nabla\vec{d}$ | Optical displacement vector gradient | [px/px] |
| $\nabla^2 n$ | Second derivative of the refractive index | [-] |
| $M_n$ | Nominal Magnification factor | [-] |
| $n$ | Index of refraction | [-] |
| $N_i$ | Number of markers per calibration target | [-] |
| $N_{distorted}$ | Number of spurious vector (error>5%) distorted case | [-] |
| $N_{corrected}$ | Number of spurious vector (error>5%) corrected case | [-] |
| $N_{removed}$ | Number of spurious vector (error>5%) removed | [%] |

| **Greek symbols** | | **Units** |
|---|---|---|
| $\theta$ | Off axis angle | [rad] |
| $\phi$ | Scheimpflüg angle | [rad] |

| **Acronyms / Abbreviation** | | **Units** |
|---|---|---|
| 2-C Velocity | 2-Components velocity | [px] |
| 3-C Velocity | 3- Components velocity | [m/s] |
| BLI | Boundary Layer Ingestion | [-] |
| BOS | Background Oriented Schlieren | [-] |
| CFD | Computational Fluid Dynamics | [-] |
| DDES | Delay Detached Eddy Simulation | [-] |
| SIG | Synthetic Image Generator | [-] |
| AIP | Aerodynamic Interface Plane | [-] |
| S-PIV | Stereoscopic Particle Image Velocimetry | [-] |
| PIV | Particle Image Velocimetry | [-] |
| PTV | Particle Tracking Velocimetry | [-] |
| ROI | Region of Interest | [-] |
| CMOS | Complementary Metal-Oxide Semiconductor | [-] |
| FFT | Fast Fourier Transform | [-] |
| FT | Fourier Transform | [-] |
| $FT^{-1}$ | Inverse Fourier Transform | [-] |
| LDV | Laser Doppler Velocimetry | [-] |
| MIR | Matched Index of Refraction | [-] |
| OpenCV | Open Source Computer Vision | [-] |
| DPE | Dot Position Error | [px] |
| Max Dist. | Maximum distortion | [px] |
| RGB | Red Green Blue image format | [-] |
| FWHM | Full-Width at Half-Maximum | [-] |
| PMMA | Poly (Methyl methacrylate) | |

# 1 Introduction

## 1.1 Background and Context

The strong interest towards more efficient and reliable propulsion engine systems is the primary driver of the experimental research in the field of convoluted aero engine intake aerodynamics. Previous studies have successfully demonstrated that these new configurations, such as Boundary-layer ingestion (BLI) and Distributed Electric Propulsion, are potentially able to ensure a substantial reduction in specific fuel consumption and an increase in propulsive efficiency by producing thrust from the reduced velocity boundary layer air [1]. In this context, the coupling between the intake and fan becomes a critical aspect of the design. Semi-immersed propulsion architectures are susceptible to intake flow distortion which can compromise the performance of the downstream turbomachinery [2]. As a result, the propulsion system integration has arisen lots of attention in several applications, seeking to counter these effects.

A possible concept for embedded propulsion systems is the S-duct shaped intakes which have showed potential benefits in both military and commercial sector. S-duct intakes lead to design more compact vehicles which are preferable for both transport and combat applications where specific requirements such as low noise, low fuel consumption and high cruise performance are desirable. Depending on geometrical characteristics of the duct, the flow is likely to separate and secondary flow effects dominate the outlet air stream, causing total pressure losses and unsteadiness. Understanding how all of that affects the engine operation, several experimental and computational studies have been conducted, outlining the mechanisms that are involved in this complex internal aerodynamics and the overall flow properties downstream.

The S-Duct experimental facility, set-up in Cranfield University, has been built for this purpose, integrating stereo particle image velocimetry (S-PIV) techniques for flow velocity measurements at the exit plane of S-duct type intakes. High-spatial resolution, synchronous data across the aerodynamic interface plane (AIP) and capability to characterising complex swirl distortions are the key benefits of PIV which represents a more accurate and suitable solution towards a full comprehension of the flow dynamics for this case study than traditional high bandwidth intrusive approaches (i.e. fast response probes, hot-wire anemometry).

Previous work has shown the successful application of using this method to measure the flow field [2], however, the method was found susceptible to uncertainties caused by the non-planar optical boundaries that introduce optical distortion to the particle images compromising the capability of the image processing algorithms to reconstruct the velocity vector map across the measurement plane. Non-intrusive measuring techniques need an optical access to the region of interest; therefore, optical windows must be included in the work section. This aspect affects negatively the accuracy of the results due to optical phenomena that take place when the light passes through a transparent medium, especially, in the condition of high curved geometry. This issue was largely recognised by previous studies, [3], [4] and its impact on the velocity measurements was recorded to be significantly high close to the boundaries [5].

In the last two years, the attention has moved to quantify the uncertainty magnitude on the S-PIV results and develop possible strategies to mitigate optical distortion effects by both hardware and software approach [6], however, a definitive solution that exploits the problem is still not available.

## 1.2 Aims and Objectives

The influence of optical distortions in the PIV measurements accuracy has been recognised as a critical aspect of experimental activities when imaging through a transparent window [4]. As aforementioned in §1.1, the outcome of the particle image velocimetry analysis is strongly related with the capability of the acquisition systems to produce clean images which are not affected by optical phenomena, such as optical aberrations. Geometrical warping and perspective distortion of the images occurring in the stereoscopic configurations are partially corrected by the calibration process which is able to deal with moderate level of distortions [6]. By contrast, manufacturing imperfections and high curved working sections can introduce aggressive local and global deformations as increasing the complexity of the transparent medium ducts, therefore, different approaches should be developed to compensate and correct these effects.

The project aims to develop an effective optical distortion correction method based on feature identification algorithms which are able to remove optical distortions from PIV calibration and seeding particles images.

The main objectives of the study are reported as follow:

- Develop and fully assess the correction method through both synthetic and experimental distorted calibration images.
- Quantify the impact of local optical distortions on PIV velocity profiles when non-planar optical sections are employed and provide an exhaustive view of the correction method effectiveness in the PIV velocity error.

The study involves a range of various distorted calibration images generated synthetically by assuming a 2-D Gaussian distortion model which simulates local optical non-linearities due to for example manufacturing imperfections of the surfaces. Moreover, the proof-of-concept will be assessed by considering real experimental calibration images taken from tubular working sections in the S-PIV experimental facility.

The final outcome is a pre-processing method which is able to correct optical distortion on S-PIV images before undertaken conventional particles image velocimetry software (e.g. TSI Insight 4G$^{TM}$), so It is envisaged that this tool will become part of the standard PIV image processing workflows. As part of the work to provide also a general overview of the effects induced by optical phenomena on PIV techniques, looking at both image and object planes velocity flow field.

## 1.3 Thesis overview

A brief description of the current work content is provided in this section. In general, the thesis is structured following the same line of thought assumed during the project investigation.

More specifically, *Chapter 1* introduces the rationale behind this study as well as the definition of the problem which is proposed to solve, along with the relative Aims and Objectives.

In *Chapter 2*, the literature survey related to the project purposes is presented. As first, a short description of the Particle Image Velocimetry technique is discussed, including principles and typical configurations of the measuring system with more emphasis on the S-PIV and relative calibration procedure. In the last part of the survey, an overview of optical distortions on PIV is given, along with an analytical model of the relative error on the velocity measurements and established mitigation strategies.

A detailed description of the methodology applied to achieve the aims and objectives of this project is presented in *Chapter 3.* In particular, the two approaches, Synthetic and Experimental, adopted to generate the test cases are described as first, followed by the description of the established correction pipeline. To conclude, the error statistics considered to evaluate the effectiveness of the method are defined.

*Chapter 4* presents the results and discussion of the analysis conducted by performing the correction method on synthetic PIV images. Separate sections are dedicated for the performance assessment based on calibration target images and PIV velocity profiles, including a discussion about the impact of optical distortions on the PIV velocity error. The conclusions of the synthetic study are also provided as last.

In Chapter 5 the proof-of-concept of the developed correction method on experimental calibration target images is presented along with the relative conclusions.

Finally, an exhaustive project summary is given in the last part of the thesis, including a possible future research.

# 2 Literature Review

*It is an important part of experimental research to quantify the level of uncertainties in measurements and propose alternative strategies to increase the accuracy of the measuring techniques. In these terms, quantification of uncertainties in experimental data is a vast scientific field and many different design factors and phenomena contribute to increase the complexity of the error analysis and the associated evaluation uncertainties process. In the case of particles image velocimetry, optical distortion can represent an important source of errors in the reconstructed velocity field, especially, when it is applied for internal flows studies. In this chapter, the necessary theory and background of the PIV technique are given, highlighting the main contributors to measurement uncertainty. Furthermore, a brief discussion of principals of optics in the field of image distortion will be provided, including also recent optical distortion compensation approaches specifically for PIV. Finally, challenges and limitations involved in these experimental campaigns will be discussed as well as de-warping image strategies derived from another field of research.*

## 2.1 Particle image velocimetry (PIV)

In this section, the general concept of particles image velocimetry is presented. Firstly, the introduction of principle and theory of the technique is described, referring particularly on stereoscopic configurations. A short description of the main causes of errors in the PIV measurements is also included, however, the reader should refer to [7], [8] and [9] for an exhaustive view of the topics proposed.

## 2.1.1 Principles of PIV

In the last 20 years, progress in optics, electronics, lasers, video and computer techniques permit the particles image velocimetry concept to become an advanced quantitative technique even though its physic principles have been used as qualitative flow visualisation setup since the early Prandtl's flows studies in 1900.

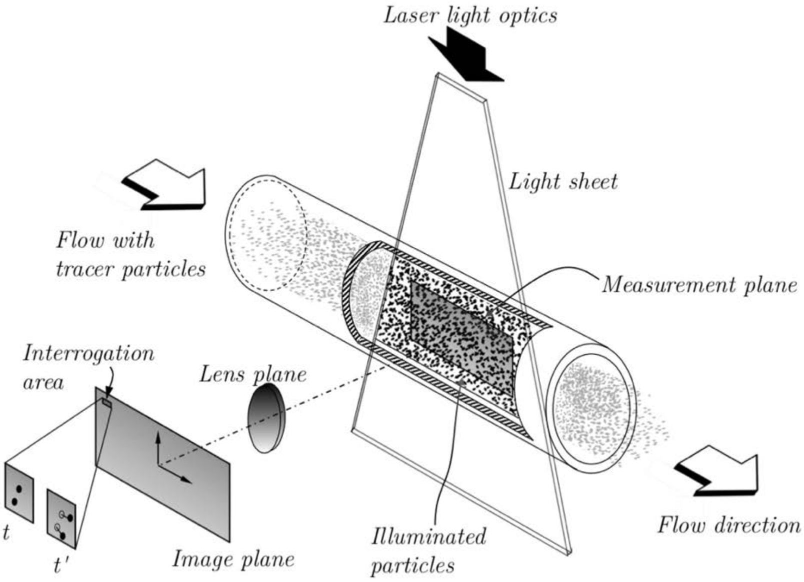

**Figure 2.1:** Typical Particle Image Velocimetry setup [6].

The typical PIV experimental system consists of several subsystems and each of them deals with a specific operation in the measurement workflow. PIV method is a non-intrusive optical measuring technique which allows recording the displacement of the particles in the flow domain and derive the associated fluid velocity. In general, tracer particles are added to the flow through a settling chamber in order to achieve a uniform particles distribution [10].

The particles are illuminated by a light source, i.e. laser light, in the flow domain and at least two pulses within a short time interval $\Delta t$ are required. The thin light sheet is formed by using several optical components, which define the measurement plane. The light scattered by the particles is recorded by at least one camera which produces image frames ready to be processed. Nowadays, high resolution digital cameras are used. The illumination pulse and the image recording system have to be synchronised, accordingly with the experiment and the flow velocities investigated. Recent laser devices and digital cameras are able to acquire flow measurements with a sampling rate of kHz.

The flow velocity is deduced indirectly by knowing the position of the particles in each frame and since the duration between the light pulses, $\Delta t = t - t'$, is known. There are different approaches that allow to derive the displacement of the particles, such as individual particles tracking implemented in PTV (Particles Tracking Velocimetry) [7], however, for the classical PIV technique, statistical methods are used to evaluate the particles movement. Farther details about particles displacement are discussed in §2.1.3.

A conventional PIV system is shown in Figure 2.1, where the optical axis of the image recording device is perpendicular to the working section. The laser sheet defined the measurement plane which axis is positioned in the longitudinal direction, accordingly with the particles stream and normal to the optical axis. It is important to highlight that the monoscopic set-up can only resolve two-dimensional flows, due to lack of information in the third dimension. Essentially, in the case of a single view, the out-of-plane component is projected on to the object plane, causing a perspective error in the in-plane measurement.

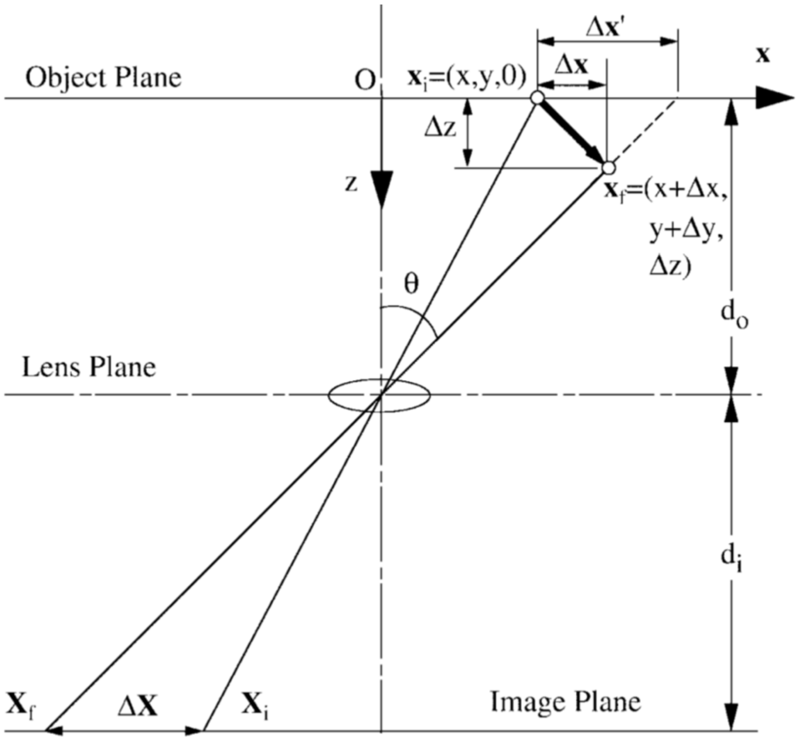

**Figure 2.2:** Error in the measurement of the in-plane component due to the out-of-plane motion [11].

The aforementioned error for the case of planar PIV configurations is illustrated in Figure 2.2. A particle with the initial position $x_i$ that moves out-of-plane until the final position $x_f$ forms an image at $X_i$ and the correspondent final location $X_f$. It is noticeable that the apparent displacement identified as $\Delta x'$ and $\Delta y'$ defer largely from the actual motion of the particle $\Delta x$ and $\Delta y$. The relative error between the displacement in the object plane and the image plane, $\varepsilon$, is called perspective error, which is function of the out-of-plane position $\Delta z$ [11]. This error can have a significantly impact on the in-plane measurements, therefore, Stereoscopic PIV configurations is usually employed in the recent experimental facilities which is able to successfully eliminate this problem as well as reconstruct the whole 3-D velocity flow field.

### 2.1.2 Velocity reconstruction

The reconstruction of the three-dimensional velocity vector from the two planar images of particles displacement involves as a first step, statistical operations which allow deriving the two-dimensional vectors describing the particles motion in two consecutive frames at time $t$ and $t + \Delta t$. This processing step is referred as PIV analysis or PIV Evaluation and an exhaustive explanation of this topic is presented in [8]. Essentially, PIV analysis consists to divide the entire region of interest, for both frames, in sub-regions commonly called *interrogation windows*. For each of them, spatial average image light intensity field is calculated by summing the contribute of the individual particles and the comparison between one frame and the following one is performed. The matching procedure is conducted by mean of a crass-correlation analysis, employing efficient Fast Fourier Transform (FFT) algorithms. The final outcome of the PIV evaluation is a dataset of the displacement of the particles after $\Delta t$ time period in form of 2-D vectors in the image domains.

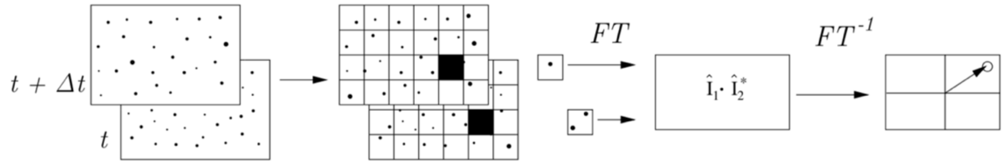

**Figure 2.3:** Cross-correlation method for double frame/single exposure recording. FT Fourier Transform, FT$^{-1}$ inverse Fourier Transform [8].

In stereoscopic PIV configurations, the cameras are individually interrogated using the aforementioned analysis. Now, the two velocity fields must be combined in order to obtain the 3-D velocity field by mapping these vectors from each image domain to the single object plane. This process is referred to as velocity reconstruction. Mainly, there are two different way to do it: the first one is known as geometric back-projection reconstruction which involves the pinhole camera model and accurate geometrical parameters of the system configuration [7], while the second one is a calibration procedure based on image processing of specific targets. Nowadays, the latter is broadly used thanks to its general formulation and no setup knowledge is required, moreover, perspective distortions and other optical phenomena occurring in the stereoscopic PIV configuration are partially removed employing calibration processes.

There are two types of calibration, namely 2D and 3D calibration methods. In the case of 2D calibration, information about the experimental configuration are still needed, so in S-PIV experiments 3D calibration procedure is commonly recognised as the most suitable option. More details about 3D calibration procedure in S-PIV technique are presented in §2.2.1, as it is the calibration method referred in the present work, highlighting the limitation of the method when applied in the condition of high level of distortion.

## 2.2 Stereoscopic PIV (S-PIV)

Stereoscopic configurations are based on two different cameras located in distinct off-axis views of the same region of interest. These two devices record simultaneously different points of view of the measurement plane, allowing to reconstruct the particles movement with all velocity components. Moreover, as already mentioned in §2.1.1, stereo vision contributes to eliminating the source of errors in the in-plane measurements due to out-of-plane particles movement. Stereoscopic PIV is commonly classified into two categories: Translational systems (lateral displacement) and Rotational systems (angular displacement). Typical stereoscopic configurations are shown in Figure 2.4.

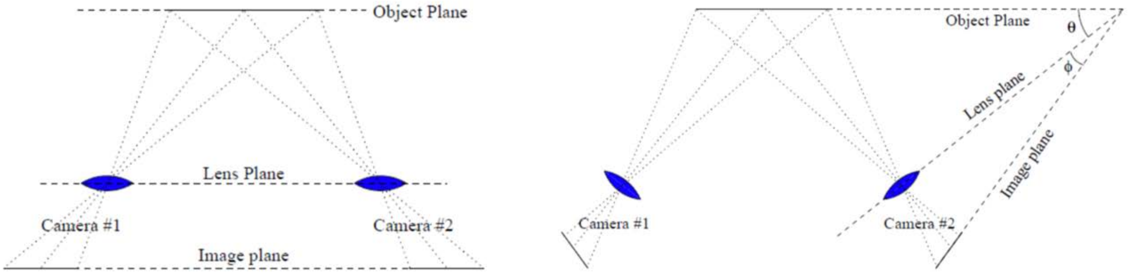

(a) Translational System (b) Rotational System

**Figure 2.4:** Typical stereoscopic PIV arrangement [12].

Translational configurations are simpler than the rotational ones, since the two cameras are placed on the same plane and parallel to each other, so uniform magnification factor, defined as $M_n = d_i/d_o$, is achievable [13]. Furthermore, the quality of the images is not compromised in absence of refractive-index changings along the optical paths and image focus is ensured without reducing the aperture of the cameras. The main drawback of this configuration is that there is an upper limit of the possible distance between the lenses, beyond that the lens performance degrades as well as the image quality. In particular, it has been demonstrated that the relative error out-of-plane decreases as increasing the off-axis angle $\theta$ [11].

Rotational systems are employed in order to remove the restriction on $\theta$ imposed by the translational arrangement. Now the angle $\theta$ can be increased without incurring issues related to lens performance, thereby providing better accuracy in the out-of-plane component. By contrast, difficulties associated with non-uniform magnification and image focus occur in this kind of set-up. A good focus on the whole image is ensured by rotating the image plane of an angle $\phi$ (Figure 2.4) from the lens plane, up to the point of collinear placement between image, lens and object planes. This requirement is known as Scheimpflüg condition and an example of this configuration in stereoscopic PIV is illustrated in Figure 2.5 [14].

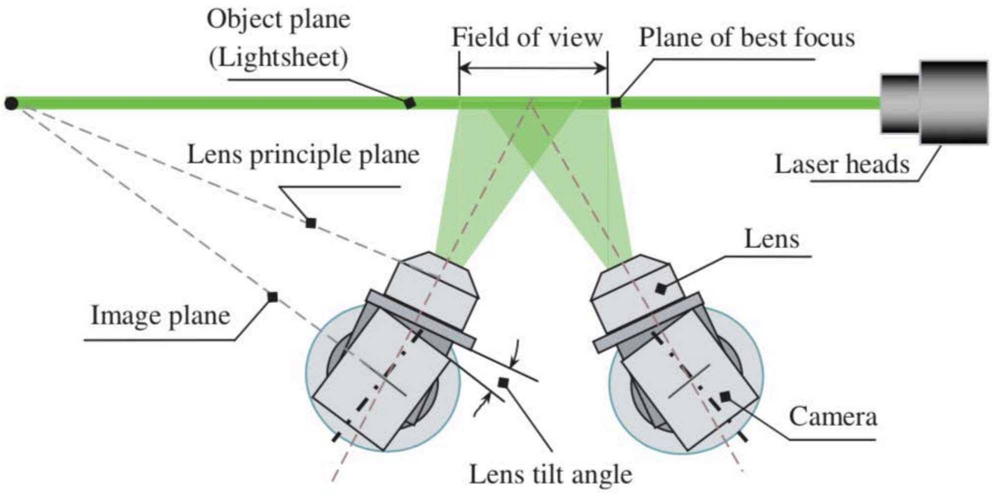

**Figure 2.5:** Scheimpflüg Stereoscopic PIV configuration [14].

By tilting the lens principal plane and the image plane, the best focus is achieved, however, this configuration introduces perspective distortions due to the camera inclination, therefore, correction methods are needed to recover the distorted image before undertaking the PIV analysis. Calibration procedures were found to be the best method which addresses this problem. Furthermore, no additional information is necessary to reconstruct the velocity field base on planar images of particles displacement. In the §2.2.1, calibration process and associated object plane reconstruction procedure in S-PIV technique will be presented.

### 2.2.1 Stereoscopic Calibration

Principles of the stereoscopic calibration method employed in Cranfield S-PIV facility is described in ref. [3] and will be now summarised.

The method proposed by Soloff was introduced as a distortion compensation technique for general S-PIV application, when imaging through refractive media. As mentioned in §2.1.3, calibration-based reconstruction maps the points from the 3D object domain to the 2D image domains for each camera. The solution presented here, introduces two non-linear vectorial mapping functions $\boldsymbol{F}^{(1)}(x,y,z,)$ and $\boldsymbol{F}^{(2)}(x,y,z,)$ for camera 1 and 2, respectively, that define the relation between the object and the image plane for both coordinates $X^{(c)} = F_1^{(c)}$ and $Y^c = F_2^{(c)}$.

A typical calibration process consists to use a calibration target with markers points at known locations positioned in the region of interest and aligned to the laser light sheet. By recording the positions of the markers in the calibration plate and since the actual positions of the target points are known, the analytical estimation of the mapping functions can be derived by finding the function that minimises the mean absolute error as defined in Eq. (2.1):

$$MAE = \frac{1}{N_i}\sum_{i}^{N_i}\left|\boldsymbol{F}^{(c)}(\boldsymbol{x}_i) - \widehat{\boldsymbol{F}}^{(c)}(\boldsymbol{x}_i)\right| \tag{2.1}$$

Where $N_i$ is the number of calibration markers within the target plate, $\boldsymbol{x}_i$ represents their coordinates vector in the physical domain and $\widehat{\boldsymbol{F}}^{(c)}$ is the estimation of vectorial mapping function. The augmented form of the non-linear transformation is reported here:

$$\begin{pmatrix} \Delta X^1 \\ \Delta Y^1 \\ \Delta X^2 \\ \Delta Y^2 \end{pmatrix} = \begin{pmatrix} \frac{\partial F_1^{(1)}}{\partial x} & \frac{\partial F_1^{(1)}}{\partial y} & \frac{\partial F_1^{(1)}}{\partial z} \\ \frac{\partial F_2^1}{\partial x} & \frac{\partial F_2^1}{\partial y} & \frac{\partial F_2^1}{\partial z} \\ \frac{\partial F_1^{(2)}}{\partial x} & \frac{\partial F_1^{(2)}}{\partial y} & \frac{\partial F_1^{(2)}}{\partial z} \\ \frac{\partial F_2^{(2)}}{\partial x} & \frac{\partial F_2^{(2)}}{\partial y} & \frac{\partial F_2^{(2)}}{\partial z} \end{pmatrix} \begin{pmatrix} \Delta x \\ \Delta y \\ \Delta z \end{pmatrix} \tag{2.2}$$

The elements of the matrix are the partial derivatives of the mapping functions of each camera, (1) and (2), which are estimated by the calibration procedure. It is worth to underline that these partial derivatives represent the gradient of particle image displacements to particle fluid displacements [3] that gives an indication of how the magnification changes in the actual domain. In general, third order of polynomial equations is employed in this process, revealing acceptable performance in terms of velocity reconstruction and distortion recovery [5].

Once the mapping functions of each camera have been found, the inverse procedure can be applied from the image plane to the object plane:

$$\boldsymbol{x}^{(c)} = \widehat{\boldsymbol{F}}^{(c)^{-1}}\left(F_1^{(c)}, F_2^{(c)}\right) \tag{2.3}$$

This procedure is called de-warping. Having applied the de-warping to the images, the velocity reconstruction is possible. For more details about velocity reconstruction procedure refer to [5] and [8].

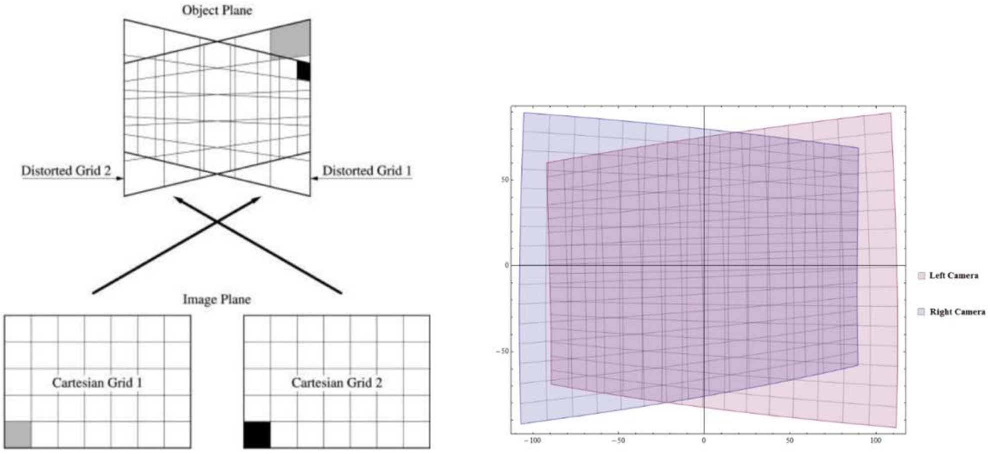

**Figure 2.6:** Effect of the prospective distortions on two Cartesian Grids (Left) and back projection process into the object domain by using mapping functions (Right) [11].

Several errors in the PIV measurements can be related to the calibration process when optical distortions deteriorate the calibration images, which are usually referred to as miss-registration errors. These errors are mainly caused by the misalignment of the laser sheet with the calibration plate and the mapping functions used to pass from the object space to the image plane [5]. Even though, previous studies have been demonstrated that optical distortions increase miss-registration errors in the PIV measurements, the 3-D calibration procedure has been found to deal partially with optical phenomena such as lens aberrations, astigmatism and coma that can be causes of image distortions and consequently the source of uncertainties in the reconstructed velocity measurements [3].

## 2.3 Optical distortions on PIV

The problem to apply non-intrusive optical technique through inhomogeneous media was raised since the early applications in transonic [15] and supersonic flows [16]. Optical distortions of the imaging process occur when the illuminated particles are observed through a transparent window which can result in deformations and blur of the particle image pattern. In relation to PIV techniques, three forms of error have been identified in previous works: position error, velocity error and particle image blur [17].

The first two errors are direct consequence of the displacement of the wrong particles due to stretches and gradients in the images while the latter one affects mainly the tracking precision of the correlation peak width due to the anisotropic increase of particle size which compromises the cross-correlation accuracy. For the purpose of this study, more emphasis is given to the position and velocity error since are related to geometrical distortion of the image rather than the blur effects which will not be included in the generation of the distorted images. In this context, an optical model of the position error has been proposed in [17] and here described in details, including the relative expression of the velocity error obtained by spatial differentiation of the position error.

### 2.3.1 Optical error model

One of the main contributors to the image distortion is the non-uniform refractive index spatial distribution. In simple terms, the light rays coming from particles in the measurement plane are refracted by inhomogeneous refractive index field, creating an apparent image particle $x'_p(t)$ in the image plane (Figure 2.7). Based on that, the error introduced in the PIV measurements due to optical deformations can be related to the refractive index spatial distribution between the PIV object plane and the image domain. In order to distinguish the effect of different sources of error, some assumptions are required in the derivation of the model.

The imaging system is considered ideal as well as the tracking process which means that the time averaging error on the velocity and pixelization effects are neglected, assuming small the time separation between exposures. Moreover, the average effect of the finite window size is assumed null and the velocity considered in this analysis is that of the particle, bearing in mind that this may not coincide with the flow velocity due to particle lag. In terms of flow field properties, steady condition is assumed which ensures that the particle velocity $\overrightarrow{V_P}$ and the image distortion depend only on the spatial location in the image plane. For simplicity, magnification factors are ignored imposing a one-to-one correspondence between the recorded plane and the plane of the focus.

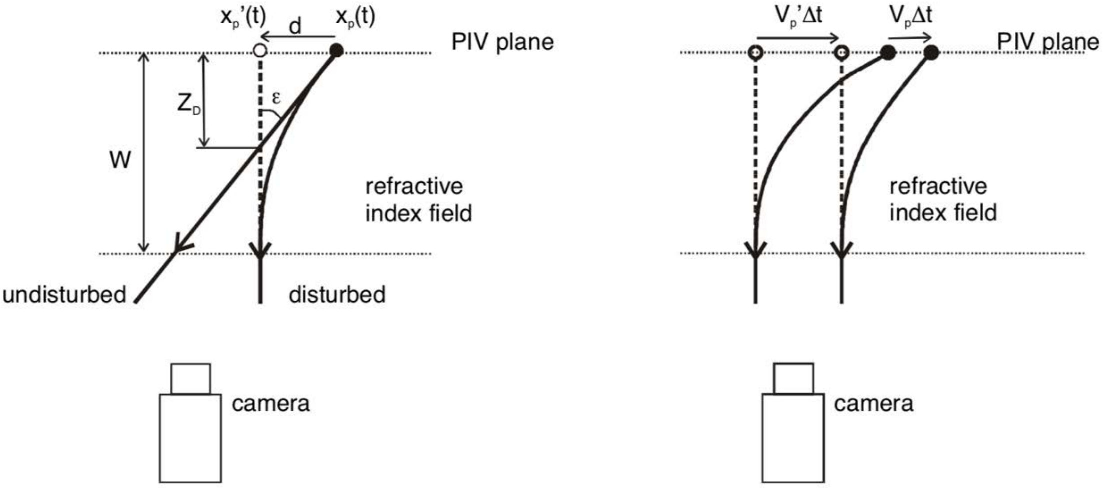

**Figure 2.7:** Position error (left) and direct velocity error (right) due to optical distortion on PIV techniques. Solid lines represent the light ray trajectories coming from the actual particle location (black dot). The backward extension of the light rays deriving from the imaged particle position (white dot) [17].

Figure 2.7 depicts in simple terms the light ray trajectories when a refractive index field is introduced between the image plane and the PIV plane. It can be noticed that the particle position perceived by the imaging system is the backward extension of the disturbed light ray propagating through an inhomogeneous refractive index field (dashed line) which does not coincide with the undisturbed light ray (propagating through a homogeneous refractive index field). Looking at the particle positions in the PIV plane, an evident spatial displacement appears between the actual position of the particle (black dot) and the imaged particle position (white dot) which is referred as the position error. The direct correspondent velocity error is shown in Figure 2.7 (right) where a single particle at two different exposures is depicted. Due to the initial position error, an error occurs in the image plane when the particle velocity is measured.

### 2.3.1.1 Position error

Based on the model illustrated above, the image distortion can be expressed as an optical displacement vector $\vec{d}(\vec{x})$:

$$\vec{d}(\overrightarrow{x_P}(t)) = \overrightarrow{x_P'}(t) - \overrightarrow{x_P}(t) \tag{2.4}$$

Where $\overrightarrow{x_P'}(t)$ and $\overrightarrow{x_P}(t)$ are respectively the exact particle position $(x, y)$ and the location perceived by the camera in the PIV plane. Applying the principles of Background Oriented Schlieren (BOS) technique presented in [18], the optical displacement vector can be directly related to the gradient of the refractive index $\nabla n$. In general, the refractive index gradient depends on the spatial component along the optical axis orthogonal to the PIV measurement plane, however, this dependency can be neglected by assuming 2-Dimensional flow which permits to derive the following simplified expression:

$$\vec{d}(\vec{x}) = -Z_D \int_0^W \nabla n(\vec{x}) dz = -Z_D W \nabla n(\vec{x}) = -\frac{1}{2} W^2 \nabla n(\vec{x}) \tag{2.5}$$

Where $W$ is the length of the light path through the refractive index field in the z axis which for PIV represents the distance between the measurement plane and the transparent window and $Z_D$ is the distance parallel to the optical axis obtained by the PIV plane and the intersection between the disturbed ($\nabla n \neq 0$) and undisturbed light rays ($\nabla n = 0$) illustrated in Figure 2.7 (left). According to the theory, the refractive index depends on the density $\rho$ [18].

### 2.3.1.2 Velocity error

As already stated above, the velocity error can be derived directly from the expression of the position error by spatial differentiation. Considering the Lagrangian expression of the particle velocity, the actual velocity is defined as:

$$\overrightarrow{V_P}\big(\overrightarrow{x_P}(t)\big) = \frac{d\overrightarrow{x_P}(t)}{dt} \tag{2.6}$$

In the same way, the measured velocity can be expressed as:

$$\overrightarrow{V_P'}\left(\overrightarrow{x_P'}(t)\right) = \frac{d\overrightarrow{x_P'}(t)}{dt} \tag{2.7}$$

It is important to highlight that the time interval between two exposures is finite in the case of PIV techniques which may introduce differences when comparing the measured velocity and the instantaneous one. In this case the assumption of short time interval $\Delta t$ ensures that these discrepancies are negligible.

Now, the velocity error is defined simply as the difference between the actual and the measured velocity at the location $\vec{x}$ in the image plane:

$$\Delta\overrightarrow{V_P}(t) = \overrightarrow{V_P'}(\vec{x}) - \overrightarrow{V_P}(\vec{x}) = \left\{\frac{d\overrightarrow{x_P'}(t)}{dt} - \frac{d\overrightarrow{x_P}(t)}{dt}\right\} + \frac{\partial\overrightarrow{V_P}}{\partial\vec{x}}\left(\overrightarrow{x_P}(t) - \overrightarrow{x_P'}(t)\right) \tag{2.8}$$

Substituting the Eq. 2.1 and further evaluation yields:

$$\Delta\overrightarrow{V_P}(t) = \frac{d\vec{d}(\vec{x}(t))}{dt} - \frac{\partial\overrightarrow{V_P}}{\partial\vec{x}}\vec{d}(\vec{x}) = \frac{\partial\vec{d}}{\partial\vec{x}}\overrightarrow{V_P}(\vec{x}) - \frac{\partial\overrightarrow{V_P}}{\partial\vec{x}}\vec{d}(\vec{x}) = \left(\nabla\vec{d}\right)\overrightarrow{V_P} - \left(\nabla\overrightarrow{V_P}\right)\vec{d} \tag{2.9}$$

Looking at the derived equation, it can be noticed that two factors contribute to the total velocity error. The first term represents the direct velocity error illustrated in Figure 2.7 (right) which is given by the product of the gradient of the optical displacement vector with the exact particle velocity. This represents a local change in the optical magnification, which results in a stretch of the image length scales relative to the physical scale domain. The second term. Instead, is the contribution of the position error to the velocity error. Note that only the derivative of the optical displacement vector taken in the direction of the velocity vector contributes to the first term of the velocity error which is proportional to the refractive index gradient as:

$$\nabla\vec{d}(\vec{x}) = -\frac{1}{2}W^2\frac{\partial\nabla n(\vec{x})}{\partial\vec{x}} = -\frac{1}{2}W^2\,\nabla^2 n(\vec{x}) \tag{2.10}$$

From the analytical expressions derived in this section, it can be concluded that the PIV error introduced by optical distortions when imaging through an inhomogeneous medium, such as transparent windows, depends mainly on the gradient and the second derivative of the refractive index which leads to identify the velocity error as the major source of systematic error (bias) in the PIV measurements, according to the [17].

#### 2.3.1.3 Particle image blur

Another effect of optical non-linearities in the seeding particle images is the image blur which is a stretch of the image length scales relative to the physical length scales in the object plane. This magnification of the image length scales is driven mainly by the second derivative of the refractive index as the direct velocity error described above, however, particle image blur has been demonstrated to become visible only for very large optical displacement gradient. Considering a particle diameter of 1 $\mu m$ and a diffraction spot of 20 $\mu m$, an optical displacement vector gradient of $\nabla\vec{d} = 0.1\ \frac{pixels}{pixel}$ introduces a 10% change of the particle size to $1.1\ \mu m$ which resulting in an imaged particle size of $20.1\ \mu m$ that cannot be directly identified as particle image blur. It can be concluded that before particle image blur is distinguishable in the PIV recordings, significant velocity error due to optical distortions may occur before, classifying the image blur as a secondary order effect.

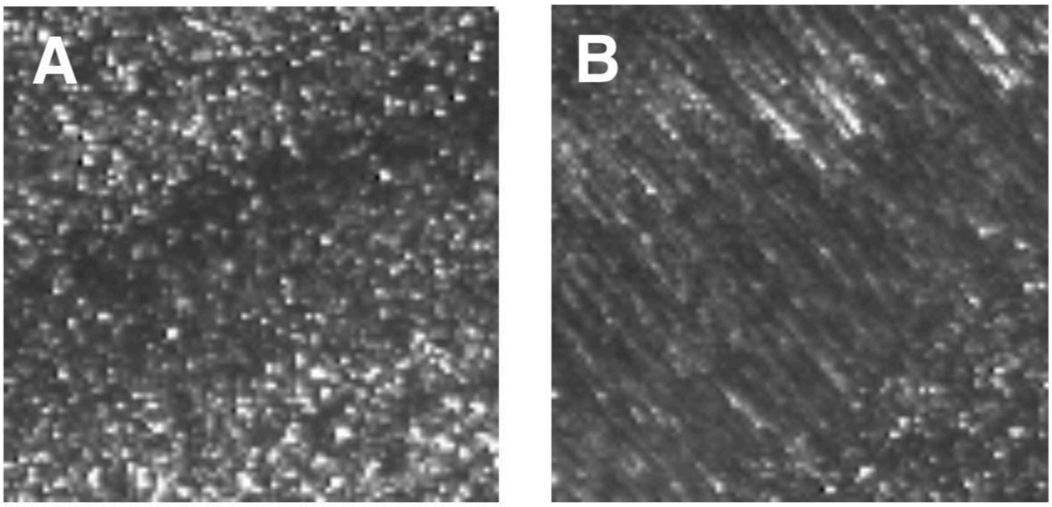

**Figure 2.8:** Effect of image blur on seeding particle images due to optical distortion in a 2D supersonic flow across an oblique shock wave [17].

## 2.3.2 Non-intrusive optical measuring techniques considerations

In this section, relevant optical distortion research and compensation strategies for non-intrusive optical measuring techniques are described, providing an overview of how researcher have approached this problem.

Several methods have been developed in order to mitigate optical phenomena in PIV measurements and most of them mainly operating on the optical access of the region of interest. In particular, lots of research has been conducted in the topic of optical distortion compensation techniques employing interfaces, such as liquid prisms as reported in [19] or external surfaces, that counters the effect of the duct refractive index (MIR) [20], [21]. As already widely discussed above, inhomogeneous refractive index field between the measurement plane and the camera is the primary cause of image distortions which depends on the material of the access window. Another design parameter that helps to reduce image deformation is the thickness of the working sections. Reduction of the working section thickness leads to lower level of light refraction as well as the distortion. This approach was applied from a number of researchers in Laser Doppler velocimetry (LDV) experiments, where thin glass working sections were introduced [22].

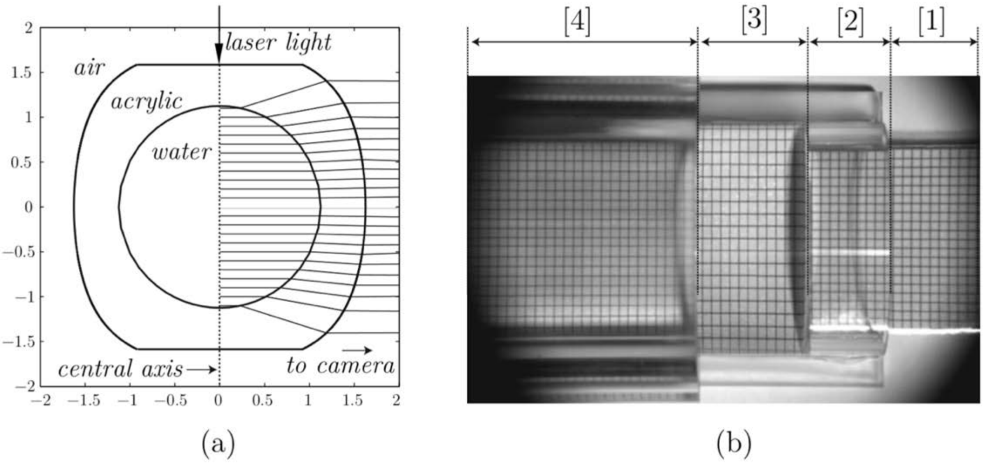

(a) (b)

**Figure 2.9:** (a) Ray tracing technique through a contoured interface made of acrylic. (b) optical distortion on uniform square grid due to: 1) Air interface, 2) Air+Acrylic half-pipe interface, 3) Air+Acrylic half-pipe + water interface, 4) Air+Acrylic contoured surface + water interface [23].

The technique, although promising, shows not suitable for high pressure flows due to the thin boundaries, limiting its application. All of these methods operate to improve the quality of the images, reducing the level of distortion and consequently increase the measurements accuracy. Although some of them recorded improvements in the final results, hardware approaches are still inefficient for aero-flow S-PIV applications, especially, when localised distortions take place. A view of the impact of local distortions on PIV measurements was investigated in ref. [24]. Local stretches and distortion gradients applied into the PIV image domain, reveal the complete degradation of the final velocity measurements, recording an error up to 100% in the velocity flow field. It is important to highlight that, even though mapping functions can mitigate partially optical distortions, in presence of cylindrical duct and high curved media, the level of error in the de-warping process is still relevant.

An example from previous study in Cranfield University [6] is reported in Figure 2.10, where significant misalignments between the left and the right camera in the de-warped target images led to high registrations errors since 3-D displacement vectors were reconstructed in different locations for both domains. It was found that, assuming a third order of polynomial for x and y and linear dependency in z-axis, the mapping functions weren’t enough to map exactly the points from the object domain to the image plane when severing optical distortions are involved.

Another example is provided in Van Doorne’s study [4]. Errors in the flow velocity profile were recorded due to miss-registration. An exhaustive study of error evaluation due to optical distortion performing calibration procedure is provided in ref [6]. The main outcome is that the calibration process struggles when optical distortion phenomena occur, increasing the error magnitude as moving closer to the boundaries of the transparent media where the velocity gradients are expected to be higher. The study was conducted by using a simple cylindrical duct and it was evident that alternative methods should be developed in order to address optical distortions on PIV techniques applied to internal aerodynamic research.

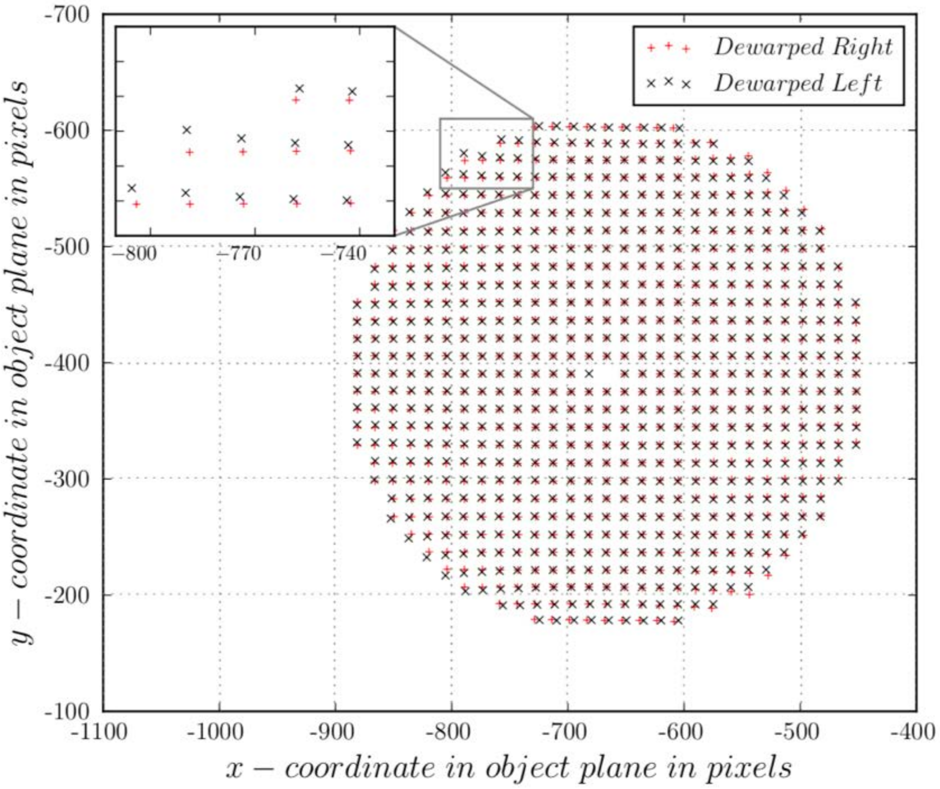

**Figure 2.10:** Effect of the optical distortion due to cylindrical working section, in the de-warped target images produced from left and right camera. Test conducted with cylindrical duct made of Perspex with 12 mm wall thickness, calibration target 5 mm and mapping function with cubic dependences in x and y and linear dependency in z [6].

## 2.4 “Gap” in the Literature Review

The theory and background on S-PIV were briefly presented in this chapter with more emphasis given to the effect of optical distortions on non-intrusive measuring techniques. In this context, several studies proposed different mitigation strategies for optical phenomena, assuming both hardware and software approaches which aimed to improve the accuracy of the measurements. Although the interest towards S-PIV technique applied for internal flow investigations and optical phenomena has increased in the last few years, limited information related to the impact of optical distortions on stereoscopic PIV measurements are available especially in the field of convoluted intakes. Moreover, a suitable optical correction method when aggressive localised optical distortions occur in calibration and seeding particle images seems to be missing.

The level of optical distortion in the current S-PIV arrangement at Cranfield University has found to be relatively high compared to equivalent studies which limit the range of the PIV applications when highly curved working sections are employed, therefore, new possible correction methods were required.

The idea to apply image processing techniques to correct optical distortions based on feature identification has revealed a completely novel approach that has never been evaluated before in the context of Particle Image Velocimetry techniques.

Some of the possible benefits that may be introduced by exploiting this method are listed below:

- Correction of the optical phenomena by performing an image pre-processing tool.
- Universal and reliable stand-alone correction toolkit for distorted images.
- High accurate S-PIV measurements of internal flows.
- Application of the PIV techniques to new research studies, such as highly convoluted intakes and ducts geometry for novel advanced propulsion systems.

# 3 Methodology

*Different methods have been applied in this work to assess the impact of local optical distortions on PIV data and fully evaluate the performance of the newly developed correction method based on feature identification. As first the synthetic approach is presented and details about the established pipeline to generate PIV images are given. Moreover, the model applied to create distorted cases will be presented, including an exhaustive description of the dataset employed. The attention will be moved then to the developed feature identification algorithm and the correction procedure. Finally, a description of the main errors considered for the assessment performance is reported.*

## 3.1 Synthetic PIV

The method used for the generation of synthetic Particle Image Velocimetry images is here presented. By synthetic PIV, it usually refers to a computational procedure that generates seeding particles images from a known displacement. Going more into details, the approach is based on different subroutines, as shown in Figure 3.1, which define the inputs required to generate PIV images. Algorithms validation and analysis of errors in the PIV measurements are widely performed by using PIV images synthetically generated which allows comparing actual results with a known true signal input. This permits to have well-proven methods free of programming errors and design parameters without undertaking experimental activities. To have a more representative data of the real flow field, highly accurate Computational Fluid Dynamics (CFD) simulations are often employed in this contest to define displacement fields from velocity profiles. Moreover, parameters of the experimental setup, such as camera angles, laser sheet thickness and geometrical configurations are needed to recreate properly the same conditions that are present in actual PIV measurements. The core of the pipeline is the PIV generator software which converts the information given by the CFD analysis and the configuration file into particles images. Further details are provided below, giving an overview of the dataset used for the correction tool validation and the assessment of the impact of local optical distortions in the PIV measurements. Few words about synthetic calibration targets will be spent in the last part of the section.

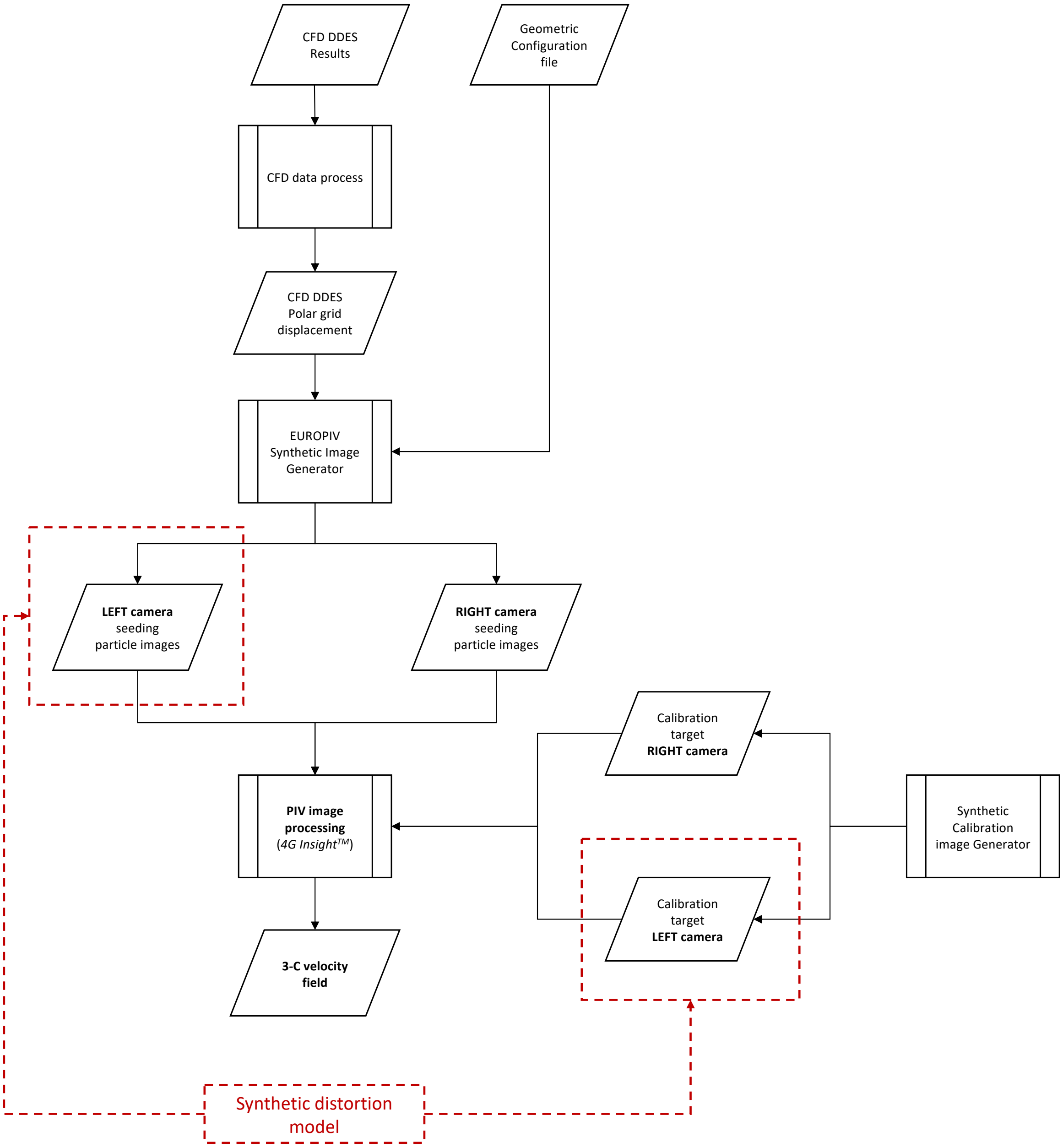

**Figure 3.1:** Synthetic PIV image generation scheme. Synthetic distortion model can be applied to seeding particle and calibration images to generate the correspondent distorted cases. In this study, the distortion was performed considering only left camera images.

### 3.1.1 S-Duct DDES CFD Simulation

As already described above, highly accurate CFD simulations are usually employed to define the displacement fields in the generation of synthetic PIV. In this section, a short description of the CFD case reported in [25] and used for the purpose of this work is here presented. The geometry investigated in the reference analysis was a diffuser convoluted S-Duct introduced firstly by Wellborn in [26] and then replicated considering the geometry dimensions reported in Table 3.1 for High Offset design.

| | $D_{in}$ | $D_{AIP}$ | $R$ | $\theta_{MAX}[°]$ | $L/D_{AIP}$ | $H_0/D_{AIP}$ | $L_{in}/D_{in}$ | $L_{out}/D_{in}$ |
|---|---|---|---|---|---|---|---|---|
| HighOffset | 121.6 | 150 | 379 | 105.1 | 4.053 | 1.978 | 2 | 3 |

**Table 3.1:** Geometry dimensions of the S-Duct expressed in [mm].

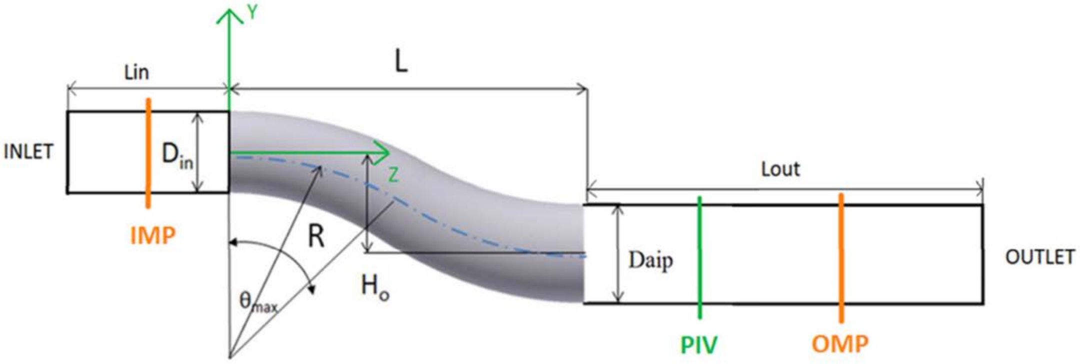

**Figure 3.2:** S-Duct geometry definition. Inlet Measurement Plane (IMP) at $s/D_{in}$ = -0.9342; PIV plane at $s/D_{in}$ = 5.526; Outlet Measurement Plane at $s/D_{in}$ = 5.73 [25].

The coordinates system is assumed as defined in Figure 3.2 where X and Y axis form the aerodynamic interface plane (AIP) characterised, respectively, by U and V velocity components while the Z-axis represents the direction of the flow according to the out of plane velocity component W. Several meshes have been generated with an in-house Python script and ICEM which were composed by a central H-grid mesh connected to an O-grid. This configuration permitted to solve correctly the boundary layer with a $y^+$ lower than 1 and to ensure an overall blocking quality above 0.86. Grid sensitivity was conducted for both RANS and DDES calculations concluding that the medium mesh of 5 million nodes gives the best compromise between computational time and quality of the results. In order to have a better representation of the flow field in the synthetic PIV images, the Delay Detached Eddy Simulation (DDES) was considered rather than the steady RANS simulation, including a compressible formulation at high Reynolds number ($10^6$). Looking at the flow properties in the study, the analysis was conducted at Mach number $M = 0.6$ and Reynolds number $Re = 1.5x10^6$ assuming a global air model based on the ideal gas formulation. Furthermore, the k-omega SST approach with pressure-based solver was chosen as a turbulent model. An important parameter for the synthetic PIV generator is the time step assumed during the simulation which is strongly related to the convective time.

The convective time is defined as the time required from a particle to pass across the entire S-Duct and its analytical expression is reported below:

$$T_c = \frac{L_{curvilinear}}{W_{in}} \tag{3.1}$$

Where $L_{curvilinear}$ and $W_{in}$ are respectively the length of the centreline of the S-Duct and the average of the out-of-plane velocity component. This gives an indication about the simulation time and permits to estimate the number of snapshots simulated. In this study 2000 snapshots have been generated for both right and left camera with a time step $\Delta t = 2.2\ \mu s$.

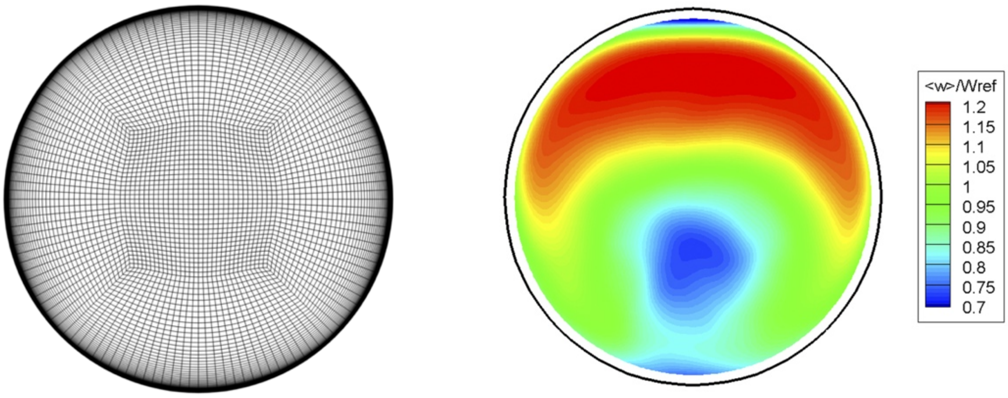

**Figure 3.3:** On the left, PIV plane 5milion nodes mesh. On the right, Synthetic PIV 3-C velocity profile.

### 3.1.2 Synthetic Image Generator SIG

Analysis of PIV errors and uncertainties are usually based on synthetic images and previous studies in Cranfield University adopted this approach to quantify the effect of optical distortions in the PIV evaluation as presented in [5] and [24]. Following the same line of thoughts, synthetic PIV images were created by using the already established pipeline based on EUROPIV Synthetic Image Generator (SIG) [27]. This is a standardised tool which is able to produce simulated PIV recordings by giving in input the coordinates of the virtual fluids domain and a configuration file with the system parameters. The software is capable to generate both 2-dimensional and 3-dimensional images, so can be used also for Stereoscopic configurations. In order to simulate PIV data, images at each time step must be created and between two consecutive frames, the particles have to move of a specific length according to the local velocity field.

To simulate the displacement field as similar to the actual one, results from Computational Fluid Dynamics (CFD) simulations available by previous works were used. In particular, Delayed Detached Eddy Simulation (DDES) results were chosen for this purpose. The software uses information of the experimental set-up specified in the configuration file and to reach a good agreement with the real case, pinhole camera equations are used to reconstruct the stereo imaging systems. A general SIG optical configuration is illustrated in Figure 3.4.

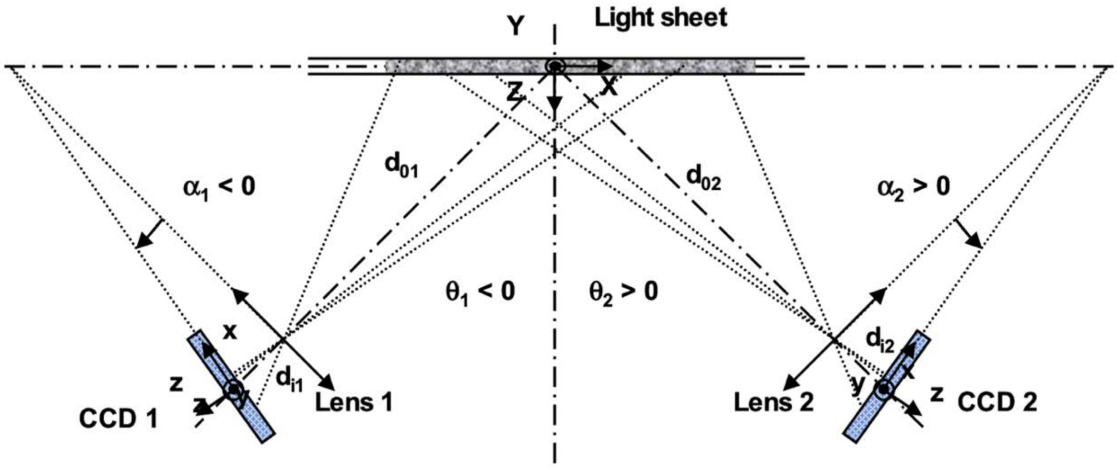

**Figure 3.4:** General SIG optical configuration [27].

The model implemented in the software is a simple angular stereoscopic vision with orthogonal projection which takes into account the effect of the Z particle motion in the in-plane measurements.

The code maps the points in the fluid domain $(x, y, z)$ to the image plane of the CCD $(X, Y)$ by solving the following equations:

$$X = \frac{p_i \cos\alpha - \mathrm{r_i} \sin\alpha - d_i \sin\alpha}{p_i \sin\alpha + r_i \cos\alpha + d_i \cos\alpha} + d_i \sin\alpha \tag{3.2}$$

$$Y = \frac{y\, d_i \cos\alpha}{p_i \sin\alpha + r_i \cos\alpha + d_i \cos\alpha} \tag{3.3}$$

Where

$$p_i = x \cos\theta - z \sin\theta \tag{3.4}$$

$$r_i = x \sin\theta + z \cos\theta - (d_0 + d_i) \tag{3.5}$$

In the equation above, the angle between the out-of-plane axis and the optical axis of the camera is denoted as $\theta$, while $\alpha$ is the Scheimpflüg angle.

The geometric parameters are extremely important since the magnification effects depend on them. In this case, approximate values have been chosen based on the knowledge of the test rig configuration. A summary of the main parameters used in the SIG software is reported in Table 3.2.

As already mentioned above, the image generator requires the position of the particle in the object plane as an input. This information comes from the results of the CFD simulation. Firstly, a uniform three-dimensional mesh points are generated over a predefined volume. Then a random number generator creates particles displacement in the coordinates of the mesh nodes. Since the CFD data are expressed in polar coordinates, an interpolation process on a rectangular grid is firstly performed. Once the velocity vectors are consistent with the particle displacement, a bilinear interpolation is computed in order to associate velocity vectors to each particle position and a filter is applied to eliminate particles that are not contained in the actual cylindrical domain of the experiment. The benefit to using CFD data is related to the higher spatial resolution of those compared with experimental results which lead to a more accurate interpolation. The relative displacement is derived from the velocity by multiplying it for the time distance $\Delta t$ between two consecutive recordings. Once the displacement is known, the particles images at initial time $t_0$ and $t_f = t_0 + \Delta t$ are generated. The final outcomes are 8-bits seeding particles images with a density of 30 $particles/mm^3$. This procedure is performed for both left and right cameras and for the scope of this work, 2000 snapshots were generated with a time step of $\Delta t = 2.2\ \mu s$.

| Parameters | Left Camera | Right Camera |
|---|---|---|
| $\theta$ [°] | -45 | 45 |
| $\alpha$ [°] | -5.75 | 5.75 |
| $d_i\ [mm]$ | 63.7 | 63.7 |
| $d_0\ [mm]$ | 632.5 | 632.5 |
| $Image\ height\ [pixel]$ | 2048 | 2048 |
| $Image\ width\ [pixel]$ | 2048 | 2048 |
| $Fluid\ domain\ dimensions\ [mm]$ | 150x150x10 | 150x150x10 |
| $Laser\ sheet\ thickness\ [mm]$ | 1.5 | 1.5 |
| Laser sheet z position [mm] | 0 | 0 |

**Table 3.2:** Parameters used in the Synthetic Image Generator (SIG).

### 3.1.3 PIV Processing

Synthetic PIV images can be treated as the equivalent experimental images in terms of PIV evaluation and post-processing, therefore, the commercial software *4G Insight$^{TM}$* was used to compute the three-component velocity field. As already described in the previous chapter, the first step in the digital PIV evaluation is the definition of the size and the number of the interrogation windows or *spots*. In this case, a recursive Nyquist grid was employed with 64x64 pixels and 32x32 pixels spots size, respectively for the first pass and second pass. Before performing the cross-correlation analysis, a preconditioning procedure based on a zeroPad mask is applied to the spots. This practice subtracts the average pixel intensity of each spot from each pixel in the window region in order to improve the signal-to-noise ratio. The cross-correlation process is performed by assuming the Fast-Fourier-Transform (FFT) correlator and a three points Gaussian sub-pixel peak estimator is then used to locate the correlation peak [8].

Once the displacement vectors are computed, a local validation procedure is performed in order to take into account only consistent vectors in the second pass with smaller spots. The validation process consists of generating a reference vector for each computed vector using the other displacements in a neighbourhood of 5x5 pixels. If the calculated vector is different by more than 2 pixels from the reference value, the former is rejected and substituted with the local median vector.

As a final step, a vector smoothing is applied, replacing each vector by the Gaussian-weighted mean of the neighbourhood vectors. The procedure is repeated for the smaller 32x32 pixels grid and the smoothed vector field expressed in pixels is stored. In a summary of the settings used in this work is presented.

| | SETTINGS |
|---|---|
| Grid Engine | Recursive Nyquist Grid → 64x64 pixels and 32x32 pixels |
| Spot Mask Engine | ZeroPad Mask, Minimum Average Intensity > 1 |
| Correlation Engine | Fast Fourier Transform (FFT) |
| Peak Engine | 3-points Gaussian sub-pixel peak → Threshold > 2.0 |
| Local validation: | Universal Median Test |
| - Size | 5x5 |
| - Tolerance | 3 |
| - Replacement | Local median vector |

**Table 3.3:** Configuration settings used in the PIV processing engine

The analysis of this study aims to quantify the impact of local distortions on S-PIV images, therefore, a calibration procedure based on synthetic targets was necessary for addition to the two-components analysis. The two-dimensional synthetic PIV is surely simpler than the three-components one and only the parameter relatives to the magnification of the images is needed while three-dimensional velocity field reconstructed by including the de-warping process based on calibration determines a more representative behaviour of the flow field. For the purpose of this work, the three-dimensional PIV procedure is the one considered assuming the stereo camera configuration already described previously.

There are two different approaches to derive the third component of the velocity field. One is to back-project PIV images before computing the velocity vectors, while the second approach which is implemented in *TSI Insight*$^{TM}$, is to calculate the 2-D displacements in the image domain and then project these to the object domain and process the out-of-plane component. Once the in-plane velocity field is computed separately for each camera, the de-warping process is based on the non-linear transformation described in §2.2.1.

**Synthetic Stereoscopic Calibration.** The mapping functions are constructed starting from the identification of the markers in the two calibration target images, one for each camera. In this case, synthetic images of the calibration plates previously created in Caruso's work [5] were used to perform the calibration process. An example is reported in Figure 3.5 for the left camera. It is worth to say that more than one calibration image is required to reconstruct properly the third component of the velocity.

In particular, five images of the target translated along the out of plane direction were created. The consistency of the calibration images with the real target has been widely tested by comparing the magnification of the real recordings and the synthetic one, as presented in [5], therefore, high fidelity synthetic S-PIV images can be simulated which permits to validate accurately the new method developed in this study. According to Soloff [3], the two main parameters are essential to define a calibration target: number of the dots and spacing between each marker.

As it will be demonstrated in the results section, these two are key factors for the newly developed method performance which employed the synthetic calibration targets as the one illustrated above to extract information about optical distortions distribution. In particular, the distance between the dots expressed in pixels is assumed as reference value for the analysis of the method effectiveness. The value was estimated considering an average of the marker positions. The properties of the synthetic target employed are reported in Table 3.4.

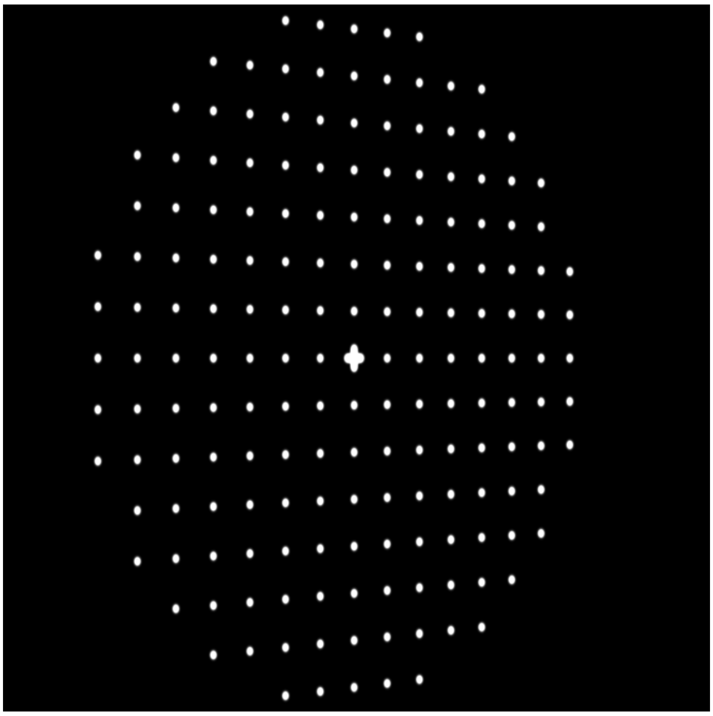

**Figure 3.5:** Synthetic Calibration Target (Left camera).

| Parameters | Value |
|---|---|
| $Number\ of\ points$ | 176+1 (fiducial mark) |
| $Calibration\ points\ diameter\ [mm]$ | 2 |
| $Spacing\ between\ points[mm]$ | 10 |
| $dots\ resolution\ (ddots)\ [px]$ | 96 |
| $Out\ of\ plane\ translation\ [mm]$ | 0.375 |
| $Calibration\ function$ | Polynomial |
| $X\ and\ Y\ Polynomial\ order$ | 3rd order |
| $Z\ polynomial\ order$ | 2nd order |

**Table 3.4:** Synthetic calibration parameters.

## 3.2 Synthetic optical distortion model

Optical phenomena on Particle Image Velocimetry measurements have been widely recognised as one of the major sources of errors in the PIV velocity when the flow field is recorded imaging through a transparent medium. By definition, optical distortions are essentially a geometric deformation of the images. Different types of distortions can occur in a PIV setup and in case of stereoscopic vision, the perspective distortion is inherently present due to imaging in an oblique angle. As a result, a non-uniform magnification is experienced in this configuration, which necessitates a camera calibration in order to be corrected.

Another type of distortion is the one related to the lens curvature, which can be classified depending on the lens sign. An example of perspective and Barrell distortion, respectively, are illustrated in Figure 3.6.

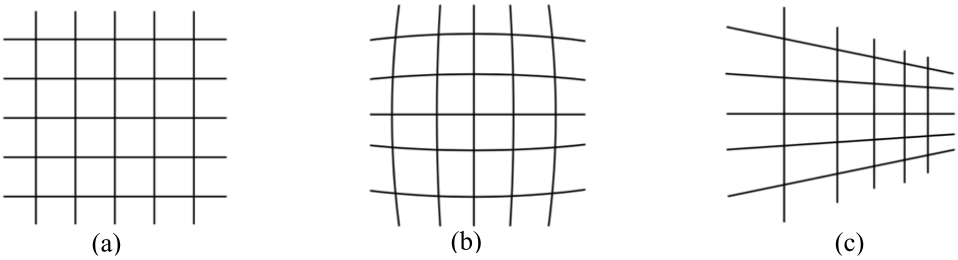
(a) (b) (c)

**Figure 3.6:** Types of optical distortion, (a) Undistorted, (b) Barrel, (c) Prospective.

Correction strategies presented in the literature usually implements affine transformations in order to project the distorted points into undistorted ones, however, this does not represent a suitable generalised solution. In the contest of optical non-intrusive measurements techniques applied to internal aerodynamic flow, low-quality transparent windows can produce aggressive non-linearities in the recorded images which leads to classifying these approaches as non-applicable. The aforementioned example, demonstrates clearly the importance of the working section design and its relative manufacturing quality, especially when convoluted ducts are involved in the experimental activities. To meet the demand of having suitable tools that correct optical distortions from PIV images, mathematical models of common optical deformations have been developed in Cranfield University based on experimental observations of the phenomena.

For the scope of this work, the local optical distortion model was applied to the clean synthetic calibration target introduced above in order to generate a dataset of distorted calibration images. The pipeline established for the synthetic local distortions is here presented.

### 3.2.1 Local optical distortions

Local optical distortion can be defined as an aberration of the seeding particles restricted in a specific region of the image due to imperfections in the duct surfaces. This phenomenon appears as a localised stretching in a specific direction of the features in the image which can be modelled as a Gaussian function expressed as:

$$f(x,y) = a\, e^{-\left(\frac{(x-b_x)^2}{2\, c_x^2}+\frac{\left(y-b_y\right)^2}{2\, c_y^2}\right)} \tag{3.6}$$

Where $a$ indicates the peak displacement, $b_x, b_y$ are the peak location along the coordinate X-axis and Y-axis while $c_x, c_y$ represent the standard deviation of the Gaussian curve respectively in X and Y direction which defines the width of the distortion. More specifically, the Full Width at Half-Maximum (FWHM) is equal to 2.355 times $c$ parameter. In the contest of optical distortion occurring on images, the two-dimensional expression and specific directions of how the distortion is applied are required. The illustration of the distortion function is represented in Figure 3.7. Different distortions can be created by changing the parameters of the model and apply for a generic image as input, i.e. calibrations targets or seeding particles images. The script of the 2D gaussian distortion requires as input an image and it gives back the equivalent input distorted and the applied synthetic distortion map.

The current tool was employed to generate the dataset of distorted calibration images used to assess the developed correction method. Moreover, starting from a clean seeding particle case, correspondent distorted images were generated to quantify the impact of local optical distortions on PIV data as well as to prove the effectiveness of the new method.

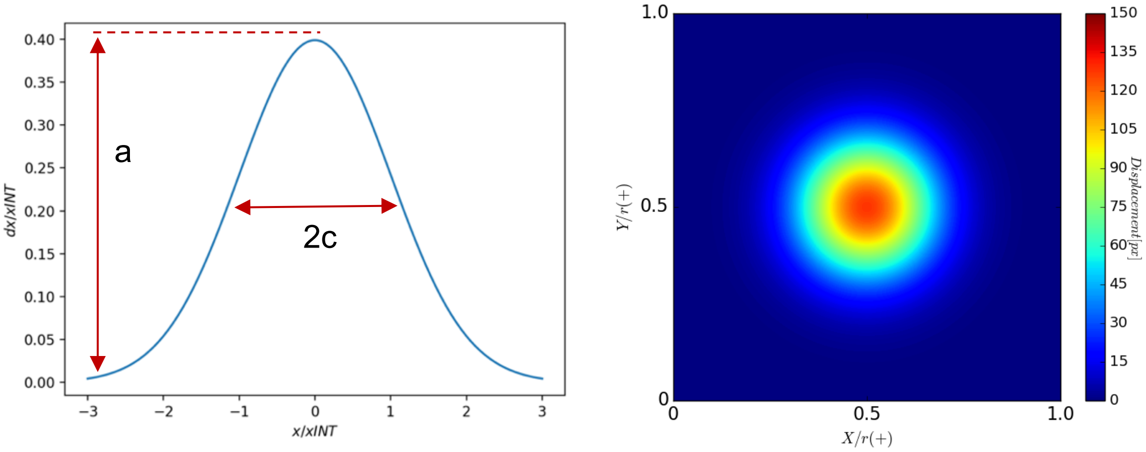

**Figure 3.7:** General example of the 2-D Gaussian Distortion function (a = 128px, c = 256px). Parameter a and c are respectively the distortion magnitude and the standard deviation.

## 3.2.2 Validation Test Matrix

The developed correction method based on feature identification uses two images of the calibration targets, one clean and the correspondent distorted image, to extract the distortion map necessary for the correction. In order to demonstrate the overall idea and prove the effectiveness of the method, a complete bench test was created using the synthetic distortion model proposed above. As already seen, different types of distortions can be evaluated by changing the parameters of the 2-D Gaussian function which can be applied either for calibration plate images or seeding particles images. This permit to fully assess the effect of optical distortions on the PIV velocity synthetically showing the benefits to introduce correction methods in the PIV evaluation procedure.

As first, the set of calibration distorted images was created. The model parameters were considered to represent a varied range of cases, from weak distortions represented by few pixels displacement to very aggressive deformations which are rarely found in experimental setups. The final outcome was the Test Matrix reported in Figure 3.8:

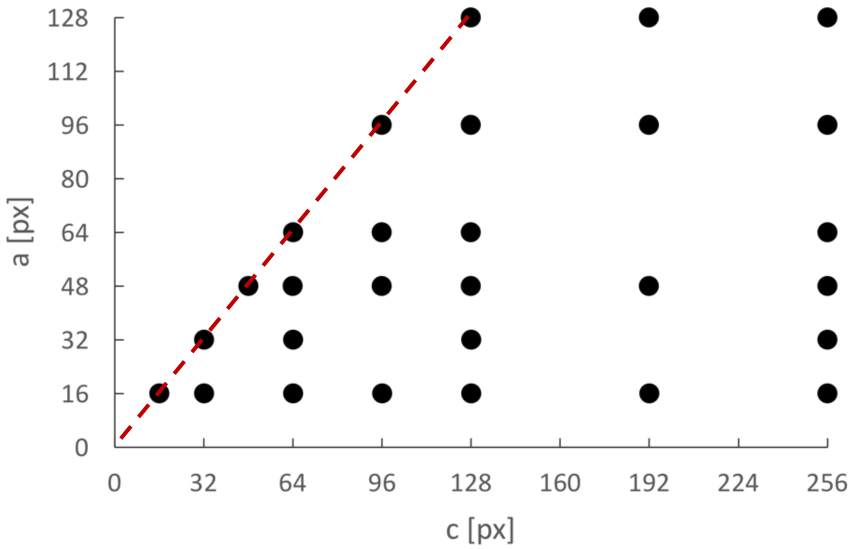

**Figure 3.8:** Test Matrix generated for the validation process. Each dot identifies one type of distortion given by different combination of amplitude a and extension c. dashed red line indicates the limit beyond which the distortion causes overlapping.

Each point of the matrix represents one type of distortion. Moderate distortions are identified by low value of amplitude $a$, while high distorted cases are confined in the upper side of the validation test matrix. Moreover, elements with same value of $a$ and $c$ represent high gradient distortions cases which define a strong limit in the choice of the parameters. For combination of $a$ and $c$ over the limit denoted by the red dash line, the distortion introduces markers overlapping between columns and rows which does not have any physical meaning. Moving for higher value of $c$ the distortions result smoother and they extent over a larger area of the image. It is worth to say that in the current study symmetric distortions are considered which means that the parameters are applied in both X and Y axis, therefore, $c_x = c_y$. In addition to that, an arbitrary position of the peak location was chosen assuming a relative location from the image centre equal to $b_x = b_y = 256px$ and directions at 45°.

In this condition, the maximum peak displacement is given by the following expression:

$$a_{max} = \sqrt{2\,a^2} \tag{3.7}$$

Finally, synthetic PIV images generated by performing the pipeline described in §3.1 were distorted assuming the same type of synthetic deformations presented in the test matrix. All the distortion cases were created considering the left camera, while the right one was preserved without any alterations.

An example of the distorted outcome for both calibration and seeding particle images is provided in Figure 3.9.

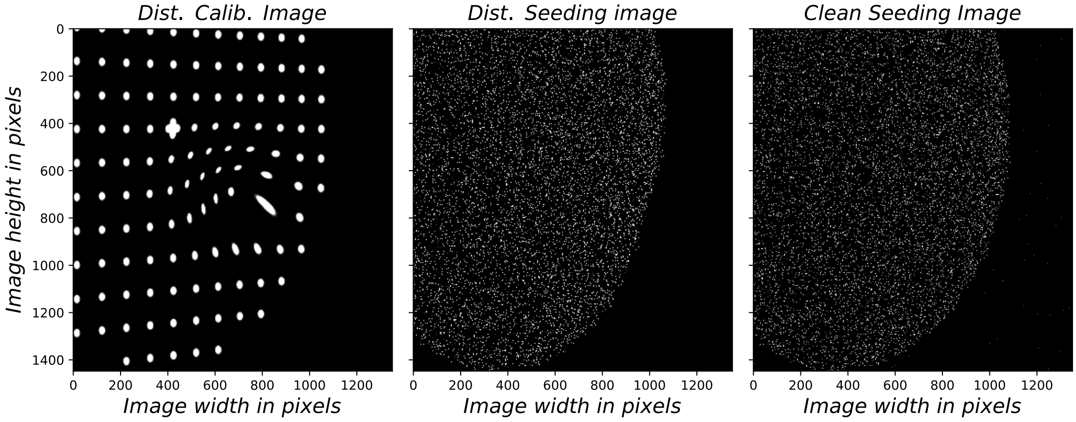

**Figure 3.9:** Effect of 128x128px 2-D Gaussian distortion on calibration target (Left) and seeding particle (Right) images.

# 3.3 S-dust Experimental Setup

The test facility developed at Cranfield University permits to investigate complex flow phenomena through convoluted intakes. Different types of measurements techniques can be employed in the experimental set-up such as hot-wire anemometry, pressure rakes and non-intrusive optical measurements, i.e. S-PIV. The rig is highly modular with the capability to accommodate several components and duct geometries depending on the researcher’s needs. The general S-Duct configuration of the experimental setup is proposed in Figure 3.10.

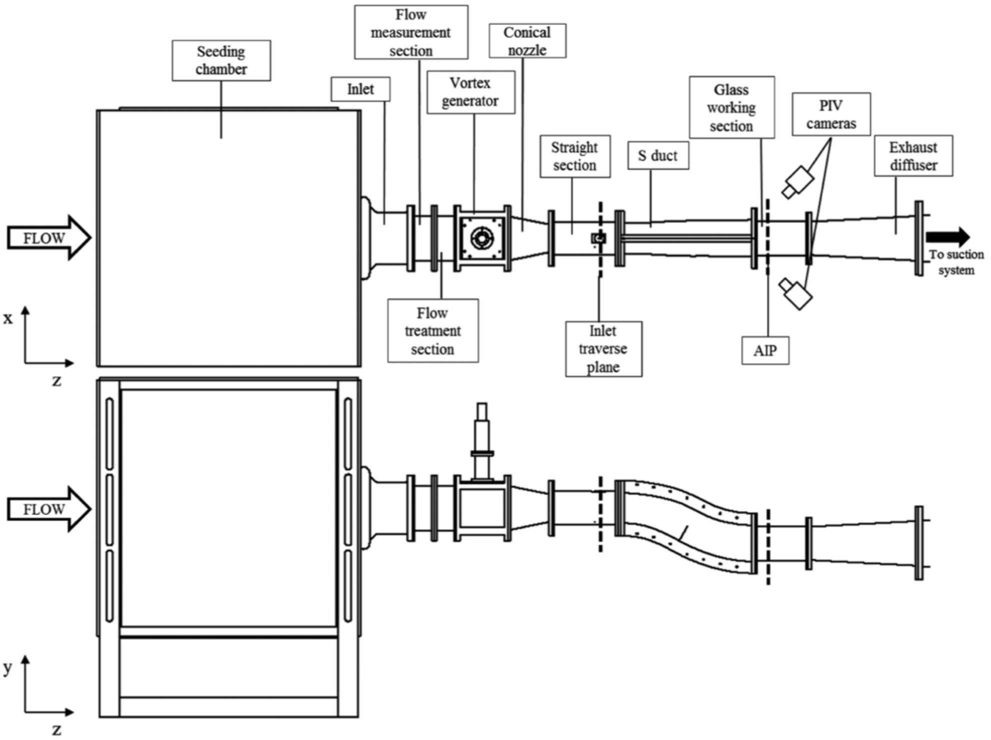

**Figure 3.10:** General arrangement of the test rig at Cranfield University [2].

As already mentioned in §2.1, it is part of the Particle Image Velocimetry technique to mix the flow with seeding particles before undertaking any measurements. This is the first step in the test rig, where a seeding chamber is accurately designed to generate a uniform trackers distribution in the interest flow at the rig inlet. A Bell-mouth intake delivers the flow into a 200 mm conditioning section which includes honeycomb flow straighteners. Static pressure measurements are taken by pressure tappings installed before the honeycomb mesh. The conditioned flow passes through a section where vortex generators can be installed if needed and then is diffused by a conical diffuser in order to reduce the diameter to 120 mm ($D_{S-Duct,in}$) which allows to accommodate the S-Duct inlet. Usually short straight tubular sections are located just before and after the S-Duct to allow PIV flow measurements.

In the current study the S-PIV set-up was positioned downstream of the duct, defining the object plane of the experiment as depicted with the dash line in Figure 3.10. Further information about the measurements plane will be given in the §3.3.2, since calibration images are taken in this region. The laser sheet is located downstream of the S-Duct exit in particular at $0.25\ D_{S-Duct,out}$ where in this case the outlet diameter of the S-Duct was

150mm. In order to avoid stresses, loads and facilitate the access where the measurements take place, a flexible duct is installed next to the transparent working section. The flow is guided finally to a single stage centrifugal fan which exhausts the flow in the main stream. The test rig operations are completed automated and the inlet Mach number is regulated based on the pressure measurements along the rig.

### 3.3.1 Stereoscopic PIV Equipment

The stereoscopic PIV instrumentation and the geometrical configuration adopted in the current work are here presented. As already widely described in the previous sections, stereo PIV employs two cameras positioned in a specific optical arrangement. The S-Duct facility in Cranfield University used two TSI PowerView 630092 high-speed cameras equipped with Complementary Metal-Oxide Semiconductor (CMOS) sensors. The cameras were positioned at an angle of 45° relative to the normal axis of the measurement plane in the direction of the flow and the CMOS sensors produced images at 16 bits of depth with 2048x2048 pixels resolution. In order to achieve the best focus, the lenses were tilted with a Scheimpflüg angle of approximately 6 degrees for both cameras, assuming an aperture of $f^{\#} = 4$ and a distance from the measurements plane of 350mm. A pair of *Nikon* AF 1.8/D *Nikkor* lenses were used with 50 mm of focal length and aperture $f^{\#}$ from 1.8 to 22.

### 3.3.2 Tubular Working Section & Calibration Target

As already mentioned earlier, non-intrusive optical measurement techniques require transparent windows. In this case a transparent cylindrical duct was installed in order to perform the measurements. It is worth to highlight that only calibration images were taken for this analysis which aims to test the optical correction method based on feature identification applied to real images.

As discussed so far, optical distortions are introduced into seeding particles and calibration target images when recording through a transparent curve section. Moreover, the manufacturing procedure and materials properties influence significantly the quality of the images which can experience different levels of deformation. In Cranfield university several tubular working sections have been used through the numerous conducted experimental campaigns. The Table 3.5 summarises the properties of the three cylindrical ducts employed in this study.

| Section | Material | Index n[1] | Transmittance[1] | OD | Thickness |
|---|---|---|---|---|---|
| | | (-) | (%) | (mm) | (mm) |
| Glass5 | Borosilicate glass | 1.473 | 92 | 160±2.0 | 5.0±0.7 |
| Perspex5 | PMMA[2] | 1.490 | 92 | 160±0.8 | 5.0±0.5 |
| Perspex12 | PMMA[2] | 1.490 | 92 | 174±0.9 | 12±1.2 |

**Table 3.5:** Tubular working sections assumed in this study. [1]Referred to $\lambda = 380 - 790nm$, [2] cast acrylic [6]

These working sections add different optical non-linearities depend principally on the manufactured materials and the thickness of the wall as presented in [6]. For the purpose of this work, clean and distorted calibration target images were taken to prove the effectiveness of the correction method. Many targets can be employed in the three-dimensional spatial calibration and different patterns are able to capture optical distortion effects as demonstrated in previous works. According to [3], two are the main parameters in the design of the calibration target, namely the spacing between the markers and their amount in the image plate. In experimental activities, target plates with high marker density are used in order to increase the accuracy of the de-warping map and mitigate better optical phenomena. The Target x5y5 is usually employed in high accuracy measurements, therefore it was chosen instead of the Target x10y10 used in the previous analysis in its synthetic version in order to recreate the same conditions of an actual experimental campaign and to test the robustness of the feature identification algorithm when applied to a finer calibration plate.

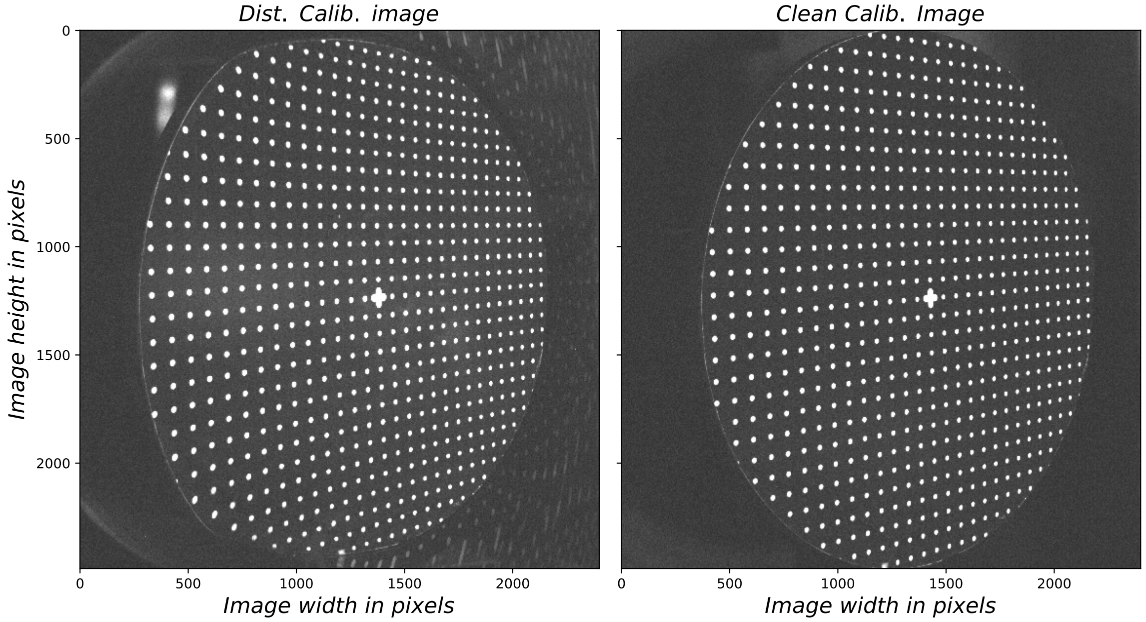

**Figure 3.11:** On the left, distorted Target x5y5 image due to Perspex12. On the right, correspondent clean Target x5y5 image taken by removing the transparent duct.

## 3.4 Feature identification algorithm

One of the main objectives of this study is to code an optical distortion correction method based on feature identification and demonstrate the effectiveness of the idea for a bunch of synthetic and experimental cases. In this section, an exhaustive description of the developed feature identification algorithm is presented, providing the basic principle, limitations and possible improvements.

### 3.4.1 Feature detector

The idea behind this study is to extrapolate information of the distortion occurring in the PIV data based on the marker displacement of the calibration images. Features in the calibration targets may change position when recorded through a transparent medium by PIV cameras therefore if compere with a clean image for example taken without windows, it is possible to reconstruct the optical phenomenon by computing differences between the dots' position of the clean and distorted case. In order to achieve this, an algorithm that extracts properly the coordinates of the centroid of each marker in both images must be developed. In the last decades, feature detectors have received considerable attention in computer vision community and they have been applied widely in many different applications. Object recognition and matching [28], 3D scene reconstruction [29] and motion tracking [30] are just a few examples where feature detection is successfully performed. Moreover, camera calibration procedures require robust detector algorithms that are able to identify accurately calibration target dots or markers and deal with brightness and image distortions, such as optical warping, noise and blurriness.

Common PIV software typically identifies square or circular patterns during the calibration process by performing marker detection functions. Another example is given in ref. [6], where contour detection algorithm in *OpenCV (Open source compute vision)* python library [31] was performed to detect calibration markers in order to quantify registration error due to optical distortion. Furthermore, the accuracy of the detection markers was investigated, revealing contour detection algorithm robust enough within a range of degraded images.

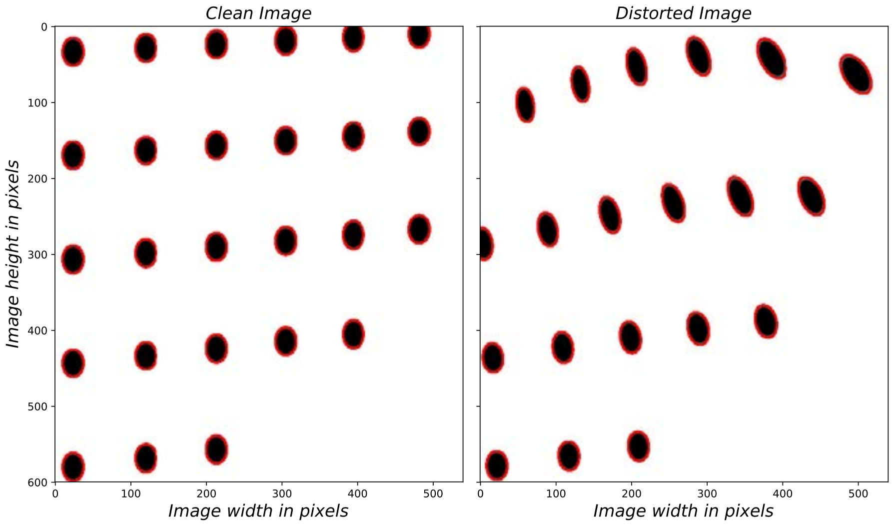

**Figure 3.12:** Output of *FindContours* function applied to clean and distorted images. (Colours inverted for clarification)

Although, the contours shape detected change as decreasing the image quality, no trend in the associated error was found. For the purpose of this work, traditional feature identification algorithms widely employed in computer vision and image processing, such as SIFT and Harris detectors [32], were revealed not suitable to detect properly repetitive patterns in calibration targets due to lack of distinctive key points in the images.

Moreover, in order to compare correctly the distorted markers in their correspondent clean dots in the no distorted image, the algorithm must find the features in a systematic way for all the images. The found solution was to build a new searching algorithm based on the feature detector functions already included in the Python libraries.

*OpenCV* library provides several functions to compute centroids of features in an image, such as *SimpleBlobDetector*, FindCircleGrid and *FindContours*. The first two are based on blob detection methods which consider features as regions of the image with constant or similar properties while the last one employs border following techniques to extract the contours of image features by using suzuky85 algorithm [33]. Some tests have been conducted using different approaches and *FindContours* function was revealed easier to implement and robust enough for this scope since it has been already applied and widely tested on calibration images [6].

### 3.4.2 Systematic searching algorithm

As already mentioned above, in order to extract optical distortions using feature detectors discrepancies between the centroids of clean and distorted markers have to be computed consistently, which means that one-to-one correspondences must be created for each dot of the distorted image and their equivalent clean. One of the critical aspects of the algorithm development was to create those marker associations. Features detectors scan the image by increasing in Y-axis and identifies as first the contour of the marker with high value of Y-coordinate. The problem arises when optical distortions alter feature positions in the image. In this condition, how the coordinates of the centroids are sorted is not consistent with the clean case, making difficult to derive the right correspondences.

A straight forward solution could not be found based on sorting algorithms therefore an ad-hoc systematic searching procedure was required. The flowchart of the feature detection algorithm is illustrated in Figure 3.13 and will be here explained.

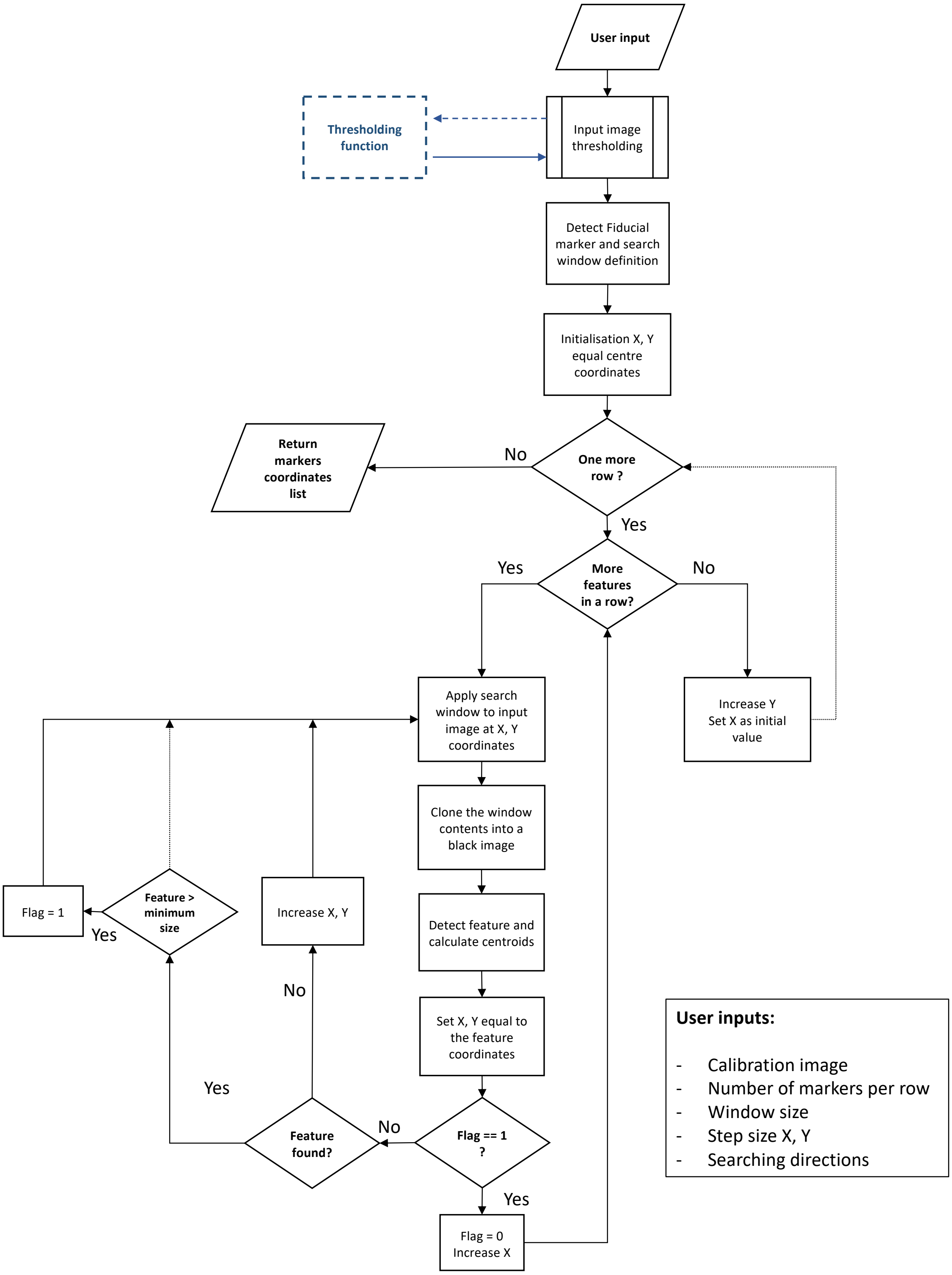

**Figure 3.13:** Flowchart of the systematic searching algorithm developed for feature identification.

Before going into more details about the feature searching strategy, a small bracket about how *Python* manipulates images is provided. Basically, images are sources of data which are treated as numerical arrays where each element represent a pixel information of the image. Dimensions of the arrays and the values if each pixel depends on the bit depth and the format of the image itself. Typical formats commonly used are RGB and Grayscale. In colour images each pixel is coded by a sequence of 24bit, 8bit per channel, red, green, and blue while in the Grayscale formats each pixel is attributed a luminance value between 0 and 1. Image processing operations, like feature detectors or thresholding functions, require usually grayscale images, therefore, this format will be considered as reference.

Moving forward with the method description, the user inputs are firstly defined which includes the image of the calibration target, number of the markers in each row, step size in X and Y axis and directions. Feature detectors do not distinguish bright spots in the image from calibration markers, which can be the cause of errors during the searching process, thus undesirable noise in the image is removed by employing a thresholding function. Since synthetic images are generated artificially source of noise are not present in this case, however, for experimental data, image post-processing must be performed. Further information about the developed image post-processing toolkit is discussed in *Chapter* 6 when experimental data are involved.

The next step is to identify the centre of the calibration plate, setting it as a starting point of the searching loop. Different strategies can be used for this purpose, for examples identify initial value by clicking on the image or computationally from image size. In this case the more logical choice was to start from the centroid of the fiducial mark previously detected with *FindContours* function.

The overall idea of the algorithm is to define a searching window which scans a quarter of the calibration image according to the directions imposed in the user inputs as shown in Figure 3.14.

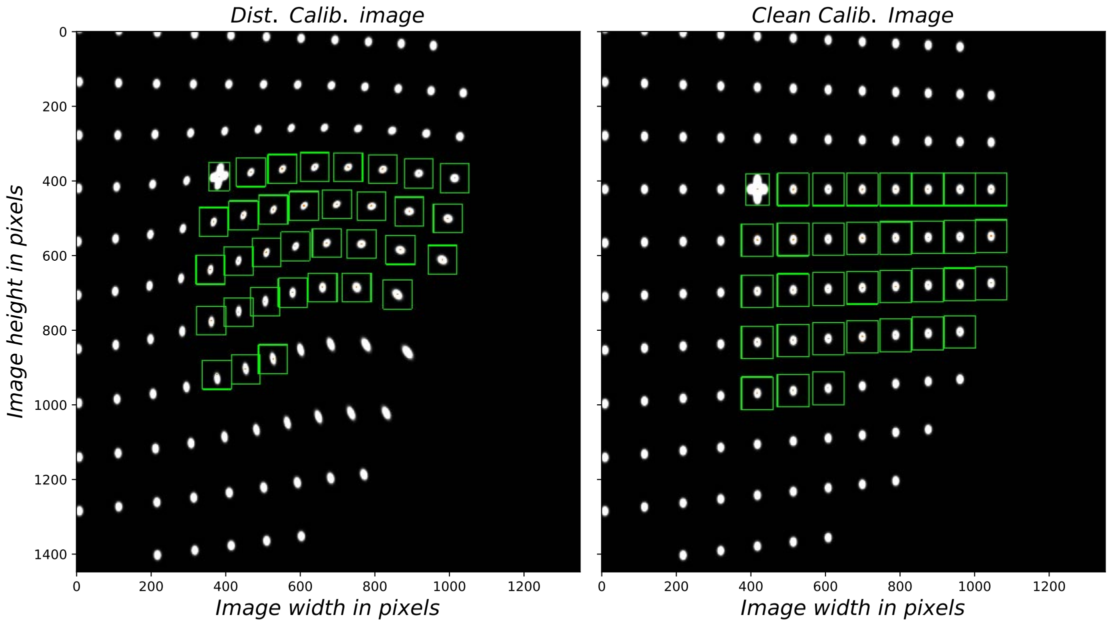

**Figure 3.14:** Outcome of the Systematic Searching Algorithm developed to identify features in the calibration images. The algorithm scans a quarter of image and identifies the coordinates of each feature centroid.

Window size is a critical parameter to successfully detect the dots which must be the right dimension according to the marker size and the distance between the dots. Too large window may include partially or completely neighbouring features that can be captured and provoke errors in the code, by contrast, adopting small windows reduces the probability to include the markers in the region of interest. Another factor that influences the final outcome is the increment in X and Y axis at each iteration. Typical values used to configure the feature identification algorithm for synthetic and experimental cases are reported in Table 3.6.

| Distortion | Width | Height | Step X | Step Y | Min size | Threshold |
|---|---|---|---|---|---|---|
| 96x96 | 67 | 98 | 85 | 110 | 170 | 60 |
| 128x128 | 76 | 70 | 94 | 110 | 190 | 60 |
| X5y5Perspex12 | 45 | 68 | 62 | 90 | 190 | 75 |

**Table 3.6:** Typical settings of the feature identification algorithm for synthetic and experimental images. The parameters are expressed in pixels.

Once a marker is detected inside the defined region centred in $(X_i, Y_j)$, the searching window is moved forward in X direction at point $(X_{i+1}, Y_j)$ computed adding a constant increment, $X_{i+1} = X_i + c_x$, while $Y_j$ is kept constant, $Y_{j+1}\mathrm{z} = Y_j$. Following the same line of thought for the vertical movement, when all the dots in a row are detected, the Y coordinate is increased, $Y_{j+1} = Y_j + c_y$ and $X_i$ is initialised at the value of the X coordinate of the first marker detected. It is important to notice that $c_x$ and $c_y$ are constant, which means that if the distance between the dots is not uniform in both X and Y directions, the code struggles to find a marker as well as to converge on a right solution. In order to mitigate partially this issue, a second control loop has been included which keeps moving the searching window a little further until it finds a contour.

Finally, when the loop is completed the algorithm returns back two arrays with the feature coordinates sorted as imposed by the directions. As already mentioned the function has been designed for one quadrant of the calibration plate which means that the number of dots per row should be provided considering a quarter of image, as illustrated in Figure 3.14. Since the calibration target is symmetric, to obtain the coordinates of the entire plate a script has been developed to extract all the features in the images for both distorted and clean cases.

### 3.4.3 Image Pre-processing

When experimental images are used in the correction method some precautions need to be taken in order to ensure an accurate and efficient analysis. In this section, the tools developed to process the experimental images are here presented.

Experimental calibration images are usually affected by noise and imperfections such as white and grey areas which could compromise the accuracy of the detection process. As already pointed out in §3.4.1, the marker detector is sensitive to changes in pixels luminance values. This could be an issue when part of the background and residual figures, such as partial features, boarders of the plate or simply reflections of the working section are present in the image. In this situation, a pre-process strategy must be considered in order to detect correctly the features. The flowchart illustrated in Figure 3.15 summarises the procedure implemented in this study.

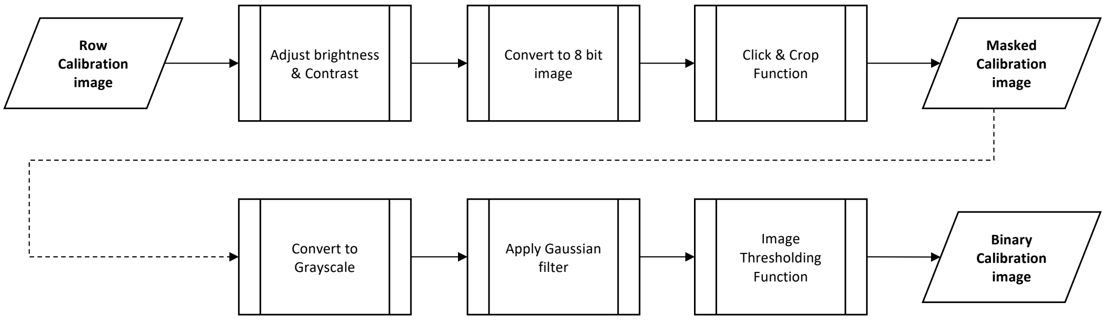

**Figure 3.15:** Pre-processing work-flow used to precondition the experimental calibration images before undertaking feature identification algorithm.

The processing starts by adjusting the brightness and contrast of the row calibration image. As discussed in the previous section, the cameras employed in the experimental setup record images with 16 bit of depth which is not compatible with the usual image processing functions available in the OpenCV library, therefore, are converted into 8bit images. Next, to remove the background and residuals noise in the image, a crop function is performed.

The *Click&Crop* function permits to define a polygonal mask based on interactive clicks and isolate a specific region of the image i.e. the calibration target, setting null values outside of the defined boundary. This allows isolating the calibration target excluding the rest from the image. Although this process removes mostly the noise and undesirable bright areas, some unwanted details may be still present in the region of the markers which can be caused by errors in the detection procedure. To achieve a perfect clean markers region, an ad-hoc thresholding function has been developed based on the structural analysis function namely *connectedComponentsWithStats()* already present in the image processing library.

This script permits to binarize a greyscale image by imposing as a threshold the minimum size of the markers. The features that are smaller than the condition imposed are removed from the image while the markers of the calibration plate are kept unaltered. To improve even better the final results the 2-D isotropic Gaussian filter is applied to the image. An example of pre-conditioning of the experimental calibration image is reported in Figure 3.16.

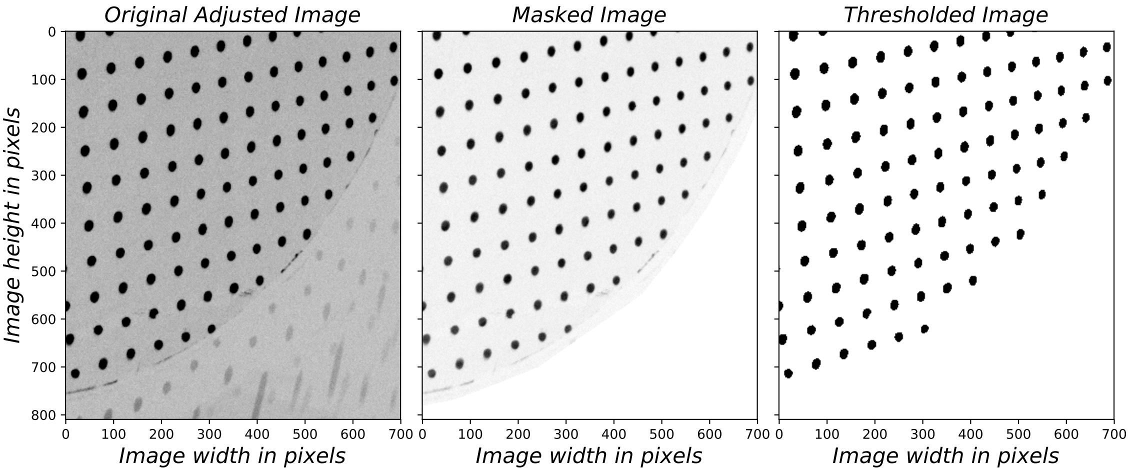

**Figure 3.16:** Example of image pre-processing applied to the distorted experimental Target x5y5 with working section Perspex12.

# 3.5 Optical Distortion Correction Method

Once the position of the features in each calibration image is successfully detected by performing the feature identification algorithm, the distortion map can be reconstructed. An overview of the developed optical distortion correction method is presented in Figure 3.17 and here described in details. As already seen in the previous sections, optical distortion induces changes in the marker displacements of the calibration target (see Figure 3.9) and consequentially variations in their coordinates in the imaging system of reference. In simple terms, the extraction procedure derives the distortion function based on the discrepancy information between the clean and distorted images.

Since the extraction procedure is one of the main operations in the correction process, further details are provided in a separate section. The last step in the correction pipeline is to apply the inverse of the distortion map to the distorted image in order to generate the corrected calibration target.

It is worth to say that all the operations computed on the calibration images are implemented using the OpenCV library, which includes suitable tools for image transformations given a generic function as input.

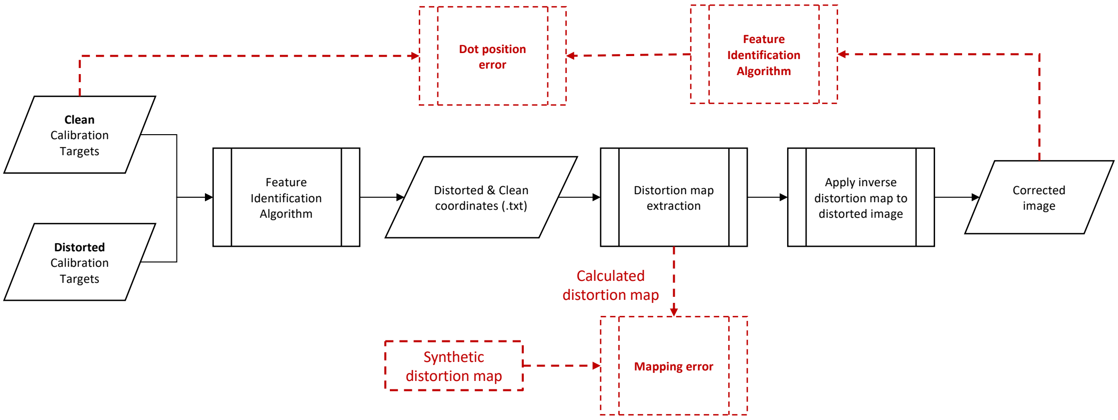

**Figure 3.17:** Overview of the established optical distortion correction method based on feature identification.

It is part of the method ensure that the distortion map extracted is consistent with the synthetic distortion model applied previously to generate the distorted calibration target for that reason, a dedicate script has been developed to compute the error between the distorted and calculated maps. Moreover, a quantitative index of the method performance has been defined by comparing the clean image with the corrected outcome and calculating the relative error called Dot Position Error (DPE).

### 3.5.1 Distortion Map Extraction

As introduced above, knowing the coordinates of the distorted and clean markers allow to calculate the distortion map necessary for the correction of the dot displacements in the original image. In this section, the extraction map procedure is described, commenting on all the operations required in order to get the final outcome.

The outputs of the feature identification algorithm are two text files which contain respectively the dots coordinates of the clean and distorted targets. As first the dots files are imported as numerical arrays of integers and the differences is computed for both X and Y axis.

$$dx = x_{clean} - x_{distorted} \tag{3.8}$$

$$dy = y_{clean} - y_{distorted} \tag{3.9}$$

In order to extract a 2-D distortion function, structured data must be considered which means that a sequence of interpolation processes are required. In particular, the desired grid is computed by interpolating the vector of the clean dot coordinates into a regular predefined grid having the same size of the calibration and a specific grid resolution. It is important to highlight that, the grid spacing influences the interpolation process and a similar or higher resolution of the dot position should be preferred in order not to compromise the quality of the calculated map. Nevertheless, the grid spacing parameter is strongly related to the computational time spent to compute the interpolation.

In this study, a grid spacing of 32 pixels was assumed which represent the best compromise between time and goodness of the map. Once the rectangular grid is generated, a Delaunay triangulation is performed for the set of clean points before undertaking the interpolation. A Delaunay triangulation is a 2-D triangulation of points that follow the empty circumcircle criterion which ensures that the circumcircle associated with each triangle does not contain any other point in its interior [36].

The interpolator requires a triangulated set of points represented by the coordinate of the clean dots and a vector of values given by $dx$ or $dy$, performing on each triangle a linear barycentric interpolation with the regular grid previously defined [34]. This procedure is computed for both vectors $dx$ and $dy$ and two grids of interpolated dots are obtained which represents respectively the maps along X axis and Y axis. Finally, the two calculated maps are merged together by performing a Radial Basis Function (RBF) for surface to interpolate pixel resolution distortion map. An example of synthetic and calculated distortion map is illustrated in Figure 3.18.

It is important to highlight that only valid data are considered when the distortion map is computed. The interpolation process takes into account the whole image domain defined by the regular grid, however, the data are restricted in the area of the calibration target which means that inconsistent values are introduced when null values are included in the computation process. To avoid this, a processing mask is implemented which neglects invalid data from the last interpolation.

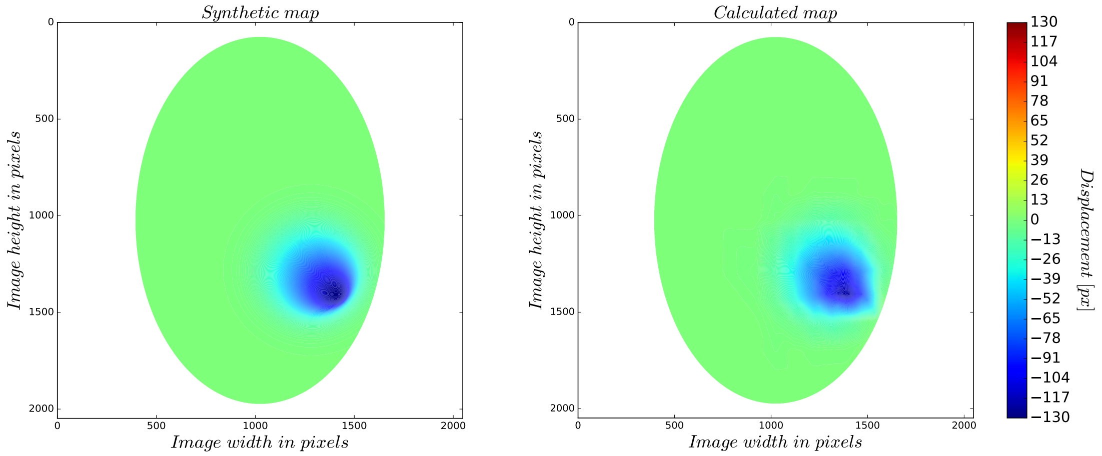

**Figure 3.18:** Example of Synthetic and Calculated maps of 128x128px distortion. The contour level indicates the distortion displacement in pixels.

Looking closer at the contours, the outcome of the extraction procedure is in a good agreement with the correspondent synthetic map which demonstrates the capability to extract distortion map based on the identification of features in calibration images. In order to understand better how good is the reconstruction process, quantitative errors are defined as part of the assessment study and their definitions are provided below.

## 3.6 Error Quantification

As already mentioned above, it is part of the correction method to establish whether or not the final outcome is consistent with the original inputs. There are two main approaches to assess the method performance which can be broadly classified into qualitative and quantitative analysis of the errors. The first one can be performed by simple visual comparison between the corrected image and the clean calibration target, while the quantitative analysis consists into systematically calculate the error among the no distorted input and the corrected output. In this study, two quantitative errors were defined based on the position of the markers in the calibration targets and the distortion maps which are described in this section.

### 3.6.1 Dot Position Error

The purpose of the performance analysis is to quantify the effectiveness of the new method to correct optical distortions occurring in calibration targets and PIV images. Ideally, the final outcome of the correction method should match perfectly with the clean calibration target used as input. Of course, as the method is based on interpolations process, errors are inevitable in the corrected images which induce discrepancies in the marker positions. In this case, a suitable error definition based on the centroid positions of the dots was defined as Dot Position Error (DPE). Essentially, the coordinates of the markers in the corrected target are extracted by performing feature identification algorithm and then compared with the clean case. The dot position error is computed as:

$$DPE = \sqrt{dx^2 + dy^2} \tag{3.10}$$

Where $dx$ and $dy$ are the differences between the clean coordinates and the corrected ones:

$$dx = x_{clean} - x_{corrected} \tag{3.11}$$

$$dy = y_{clean} - y_{corrected} \tag{3.12}$$

This index is representative of how accurately the method is able to recover the position of the calibration markers when those are shifted due to optical distortions. It is important to highlight that the dot position error is defined at target resolution which means that no information about how good is the calculated distortion map cannot be found. For visualisation purpose, the dot position error calculated for each marker in the calibration target is converted in structured data in order to have a better view of the overall error in the whole calibration plate. An example of dot position error map is presented in Figure 3.19. It is worth to say that no analytical model or prior information are required to compute this error which is simply based on the markers' position of the target plate, therefore, it is a suitable error quantification approach for experimental data.

The method assessment has been conducted considering the maximum dot position error in the whole image expressed in pixels. The analysis results are shown in §4.1.

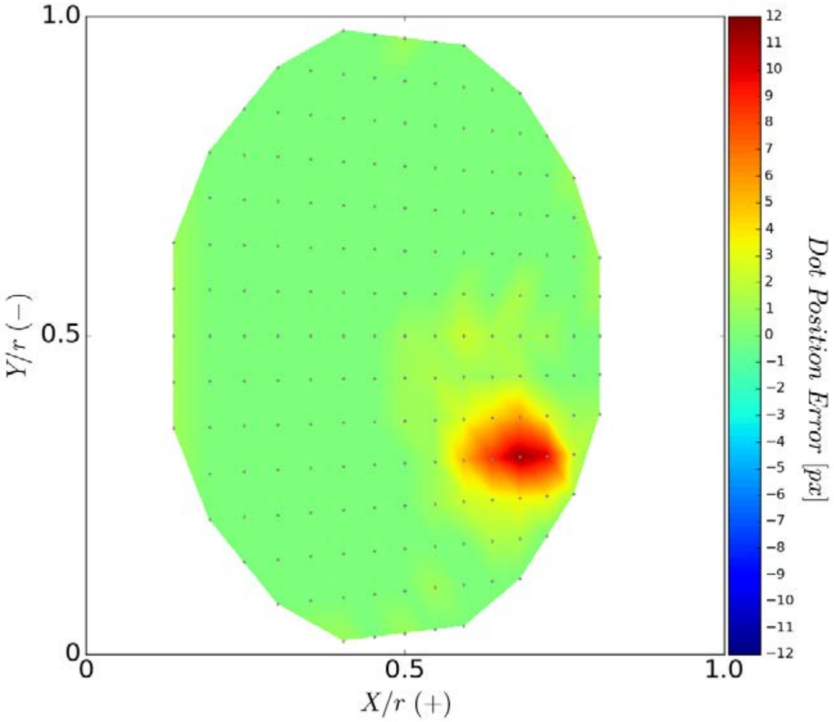

**Figure 3.19:** Example of Dot Position Error (DPE) expressed in Pixels.

### 3.6.2 Mapping error

As stated above, the dot position error does not take into account how the extraction procedure performs. In order to have a complete error analysis, the mapping error was defined by comparing directly the calculated distortion map with the synthetic distortion map applied to generate the distorted cases (see Figure 3.17). Even though the concept behind the mapping error itself is simple, the computational procedure to achieve that is not straightforward and several operations already employed in the extraction map procedure are here required. One of the main difficulties is that the synthetic maps are expressed in clean coordinates while the calculated maps are defined in the distorted coordinates. In this condition, the two maps are not consistent and a preliminary conversion must be taken for one of the maps. Particularly, the synthetic map is adjusted and expressed in terms of distorted coordinates before computing the error.

The conversion process subtracts $dx$ and $dy$ as defined in §3.5.1 from coordinates and resamples the data by linear interpolations. Moreover, as the comparison takes place in distorted image plane the synthetic map has to be considered in opposite direction which means that a changing in map sign is required. Once the maps are expressed in the same image plane, the error is computed simply by differences in both X and Y axis and the relative statistics can be calculated. Following the same line of thoughts discussed in the previous sections, only the valid data are taken into account in the error statistics, therefore an elliptic mask has been applied to the mapping error. In agreement with the dot position error, only the absolute maximum error expressed in pixels has been considered in the method performance assessment.

The definition of mapping error allows having a better view of how the method captures the distortion function based on the information given by the markers. In addition to that, a more sensible evaluation of the effect on PIV images can be derived by looking at the mapping error instead of dot position error since the former one is calculated at pixel resolution.

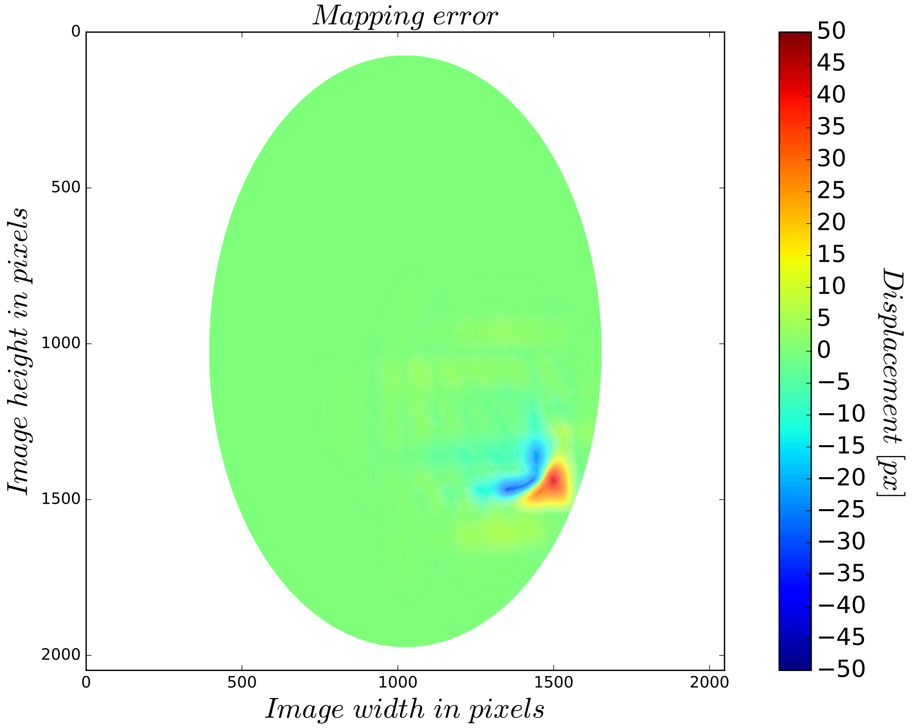

**Figure 3.20:** Example of Mapping Error expressed in Pixels.

# 4 Synthetic local distortion study

*In this section, the results obtained with the Feature Identification correction method are presented. As first, the analysis of the method performance to correct optical distortion in synthetic calibration images is assessed, giving a quantitative overview of the pipeline effectiveness. Then, the impact of localised optical distortion on synthetic PIV measurements is discussed and supported by a representative example chosen from the validation test matrix described in §3.2.2, including an exhaustive summary of the study and relative achievements.*

## 4.1 DPE and Mapping error results & discussion

The validation procedure explained in Chapter 3 aims to test Feature Identification correction method for various types of local distortions and provide a quantitative analysis of the impact on the PIV measurements. The study is based on clean and distorted synthetic calibration images for Left camera generated as described in §3.1 and their equivalent distorted DDES S-PIV velocity profiles.

In general, the correction procedure extracts the distortion map from the clean and the distorted images and applies the inverse map in order to remove the local distortion. The same function is then applied to the correspondent synthetic PIV snapshots, producing the corrected 3D velocity profiles. Quantitative evaluation of the overall error in the method performance assessment is conducted following the two definitions of dot position error and mapping error as illustrated in §3.6. The main difference is that dot position error is expressed in dots resolution which represents an index of the markers position deviation from the clean case. Mapping error, instead, is defined in pixels resolution, allowing to show better the calculated distortion map in comparison with the analytical model.

### 4.1.1 Dot Position Error (DPE)

The first analysis conducted to assess the effectiveness of the method was a direct comparison between the corrected image and the clean image. The evaluation was performed based on the DPE values calculated considering the centroid coordinates of each marker previously detected by the feature identification algorithm. In general, errors are recorded where the localised distortion was taking place as is shown in Figure 4.1. Nevertheless, when examining cases with the same distortion amplitude but different extensions, the error tends to become smaller as a function of the distortion distribution. This indicates that the distance between each marker is an important factor that can affect the final outcome of the method. High gradient local deformations cannot be reconstructed properly whether the phenomena manifest partially or at all changes in the dots displacement which is strongly related to the number of the dots available in the calibration plate.

At first glance, in the example reported below, the dot position error is lower than 10 pixels on the overall image, reaching the lowest DPE value for the high extension case.

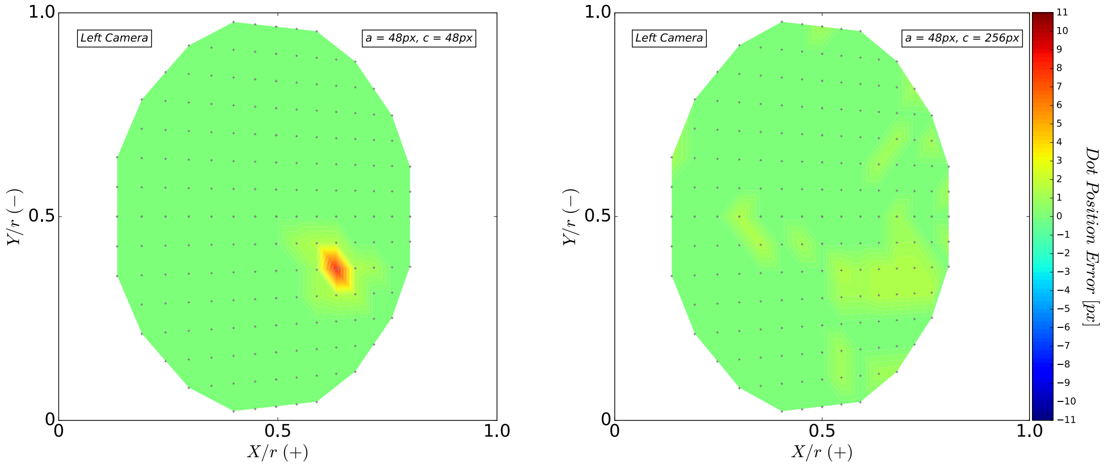

**Figure 4.1:** Dot Position Error: 48x48px (Left) and 48x256px (Right).

Interestingly, the method is able to recover successfully the location of the markers, especially, when the distortion affects a large area of the image, however, looking carefully at the case 48x256px (right), some noise can be noticed over the whole image. This effect may be related to the extraction process of the distortion map which assumes a linear interpolation. Moreover, the noise enlargement seems increasing accordingly with the distortion extension. Since the level of error introduced in the image is very low, few pixels in the marker displacement, this residual noise can be neglected for the scope of the analysis and further investigations should be assessed.

Another factor that influences the accuracy of the repositioning process is the shape of the features. Very aggressive localised distortion induces stretches and shape deformations in the markers which cannot be recovered completely. An example is reported in Figure 4.2. It can be seen that for high gradient distortions, markers in the corrected image are still deformed even though they are in the right position, representing an additional source of error in the DPE map. Possible improvements could be noticed by employing denser calibration targets which may help to capture better the distortion gradient.

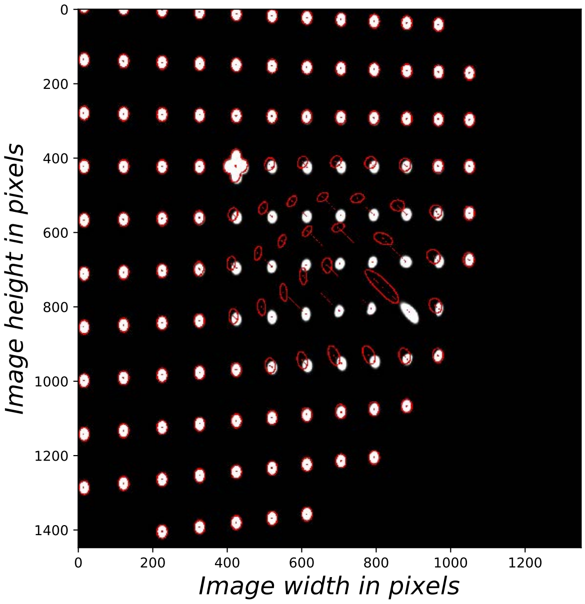

**Figure 4.2:** Residual deformation of the features in the corrected image.

To conclude, it can be stated that reductions of the maximum displacement are experienced within 10px in the overall corrected image which denotes that the developed method is able to extract properly the distortion map based on the calibration markers. To understand better the correction performance, however, the attention must be moved to the mapping error analysis reported below.

### 4.1.2 Mapping Error

Optical distortions deteriorate PIV images at pixels resolution, therefore, it is important to assess the method considering the capability to derive the distortion map based on the calibration patterns. The analytical expression of the applied local distortion is the Gaussian function described in §3.2 with symmetric extensions along the X and Y axis, which results in a circular profile in the 2D contour. Then, the distortion maps calculated are compared with their equivalent synthetic models and a quantitative error is computed following the definition reported in §0.

**Figure 4.3** shows representative results for the X coordinate of the mapping error analysis. Noticeably, in the high gradient distortion case (Left), the distortion map calculated differs largely from the synthetic equivalent due to the extrapolation procedure that assumes a linear function to interpolate the marker coordinates.

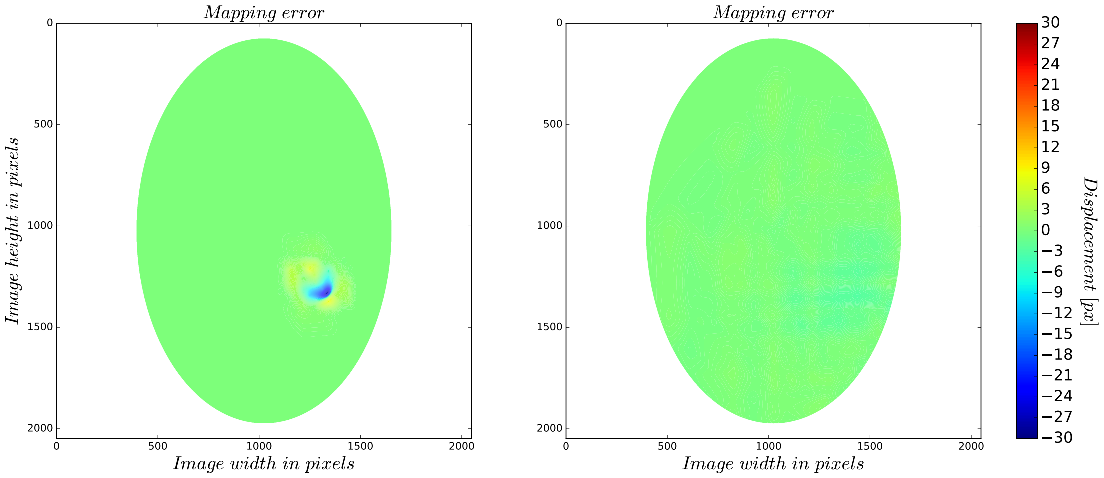

**Figure 4.3:** Mapping error results: 48x48px (left) and 48x256px (right).

As a result, residual distortions still affecting the corrected images at pixel scale resolution even if the markers are correctly allocated in the original position. The difference is relatively big, up to 40 pixels, compared with the dot position error which is a more optimistic evaluation of the error. Under the PIV point of view, mapping error is relevant to evaluate whether the distortion can be successfully removed or not, considering possible actions on the distortion extraction process due to the fact that it gives a better representation of the effect on the seeding particles images.

In Figure 4.4, a summary of the maximum mapping error is presented for the all test matrix.

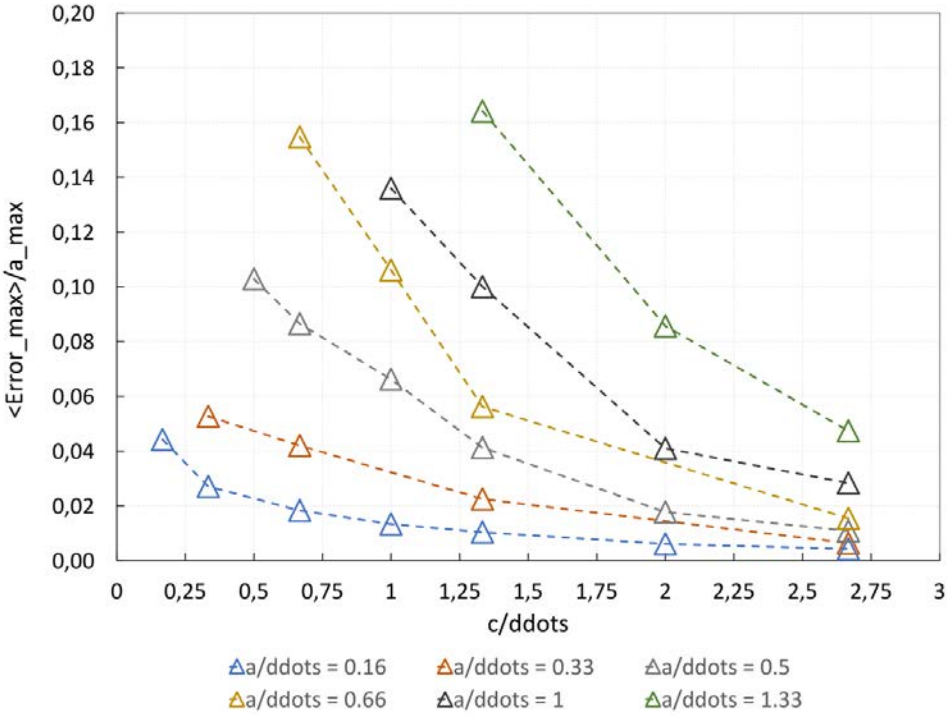

**Figure 4.4:** Maximum mapping error statistics normalised by the peak displacement. the distance between the dots (ddots) is assumed 96px.

The mapping error analysis demonstrates under the second point of view on how the performance of the method scales as increasing the extension of the local distortion. The lack of information given by employing calibration targets with defined dots resolution does not permit to reconstruct exactly the distortion profile as well as to capture deformation gradients in the whole image. This argument can be seen also as a criterion to the choice of the calibration plate. The number of the dots and the pattern displacement are critical aspects for a correction procedure based on feature identification. In general, a rise in dots resolution is recommended for those cases in which high local optical deformations are present in a small region of the image due to, for example, manufacturing imperfections in the duct.

It is apparent that, considering aggressive optical distortions, the accuracy of the corrected images reduces. Overall, the correction pipeline established is able to reduce the maximum error up to 80% of the original peak displacement for the worst aggressive case, while a reduction of the order of 90% was experienced for moderate distortions. Furthermore, the developed contour detection algorithm was revealed robust enough to identify the dots with high precision, allowing to minimise artificial errors which may be included during the searching procedure.

## 4.2 Impact on PIV velocity errors

In the previous section, the performance of the optical distortion correction method was discussed, outlining the three main factors that influence the accuracy of the results and the effectiveness of the overall method. To have an exhaustive view of the real benefits on mitigating optical distortion in the PIV measurements, a DDES S-PIV dataset affected by optical distortions from the evaluated test matrix was corrected by applying the extracted distortion maps. In this section, a discussion on the impact of local optical distortions on the PIV accuracy is presented, providing significative examples and the complete assessment of the pipeline established.

### 4.2.1 Object Plane Velocity Analysis

The main objective of this analysis was to quantify the effect of optical non-linearities on the S-PIV images when this is applied for internal flow measurements. Many sources of error can occur in the reconstructed 3-D velocity profile due to low-quality images as presented in §2.3 and the majority of them are related to the PIV evaluation process and the calibration procedure which struggles when severe prospective and localised distortions are present. The statistic in the object for this analysis is the absolute 3-D velocity magnitude normalised by the aerodynamic inlet plane (AIP) velocity taken as a reference value and the relative error computed as the difference between the absolute velocity profile of the clean and distorted cases.

The first outcome that appears clearly from the analysis is that two different errors modes are experienced when optical distortions deteriorate PIV images. Optical distortion can either provoke high localised velocity errors in the reconstructed velocity field or a complete failure of the calibration procedure which induces large spread errors over the whole outcome. In order to distinguish which aspect of the S-PIV evaluation is more susceptible to different types of optical deformations, these two errors will be treated separately.

Focusing on those cases where the calibration does not fail to de-warp the 2D velocity components in the object plane, the effect of distortions in the PIV velocity profiles and relative error is reported in the first row of Figure 4.5. As already anticipated above, only the small region where the distortion occurring experienced high-velocity vectors which are clearly physical sense inconsistent. In addition to that, the impact of localised distortions on the velocity errors becomes weaker as increasing the extension of the distortion.

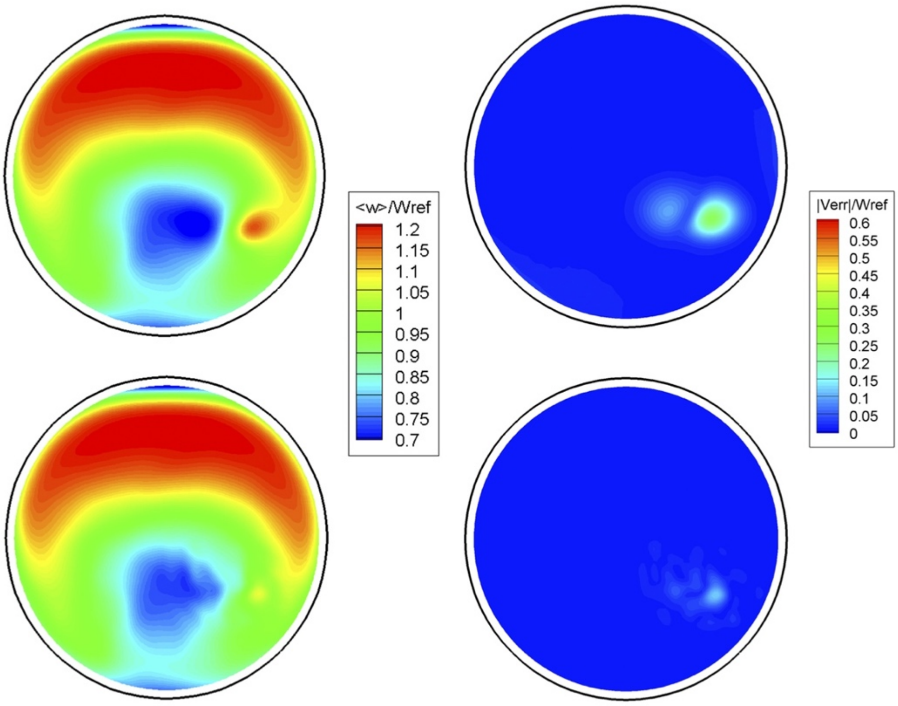

**Figure 4.5:** High localised velocity error due to 48x96px local distortion. Distorted and Corrected profiles are reported respectively in the first and second row with the relative absolute velocity errors. The values are normalised by the actual reference velocity assumed as equal to the clean case. Wref = 113 m/s.

For sake of brevity the rest of the results for a = 48px are reported in Appendix B. Looking at the velocity profiles and their relative errors, there is a clear pattern where the effect of optical distortions is reduced when this is distributed in a larger area. According to this, relevant discrepancies were recorded for high gradient distortions while not significant changes could be noticed for small distortion with high extent. A better view of this behaviour and its implication can be seen considering the number of vectors with more than 5% of error in the PIV velocity profile. Figure 4.6 shows the results summary for those cases where calibration failure is not experienced.

Noticeably, the error introduced due to local deformations on the seeding particle images is a function of the ratio c/ddots, reaching a maximum before decreasing for high value of the parameter c. Interestingly, the error magnitude for the distorted cases is around 5% with one exception represented by the most aggressive distortion which reached up to 12%. In general, PIV measurements are considered valid when the error in the overall velocity profile is beyond the limit of 5%, which can be concluded that for almost those cases where the distortions are relatively small, no specific actions need to be taken. Following the same line of thought presented above, the corrected results by performing feature identification method were assessed and reported as dash lines.

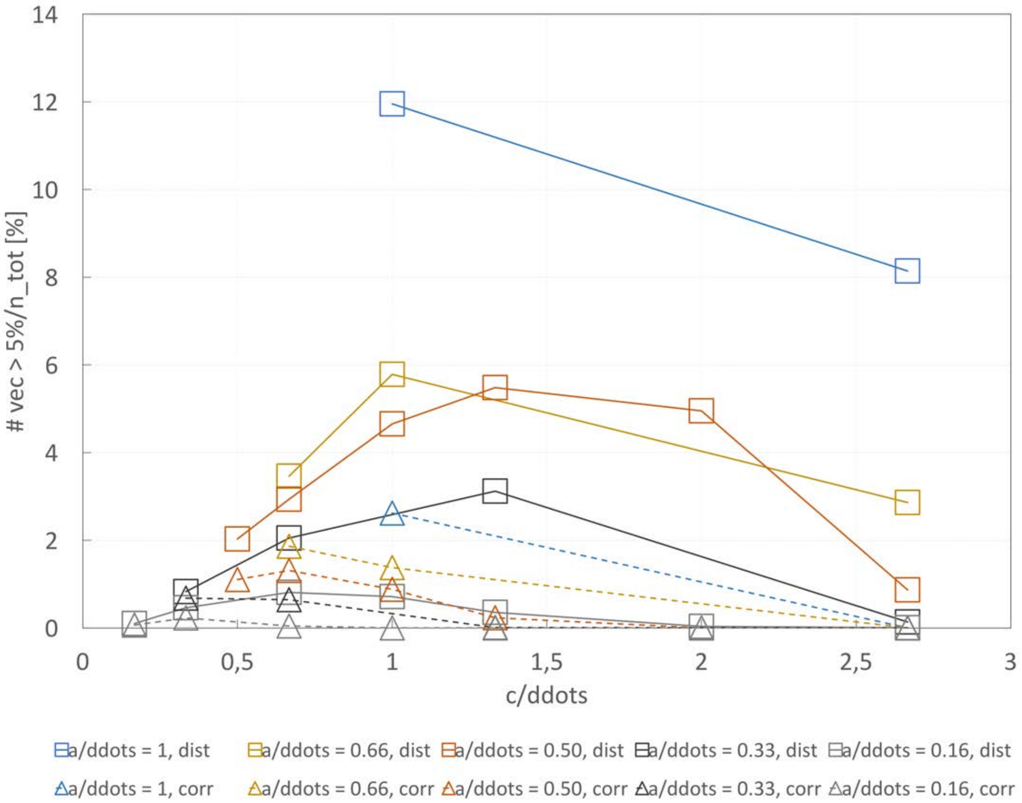

**Figure 4.6:** No calibration failure cases: number of vectors with error > 5%. Total number of vector equal to 7919.

It is obvious from the line chart that by applying the correction procedure, the error drops to around one per cent. This can be noticed also from the contours reported in Figure

4.5, where the localised velocity errors are significantly reduced after the correction. In terms of method performance, the pipeline established removed in the worst case 80% of the vectors with more than 5% of error, while a complete correction of the velocity profile is achieved for smoother distortions. As already seen in the previous section, PIV velocity errors seem to agree with the mapping error presented in Figure 4.4. It is not surprising that higher is the discrepancy between the calculated map and the synthetic model, higher will be the error in the corrected PIV velocity profile. Despite this, the mapping error still gives a pessimistic view of the actual performance of the method to correct optical distortion in the PIV images. Moving forward on the calibration failure analysis, the characteristic PIV velocity profile of the S-Duct is not anymore distinguishable due to the breakdown of the de-warping process.

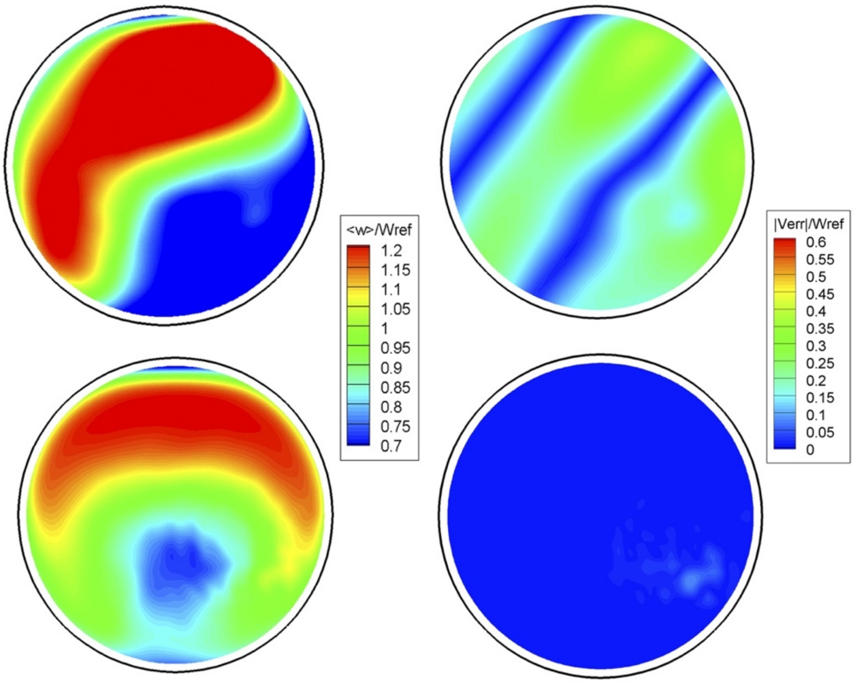

**Figure 4.7:** Calibration failure due to 64x128px local distortion (first row). Correspondent corrected velocity profile (second row).

The calibration procedure implemented in the *4G Insight*$^{TM}$ software [35] reconstructs the out-of-plane displacement vectors in the object domain from the in-plane domain of each camera as described in §2.2.1. In general, a third order of polynomial function is employed to approximate the position of the markers which can deal partially with optical non-linearities, introducing another source of error in the final outcomes, as largely demonstrated in previous works [6]. For high local distortions, however, the calibration procedure fails completely to map the object plane to the image plane, determining inconsistent results. An example of calibration failure is reported in Figure 4.7.

When aggressive deformations occurring, the reconstructed 3D velocity profile is not in agreement with the actual profile computed from clean images. In this condition Stereoscopic Particle Image Velocimetry is not feasible and actions must be taken in order to recover the raw data. The results of the correction procedure for calibration failure cases are summarised in Figure 4.8.

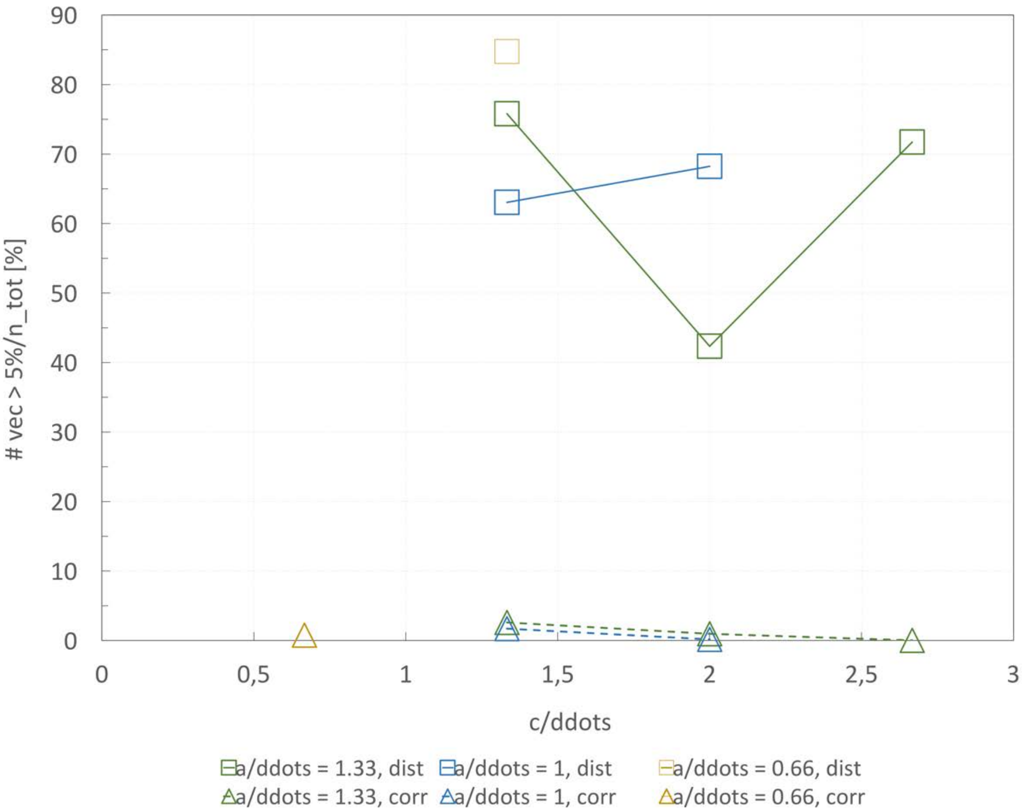

**Figure 4.8:** Calibration failure cases: number of vectors with error > 5%. Total number of vector equal to 7919.

It appears that considerable improvement in the statistic as well as in the velocity profile was achieved after the correction process. In particular, for the representative case reported above, more than 90% of the error present in the distorted case was successfully removed, recovering completely the velocity profile. Looking at Figure 4.8, before the correction, 85% of the vectors were affected by more than 5% of error while in the corrected profile no vectors experienced significant discrepancies from the clean velocity flow field. The same trend was found for more aggressive cases, where the velocity errors reached up to 3% after the correction. This leads to the conclusion that the proposed method to mitigate optical distortions is effectively beneficial to reduce uncertainties in the PIV measurements, allowing to apply the PIV technique to possible experimental setups with high optical deterioration effects, which is the case of the complex ducts research.

In order to quantify the effectiveness of the method to correct optical distortions in the PIV images, the number of vectors with more than 5 % of error successfully removed was computed as follow:

$$N_{removed} = \frac{N_{distorted} - N_{corrected}}{N_{distorted}} \tag{4.1}$$

Where $N_{distorted}$ and $N_{corrected}$ are the number of vectors with above 5% of error for the distorted case and corrected case, respectively.

Figure 4.9 depicts quite clearly in which cases the method performs well. As already widely discussed the ratio between the extent of the distortion and the dot resolution of the calibration target contributes in the method performance. In general, the same trend experienced in the pipeline assessment can be here noticed from a different point of view. Smoother distortions are captured better by the algorithm which is able to remove up to 100% of the errors. Moving close to the left side of the chart, the effectiveness reduces below 50%. Two main factors can justify this behaviour.

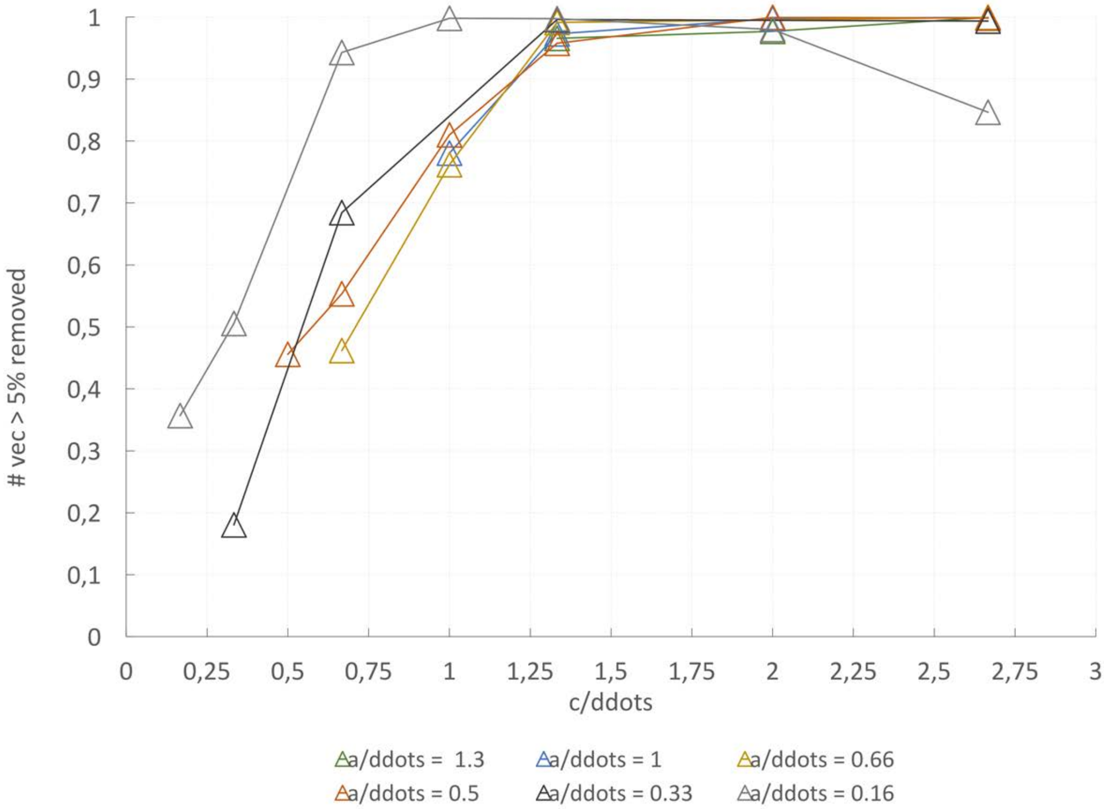

**Figure 4.9:** Number of spurious vectors (error > 5%) successfully removed by feature identification correction method.

In presence of small distortions, the code struggles to extract properly the inverse map as demonstrated in the previous section as well as for high gradient deformations. The main reason is related to the coarse marker distribution chosen for the analysis. Finer grid in the calibration target helps to capture better optical phenomena and to reconstruct accurately the distortion map. For these cases, however, the level of error introduced in the PIV measurements is relatively low even without corrections, therefore, no particular effort was spent to improve the outcomes. Few pixels deformations in the seeding particles images as represented by the a/ddots = 0.16 and a/ddots = 0.33 cases, determine up to 3% of error in the PIV velocity profile which does not either compromise the accuracy of the measurements and justify any specific actions.

Overall, an effective optical distortion correction method based on feature identification has been successfully developed, providing a possible solution for high accuracy PIV measurements. To conclude the out-of-plane analysis, it is important to highlight that local optical distortions become important in the PIV technique imaging through transparent surfaces when high gradients and shears deformation occurring in a sensible magnitude scale, inducing high localised velocity errors or failure of the calibration procedure which is predominantly the cause of drastic changes in the out-of-plane velocity profile. In order to have a better understanding of the cause-effect relationship between optical non-linearities and PIV velocity errors, a step back on the PIV evaluation pipeline must be analysed, looking at the image plane velocities.

### 4.2.2 Image Plane Velocity Analysis

In this section, the analysis of the image plane velocity profiles is discussed. The Stereoscopic PIV evaluation process can be separated into two different phases, correlation process and calibration procedure, as widely described in the literature survey. The snapshots of the seeding particles are cross-correlated to get the image plane velocity profile of each camera and then back-projected in the object plane by mean of the stereo calibration procedure which reconstructs the out-of-plane component.

Bering in mind this, different answers can be found looking just at the image domain velocity, excluding the de-warping process from the analysis. The same line of thoughts applied to assess the 3-Components velocity vectors was used to quantify the error in the 2-Components velocity profiles due to local optical distortions. For sake of brevity the results of the image plane velocity study for the a = 48px case are reported in the Appendix B.3 and only the statistics are here presented. It is important to remark that two image plane velocity profiles are needed to compute the out-of-plane component which is provided by two different cameras. Since optical distortions can occur independently in every single view, synthetic optical distortions were applied only to the left images, assuming without alteration the right ones.

In Figure 4.10, the comparison between the image plane and object plane velocity errors for the distorted and corrected cases is shown, considering the maximum absolute velocity error. Looking at the graph on the left, it can be noticed that the maximum velocity error does not change pattern when the 3D velocity is computed, reducing as a function of the distortion extension.

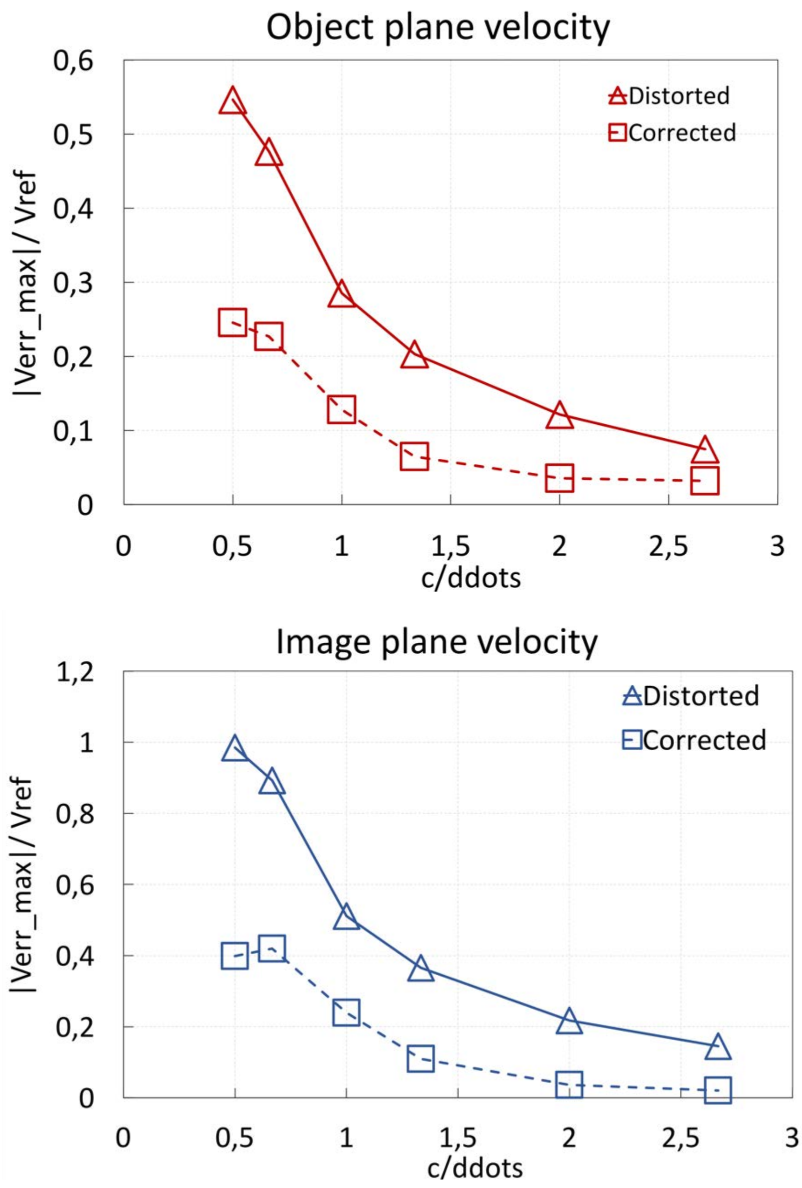

**Figure 4.10:** Maximum velocity error for object plane (Top) and image plane (bottom) analysis. The dashed line represents corrected results, while the solid line identifies the distorted cases (a = 48px). Vref is 117 m/s and 2.5 pixels/Δt for respectively object and image domains.

This demonstrates that in case of no calibration failure, significant errors are not introduced by optical distortions when projecting in the object plane. As a result, local optical distortions affect predominantly the correlation process. This argument can be generalised for the whole test matrix even those cases where the calibration procedure fails. Since Particle Image Velocimetry is based on statistical correlation of subregions images, the velocity vectors may be biased due to correlation occurring between unmatched particles, particle overlap and particle entering and exiting the sample volume in the time between exposures. All of these situations can be introduced by optical distortions when imaging through a medium due to the light refraction or manufacturing imperfections of the surfaces.

As expected the corrected results experience lower maximum errors in the velocity field for both cases. Noticeable, the correction method is able to reduce the maximum error up to 63% considering the image domain, while lower performance is recorded for the object plane analysis, up to 30% of correction. Moreover, the results in the Appendix Figure B.5, shows clearly that the level of errors in the image plane velocity appears sensibly higher compared with the 3-C velocity. The reason behind this is not clear and further systematic investigations are necessary, however a possible interpretation of this finding is that the non-linear transformation applied to pass from the image domain to the object plane during the calibration process reduces partially the overall errors.

Considering the number of anomalous vectors for both cases reported in Figure 4.11, it appears that the error increases linearly as increasing the extension of the distortion, while the different tendency is recorded for the object plane velocity which decreases according to the ratio c/ddots. This reinforces even more the fact that the de-warping process is able to mitigate the effect of optical distortions when the third component of the velocity is computed. This could be justified by the fact that the calibration procedure deals partially with distortions when it extracts the markers positions from the calibration targets as stated in previous works. For small intensity and high gradient distortion no significative changes are experienced whether is the case where the polynomial fit used in the calibration procedure is involved. In this condition, the distortion affects few markers of the calibration targets which do not give contributes assuming a polynomial function.

As a result, the number of vectors with error > 5% is comparably the same for both cases. Moreover, smoother distortions are likely inclined to be approximated better by the fitting curve which could be beneficial to reduce inconsistencies in the object plane velocity profile, agreeing with the error behaviour represented in the figures.

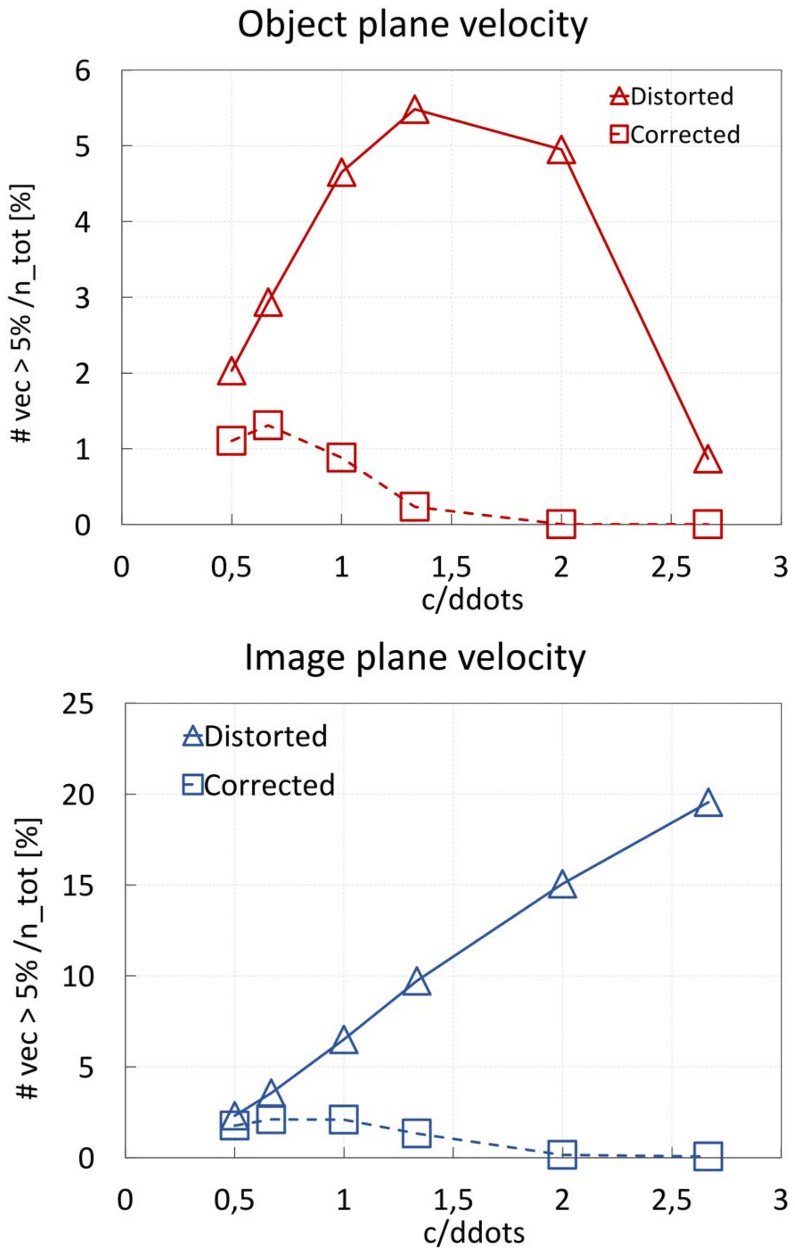

**Figure 4.11:** Number of vectors with error > 5% for object plane (left) and image plane (right) analysis. The dashed line represents corrected results, while the solid line identifies the distorted cases (a = 48px). Total vectors are 7919 and 7404 respectively.

Looking close at the graphs, the number of vectors affected by more than 5% of error is reduced in both planes after performing the correction method, however, the best performance in the object plane is around 5% against the 20% recorded for the image plane velocity. This fact justifies farther more what has been stated above. Calibration techniques give a positive contribution to drop down the errors on PIV measurements due to optical distortions and this may be related either to how the error propagates when the third component is computed and the capacity of the polynomial function to capture the distortions.

Interpreting this results in terms of method assessment, Figure 4.9 presented in the previous section overestimates the effectiveness of the feature identification method which is not the only factor that affects the corrected outcomes. In general, although part of the correction is caused by the de-warping procedure, feature identification method still removes most of the optical distortion from the seeding particle images, revealing an effective method to reduce correlation biased due to optical non linearities in the PIV measurements and avoid calibration failures which could make impossible the employment of the PIV technique.

## 4.3 Conclusions

In the previous sections, results and discussion of the optical distortion correction method based on feature identification performance were presented as well as the relative impact on PIV velocity errors. In the former study, the results showed that the developed method is able to recover the markers displacement when this is altered due to optical distortions. The assessment based on synthetic calibration images previously distorted by applying 2-D Gaussian distortions demonstrated that information about the dot coordinates were enough to extract consistent distortion maps from images. In terms of accuracy, the results were in a good agreement with the clean case even though residual errors were recorded looking at both the calculated maps and the corrected images. Considering the dot position error analysis presented in § 4.1.1, the discrepancy between the undistorted case and the corrected one was relatively low, few pixels in the overall target image for the highest gradient distortion while a complete correction was recorded for smoothly deformations.

The same trend was also noticed in the direct comparison of the distortion maps, however, the error analysis revealed that the method struggles to capture gradients and shear deformations whether the markers density in the calibration target is too low relative to the distortion size. This ends up with coarse distortion map approximations which may result in high mapping error even though no significant discrepancies are recorded in the corrected calibration image. The only reasonable explanation for this behaviour is related to the linear interpolations in the extraction procedure. Essentially, the inverse function is calculated based on linear interpolation between the distorted points and the known original dots position which helps to relocate accurately the markers displacement rather than derive the distortion distribution.

In the second part of the study, the impact of local optical distortions on the PIV velocity errors was investigated, along with the effectiveness analysis of the correction method to improve PIV measurements accuracy. In general, local optical distortions were found to affect negatively the PIV velocity profiles in the region where the distortions took place, experiencing high localised velocity errors (Appendix B, Figure B.3).

According to the 2-Components velocity results, the effect of local distortion on the seeding particles images generates mainly correlation biased due to the reallocation of the particles in the images. This is justified either by looking at the object plane velocity for those cases where there is no calibration failure and considering the maximum velocity error in Figure 4.10. No significant errors are introduced when the out-of-plane component is reconstructed properly, which means that optical distortions involve mainly the correlation process. Movement of the particles due to optical phenomena can be seen as high displacement gradient effect [8]. Essentially, shears and gradients change the location of the particles in addition to the normal flow stream which results in a displacement gradient across the interrogation windows. This is likely to introduce biases in the data due to the fact that not all of the particles present in one interrogation window at time $t_0$ will also be present in the second window at time $t_0 + \Delta t$. This generates uncertainties in the calculated displacement. The error related to this effect has been demonstrated to be dependent on the gradient, the size of the interrogation windows and the particle image density. This conclusion is also in according to the optical error model reported in §2.3.1. In terms of velocity errors, intensity and extension of the distortion represent the two factors which influence the accuracy of the velocity profiles.

It is important to notice that large extension and low intensity distortions may have no relevant effects on the 2-C velocity profiles even though a large number of vectors are affected by more than 5% of error, while high gradient distortions may introduce localised errors in the velocity profiles with very few vectors involved.

One interesting conclusion is that biases introduced by optical distortions are mainly driven by distortion gradients. This can be noticed looking at the maximum image plane velocity error in Figure 4.10. A 2-D Gaussian distortion with magnitude and extension of 48x48 pixels introduces a maximum bias approximately of 3 pixels average which is relatively small if compared with the maximum peak displacement of 68 pixels introduced and calculated by the Eq. (3.7). Moreover, increasing the extent of the distortion the maximum velocity error reduces according to the gradient reduction. This implies that the error cannot be related just to the distortion peak but it must be linked also to the gradient across the interrogation window. Nevertheless, looking at the Eq. (2.9) provided in § 2.3.1.2, the analytical expression of the velocity error results dependent on the gradient of the optical displacement vector rather than the peak displacement which remarks even more what stated above.

When the 3-C velocity is computed, however, the error introduced by optical non-linearities is partially reduced, revealing the scenario of localised distortions on PIV measurements less dramatic than the one expected. This finding is strongly linked with the capability of the calibration procedures to back-project the image plane velocity to the object plane and how errors propagate through the de-warping process. Systematic investigations about the calibration performance need to be done since a direct assessment of the causes of the error reduction cannot be evaluated based on the data available. For the cases considered in Figure 4.6, the level of error reached is up to 6% with two exceptions represented by 96px distortion.

A completely different scenario is instead depicted when optical distortions cause calibration failure. The main issue related to optical phenomena on PIV techniques was found to be the breakdown of the de-warping process rather than the bias introduced in the measurements. In this situation, the velocity profile of the flow field was not consistent with the physical behaviour and high-velocity error was recorded in the object plane data (Appendix A, Figure B.4). The analysis presented in this chapter indicates that PIV techniques are not employable for applications where aggressive distortions deteriorate the quality of the calibration images and countermeasure strategies are required to recover the raw data.

In this context, the developed correction method based on feature identification was applied to the synthetic distorted images to evaluate the real effectiveness when this is employed in the PIV pipeline. Looking at the corrected data against the results affected by distortions, relevant benefits were experienced in terms of accuracy. For those cases where localised errors were present, the method reduced sensibly the overall error in both image and object plane velocity profiles. Actual achievements, however, were seen in the calibration failure cases where the measured profiles were completely recovered after performing feature identification correction method.

# 5 Experimental optical distortion study

*In the previous chapters, the effect of optical distortions in both object and image plane velocity was discussed, proving the capability of the correction method to deal with different types of distortions and successfully reduce the level of errors in the PIV velocity profiles. The developed validation procedure based on the synthetic images illustrated in §3.2 gives a suitable approach to widely demonstrate the general idea of the new correction pipeline, however, no assertions can be made when real experimental data are employed. In order to prove the effectiveness of the method in a real scenario, a set of experimental calibration images were used as a testbench and the discussion of the analysis is here reported.*

## 5.1 Results and discussion

The project aims to establish an effective optical distortion correction method based on feature identification algorithm as part of the already existent PIV procedure which can remove optical deformations in actual seeding particles and calibration targets images, ensuring high accuracy PIV measurements. In this context, it has been widely demonstrated the capability of the new method to correct synthetic data, proving the tool performance when this is applied for a variety of localised distortions. Purpose of this analysis is to extend the method assessment to experimental calibration images and therefore validate the correction toolkit in actual conditions.

In essence, the approach adopted here takes into account optical phenomena occurring in the calibration targets when different working sections presented in §3.3.2 are employed. Since optical non-linearities are strongly related to geometric and manufacturing properties of the working section, different levels of distortion were experienced in the target images for both left and right cameras, classified as Cylindrical duct distortions. Following the same sequence of actions taken in the synthetic analysis, the distorted experimental calibration images were corrected by performing the correction pipeline discussed in §3.5 and relative dot position errors were computed against the no distortion case. In order to provide a better view of the method effectiveness the distortion maps were computed also for the distorted cases. In Figure 5.1, a quantitative representation of the distortion is reported respectively for the two representative cases, Glass5 and Perspex12. Perspex5 has revealed a similar optical distortion distribution found in the Glass5 with the exception that the latter one introduces higher non-linear distortions, therefore, contours of Perspex5 are not reported and only the relative statistics will be provided in Table 5.1 as well as with the right camera results.

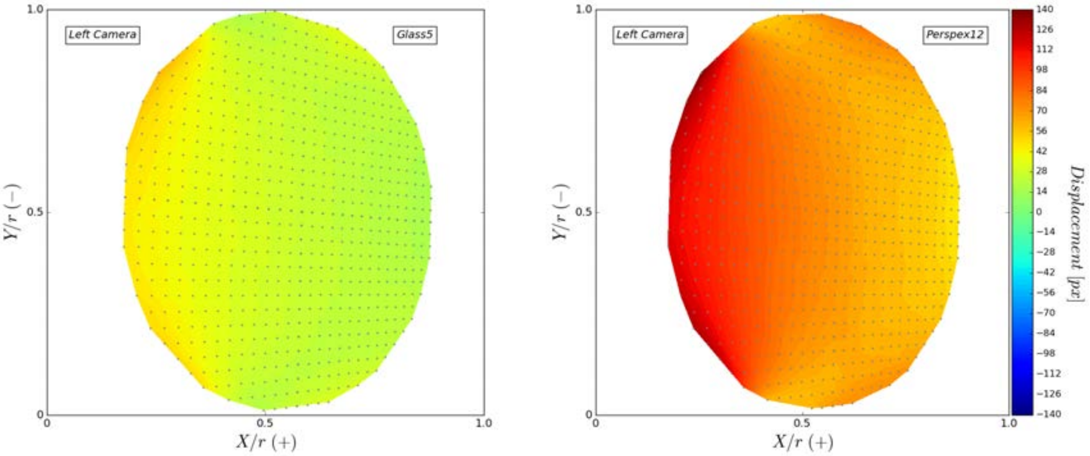

**Figure 5.1:** Experimental distortion maps of Glass5 (left) and Perspex12 (right).

Looking at the error in the markers' position, it obvious from the contours that the worst case is represented by the Perspex12 where an average error of 73px is experienced in the overall image. Noticeably, the distortions levels increase close to the borders on the left side in which the refraction is likely to be higher, causing a maximum dot position error of 140px. For the case of Glass5 the average error is sensibly reduced by approximately 60% as well as the maximum error which is still confined in the regions near the borders. It is worth to say that even though the distortions seem quite aggressive, the previous work conducted by Chasoglou A. has widely demonstrated that the registration errors introduced in these conditions are comparatively small whether the high order of polynomial functions is employed in the calibration procedure [6]. Although for the PIV point of view those cases are not really challenging, in terms of feature identification method they represented good examples to prove the correction process on actual data. The target pattern, marker spacing and features size play a significative role in a successful marker detection process which requires a careful choice of the input parameters such as window size and steps size based on trial and error approach. For the cases examined in this analysis, the algorithm managed to extract systematically the points in the Target x5y5 for both distorted and clean images, however, further upgrades are required in the detection strategy in order to facilitate this procedure.

Moving forward to the correction method results, significative improvements were recorded in the marker position as it can be noticed in Figure 5.2. In both cases the distortion level is almost null with average errors lower than 0.3px in the whole image and a maximum dot position error of 5px recorded in the most aggressive distorted case. Looking closer, the maximum residual errors are experienced in the regions where larger distortions where involved which correspond to the side of the viewing camera.

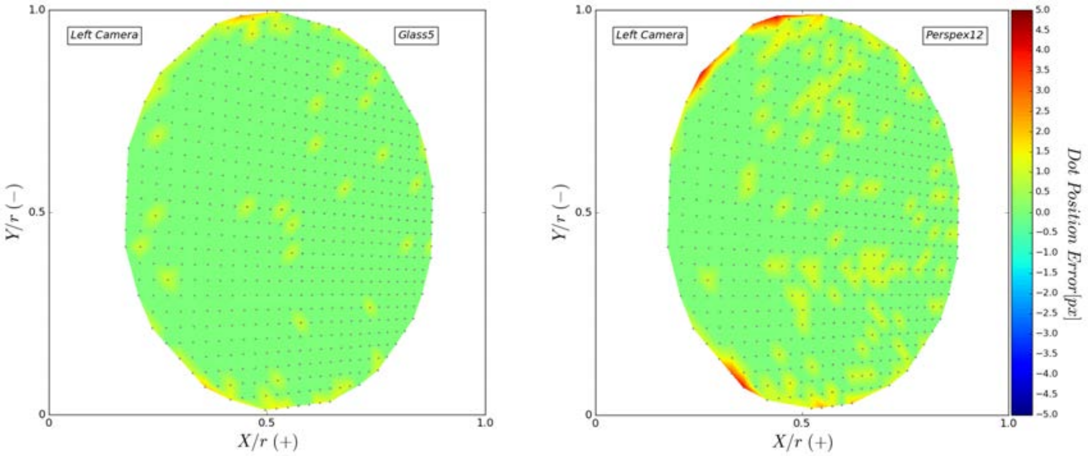

**Figure 5.2:** Dot Position Error of the corrected experimental images after performing feature identification correction method.

This could be related to multiple reasons such as bad quality of the features or low marker density relative to the distortion magnitude, however, the accuracy of the correction is still surprisingly high. Considering the amount of dot position error successfully removed from the Perspex12 image as indicated in Eq. 5.1, the worst performance of the method to reposition the markers is 96% out of 100% which is the case where the feature perfectly overlaps the original position.

$$DPE_{removed} = \frac{Max\ Dist. - DPE_{corrected}}{Max\ Dist.} \tag{5.1}$$

The same performance is recorded in the Perspex5 and Glass5 cases where the errors are comparatively smaller. In Table 5.1, the summary of the results for both Left and Right cameras are provided. As expected no significative difficulties have been noticed either in the correction approach and in the method performance when different viewing cameras were considered.

| | Left/Right | | Left/Right | |
|---|---|---|---|---|
| | Max Dist. | Max $DPE_{corr}$ | Avg Dist. | Avg $DPE_{corr}$ |
| Glass5 | 60.0/48.8 | 2.2/3.2 | 28.0/23.4 | 0.09/0.08 |
| Perspex5 | 38.9/33.2 | 2.0/2.8 | 20.2/17.6 | 0.1/0.1 |
| Perspex12 | 139.6/119.3 | 4.2/4.5 | 72.6/65.2 | 0.23/0.21 |

**Table 5.1:** Summary of the experimental results expressed in pixels for both Left and Right cameras and the three investigated working sections.

## 5.2 Conclusions

The analysis presented in this section revealed how the correction method performs when is applied to experimental calibration images. The results showed clearly the capability of the established method to correct optical distortions in actual calibration targets with surprisingly high accuracy. The distortion level removed in the worst case is around 96% considering the peak errors on the borders, while perfectly overlaps were experienced in the central regions of images where cylindrical distortions do not cause high non-linear gradients. Moreover, the feature identification algorithm has been revealed robust enough to capture automatically the markers in a finer calibration plate without additional user assistance, however, the determination of the window size and the X, Y increments in the searching algorithm has not been found straightforward as expected and several trials were required before converging to the right solution. Nevertheless, the image pre-processing toolkit has been fundamental to ensure no noisy images, facilitating the all detection process.

In terms of correction effectiveness, it can be generalised that the method performance is in agreement with the analysis conducted synthetically, which has demonstrated that the distortion extraction procedure approximates better linear marker distributions rather than highly non-linear displacements. A direct comparison of the calculated map with analytical models cannot be assessed since there is no prior information about the actual distortion map introduced in the experimental data. This fact limits the discussion only to the dot position, leaving open questions about the capability of the method to capture gradients and shear deformations across actual targets which have appeared an important aspect in the correction of PIV measurements. By contrast, the analysis demonstrates that an effective optical distortion correction toolkit based on feature identification has been successfully developed, leading to new possible applications of PIV techniques in the field of the internal aerodynamics research.

As already mentioned so far, a better comprehension of the highly distorted unsteady flow generated in complex intakes is required in the context of Boundary Layer Ingestion and Distributed Electric Propulsion concepts. High-spatial and time resolution flow measurements such as the ones provided by non-intrusive S-PIV techniques are strongly desirable for this purpose, however, no previous experiments have managed to fully investigate high convoluted ducts due to optical distortions occurring on the seeding particles and calibration images. In these terms, the correction method proposed in this study can allow to increase significantly the accuracy of PIV measurements for internal flow applications as well as opens new experimental campaigns in internal convoluted intakes aerodynamics which were not feasible before.

# 6 Summary and Future Work

The scope of the study was to develop an optical distortion correction method based on feature identification algorithms which allow improving the accuracy of Stereoscopic Particle Image Velocimetry techniques when applied to investigate internal flow aerodynamics. Besides, it was part of the study to provide a general view of the impact of optical distortions on PIV measurements when imaging through complex transparent sections, i.e. S-Ducts. The applications referred in this study are related to convoluted aero engine intakes which represent a critical aspect of design for novel integrated propulsion systems architectures which required high understanding of the flow behaviour at the aerodynamic interface plane (AIP) downstream of the intake.

Synthetic and Experimental approaches were adopted in the correction method performance assessment, while only the former one was employed to evaluate effects of optical distortions on the PIV accuracy. The dataset of distorted synthetic images, seeding particles and calibration target, was generated by assuming a 2-D Gaussian distortion model which allowed to simulate different types of localised distortions which may occur in actual experiments due to manufacturing imperfections of the duct surfaces, high thickness of the section walls and properties of the material. In the context of optical correction strategies, the new method proposed in this study was based on the idea to develop an image pre-processing toolkit which is able to remove optical non-linearities from images before undertaking commercial PIV software.

The validation process introduced in this study showed that reliable corrections of optical distortions were achieved in both calibration targets and PIV velocity profiles after performing the new method. This conclusion came after the two different investigations presented. The analysis of the dot position and mapping errors applied for synthetic calibration targets revealed how well the developed toolkit extracts distortion maps from the clean and distorted marker coordinates and the level of residual errors present in the corrected images in terms of markers distribution. it is concluded that the correction method based on feature detection algorithm recovered the position of the markers with high precision, maximum 10 pixels of DPE was recorded in the most aggressive case in the test matrix, which is not relevant to introduce significant registration errors when a third order of polynomial function is assumed during the calibration process [6]. By contrast, high shears and gradients distortions occurring in the images were not reconstructed completely in order to ensure null errors in the analysis at pixel resolution which was more representative of the possible implications in the PIV velocity profiles. Even though the calculated distortion maps were consistent with the correspondent synthetic ones and good approximations of the analytical models were achieved, the mapping errors revealed the distortion computation procedure strongly dependent on the marker density of the calibration target. The method accuracy improved up to 80% as increasing of the ratio between the distance of the dots and the distortion extent which can be linked to the pattern resolution. Under the second point of view, it can be stated that the method struggled more when high gradient distortions affected the images resulting in lower correction performance.

Moving forward to the PIV velocity analysis, several conclusions can be found looking at the results of the distorted and corrected cases. In one hand optical distortions affect mainly the correlation procedure. According to the 2-C velocity error, no changes were experienced in the trend when the out-of-plane components were computed and lower localised maximum errors appeared in the 3-C velocity profiles which means that calibration procedure, actually reduced partially the errors when no failures in the de-warping procedure are experienced. This leads to the conclusion that optical non-linearities introduce correlation biases in the PIV measurements which seems to be primarily driven by the distortion gradient across the interrogation windows rather than the peak displacement. In the other hand, very high distorted calibration images provoke the failure of the calibration software which results in completely wrong flow field profiles, imposing serious limitations to the S-PIV techniques applied for internal flow measurements.

Considering the corrected results, the level of error in the velocity profiles was sensibly reduced, up to 100% of spurious velocity vectors (vectors with more than 5% of error) successfully removed and complete restoration of the flow field velocity characteristic for those cases where the calibration failed. The error trend appeared in this case was in agreement with the one experienced in the dot position and mapping error analysis, recording the best performance for low gradient distortions. Those results widely proved the correction strategy developed in this thesis and its relative benefits in the PIV measurements when optical distortions affecting calibration and seeding particles images. Nevertheless, tests on experimental target images demonstrate the applicability of the method in the actual scenario, where noise and external factors, such as residual background and blur effects, deteriorate the quality of the images.

## 6.1 Feature Research

Same of the aspects presented in this thesis require further investigation and research. Below a detailed list of possible improvements about the feature identification algorithm and the correction pipeline is here provided:

- The current version of the algorithm requires to specify the number of markers in each row of the target quadrant in order to define when the searching window must be moved in the following row. This could be done by imposing some sort of boundaries based on the target region which allows generalising the code for different types of calibration plate. In the more recent version of the algorithm this has been already implemented, however, no depth tests have been conducted due to time constraint.

- Non-uniform distances between the dots in the vertical and horizontal axis may be the cause of failure when constant increments are considered in the scan process. Different strategies could be evaluated for this purpose, such as calculate the step size by means of predefined functions.

- In the context of high distorted experimental images, the development of semi-automatic searching strategy is strongly recommended since markers and rows may not be distinguishable. A possible solution should be to develop an interactive feature identification algorithm assisted by user actions, i.e. select manually the markers that are not identified automatically.

- The current feature identification algorithm assumes perpendicular searching directions which limit the applicability of the code when high prospective distortions affect the images. Implement the possibility to choose arbitrary directions should allow exploiting aggressive distorted cases.

Concerning the impact of optical distortions on S-PIV measurements:

- When the 3-C velocity has computed the level of error due to optical distortions reduce significantly, which means that the de-warping procedure mitigates partially the effect of the distortions. Further investigation about the calibration procedure implemented in *4G Insight*$^{TM}$ should be evaluated in terms of how the error propagates when passing from the image plane to the object plane.
- A depth investigation of the calibration performance to map correctly the object domain is suggested in order to define whether or not the calibration fails to reconstruct the out-of-plane velocity component.
- Velocity errors introduced by optical distortions are mainly related to the correlation process. Systematic analyses should be performed to evaluate the relation between optical non-linearities and correlation biases, demonstrating the dependency with distortion gradients across the interrogation windows.

# REFERENCES

[1] L. Hardin, G. Tillman, O. Sharma, J. Berton, and D. Arend, “Aircraft System Study of Boundary Layer Ingesting Propulsion,” *48th AIAA/ASME/SAE/ASEE Jt. Propuls. Conf. &amp; Exhib.*, no. August, pp. 1–12, 2012.

[2] P. K. Zachos, D. G. MacManus, D. G. Prieto, and N. Chiereghin, “Flow Distortion Measurements in Convoluted Aeroengine Intakes,” *AIAA J.*, vol. 54, no. 9, pp. 2819–2832, 2016.

[3] S. M. Soloff, R. J. Adrian, and Z. C. Liu, “Distortion compensation for generalized stereoscopic particle image velocimetry,” *Meas. Sci. Technol.*, vol. 8, no. 12, pp. 1441–1454, 1997.

[4] C. W. H. Van Doorne and J. Westerweel, “Measurement of laminar, transitional and turbulent pipe flow using Stereoscopic-PIV,” *Exp. Fluids*, vol. 42, no. 2, pp. 259–279, 2007.

[5] F. Caruso 2015, “S-duct Aerodynamics: Evaluation of uncertainties for S-duct experimental campaigns”, MSc Thesis, Cranfield University, Cranfield UK.

[6] A. Chasoglou 2016, “Experimental Aerodynamics: Application of stereo PIV for internal flow measurements through non-planar windows”, MSc Thesis, Cranfield University, Cranfield UK.

[7] R. J. Adrian and J. Westerweel, *Particle Image Velocimetry*. Cambridge: Cambridge University Press, 2011.

[8] M. Raffel, C. E. Willert, S. Wereley, and J. Kompenhans, *Particle image velocimetry: a practical guide*. Springer, 2013.

[9] R. J. Adrian, “Twenty years of particle image velocimetry,” *Exp. Fluids*, vol. 39, no. 2, pp. 159–169, 2005.

[10] A. Melling, “Tracer particles and seeding for particle image velocimetry,” *Meas. Sci. Techno.*, vol. 8, pp. 1406–1416, 1997.

[11] A. K. Prasad, “Stereoscopic particle image velocimetry,” *Exp. Fluids*, vol. 29, no. 2, pp. 103–116, 2000.

[12] C. Willert, “Stereoscopic digital particle image velocimetry for application in wind tunnel flows,” *Meas. Sci. Technol.*, vol. 8, no. 12, pp. 1465–1479, 1999.

[13] E. Hecht, *Optics*, 5th ed. Pearson, 2017.

[14] W. Zang and A. K. Prasad, “Performance evaluation of a Scheimpflug stereocamera for particle image velocimetry,” *OSA Publ.*, vol. 36, no. 33, pp. 8738–8744, 1997.

[15] M. Raffel and F. Kost, “Investigation of aerodynamic effects of coolant ejection at the trailing edge of a turbine blade model by PIV and pressure measurements,” *Exp. Fluids*, vol. 24, no. 5–6, pp. 447–461, 1998.

[16] J. Haertig, M. Havermann, C. Rey, and A. George, “Particle Image Velocimetry in Mach 3.5 and 4.5 Shock-Tunnel Flows,” *AIAA J.*, vol. 40, no. 6, pp. 1056–1060, 2002.

[17] G. E. Elsinga, B. W. Van Oudheusden, and F. Scarano, “Evaluation of aero-optical distortion effects in PIV,” *Exp. Fluids*, vol. 39, no. 2, pp. 246–256, 2005.

[18] H. Richard and M. Raffel, “Principle and applications of the background oriented schlieren (BOS) method,” *Meas. Sci. Technol.*, vol. 12, no. 9, pp. 1576–1585, 2001.

[19] A. K. Prasad and K. Jensen, “Scheimpflug stereocamera for particle image velocimetry in liquid flows,” *OSA Publ.*, vol. 34, no. 30, pp. 7092–7099, 1995.

[20] N. Amini and Y. A. Hassan, “An investigation of matched index of refraction technique and its application in optical measurements of fluid flow,” *Exp. Fluids*, 2012.

[21] R. Budwig, “Refractive index matching methods for liquid flow investigations,” *Exp. Fluids*, 1994.

[22] G. Wendt, B. Mickan, R. Kramer, and D. Dopheide, “Systematic investigation of pipe flows and installation effects using laser Doppler anemometry - Part I. Profile measurements downstream of several pipe configurations and flow conditioners,” *Flow Meas. Instrum.*, vol. 7, no. 3–4, pp. 141–149, 1996.

[23] B. J. De Witt, H. Coronado-Diaz, and R. J. Hugo, “Optical contouring of an acrylic surface for non-intrusive diagnostics in pipe-flow investigations,” *Exp. Fluids*, vol. 45, no. 1, pp. 95–109, 2008.

[24] A. Amezua 2017, “Experimental Aerodynamics: Uncertainty quantification due to optical distortion in S-PIV experiments”, MSc Thesis, Cranfield University, Cranfield UK.

[25] F. Wilson 2015, “CFD analysis of the flow field generated by convoluted ducts”, MSc Thesis, Cranfield University, Cranfield UK.

[26] S. Wellborn, B. Reichert, and T. Okiishi, “An experimental investigation of the flow in a diffusing S-duct,” *28th Jt. Propuls. Conf. Exhib.*, 1992.

[27] B. Lecordier and J. Westerweel, “The EUROPIV Synthetic Image Generator (S.I.G.),” *Part. Image Velocim. Recent Improv.*, pp. 145–161, 2004.

[28] A. Andreopoulos and J. K. Tsotsos, “50 Years of object recognition: Directions forward,” *Elsevier*, vol. 117, no. 8, pp. 827–891, 2013.

[29] P. Moreels and P. Perona, “Evaluation of Feature Detectors and Descriptors based on 3D Objects,” *Int. J. Comput. Vis.*, vol. 73, no. 3, pp. 263–284, 2007.

[30] J. Martinez, D. M. J.-C. Nebel, and C. Orrite, “Tracking Human Body Parts Using Particle Filters Constrained by Human Biomechanics,” *Br. Mach. Vis. Conf.*, pp. 1–12, 2008.

[31] G. Bradski, “The OpenCV Library,” *Doctor Dobbs Journal*, 2000. [Online]. Available: http://www.drdobbs.com/open-source/the-opencv-library/184404319. [Accessed: 10-May-2018].

[32] C. Harris and M. Stephens, “A Combined Corner and Edge Detector,” *Procedings Alvey Vis. Conf. 1988*, 1988.

[33] S. Suzuki and K. A. be, “Topological structural analysis of digitized binary images by border following,” *Comput. Vision, Graph. Image Process.*, vol. 30, no. 1, pp. 32–46, 1985.

[34] SciPy.org, “scipy.interpolate.LinearNDInterpolator,” 2018. [Online]. Available: https://docs.scipy.org/doc/scipy/reference/generated/scipy.interpolate.LinearNDInterpolator.html. [Accessed: 05-Jul-2018].

[35] TSI Inc., “Insight 4G Global Image, Acquisition, Analysis, & Display Software User’s Guide,” no. June, 2014.

# APPENDICES

## Appendix A – Extra analyses

### A.1 Multiple Iteration Procedure

The pipeline presented in Figure 3.17 can be performed as multiple iterative procedures. In the first iteration the method evaluates the distortion map starting from the distorted image and then for the following steps considers as input the corrected image of the previous iteration. The whole test matrix was corrected until the third iteration, however, no significant improvements were recorded in the final outcomes.

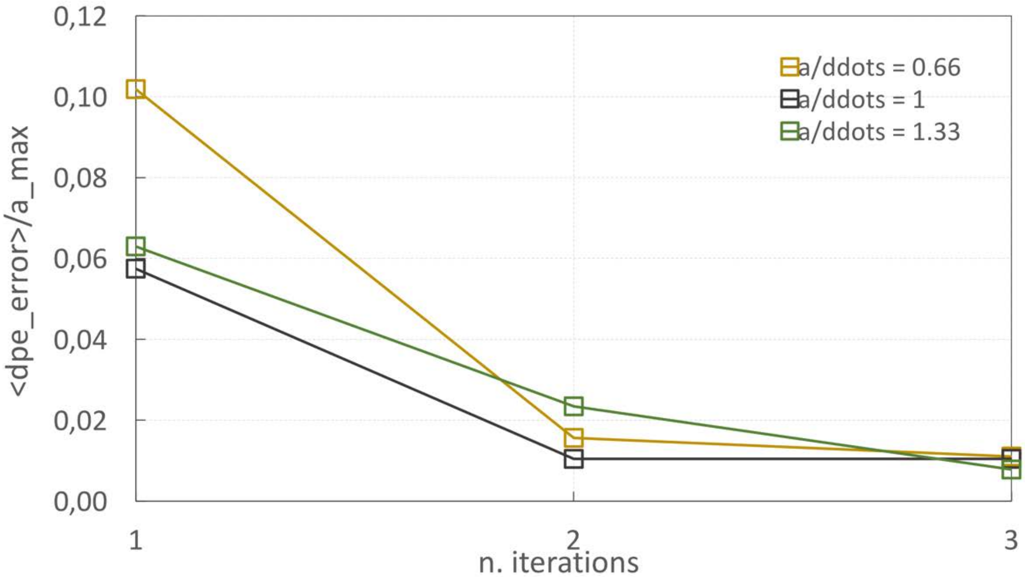

**Figure A.1:** Dot Position Error as function of the number of iterations.

shows the maximum dot position error as a function of the number of iterations for the most aggressive cases. As expected the maximum dots discrepancy between the clean and the distorted images decreases as increasing in number of iterations, reaching few percentages of the original error at the second step. Despite the fact that there is a reduction of the maximum error, very limited benefits can be appreciated in the PIV measurements, therefore, only the first iteration was considered for the discussion of the results.

## A.2 Method sensitivity to optical distortion position

No distortions can be captured since there is not any manifestation on the images which is a matter of either the grid resolution or the relative location of the peak displacement. A systematic study was conducted to assess this dependency, changing the location of the distortion peak along one coordinate axis and computing the mapping error. For this case, a local distortion with amplitude a = 32px and three different extensions c = 32px, 64px, 128px were chosen.

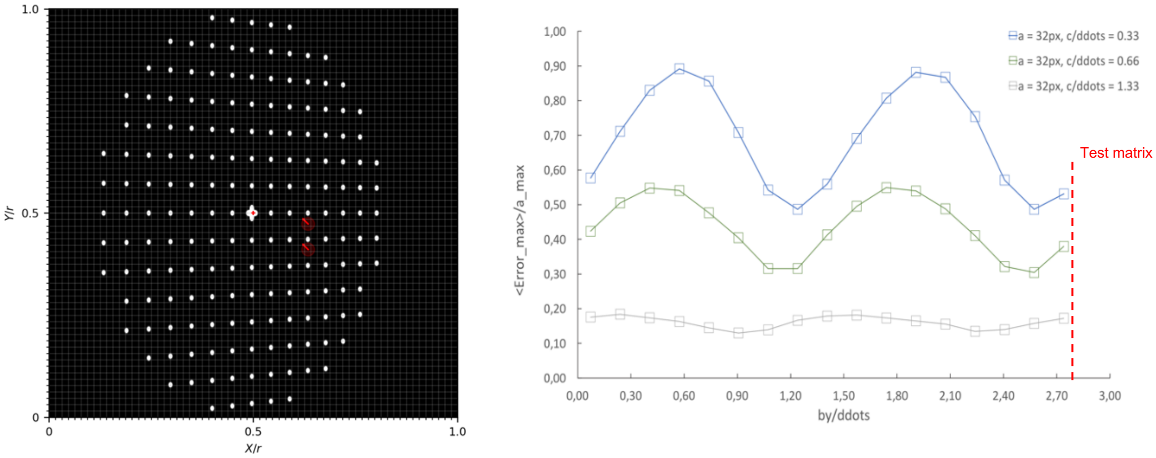

**Figure A.2:** On the left, the effect of the peak location on the maximum mapping error; on the right, a representation of the distortion location on the calibration target correspondent to the maximum errors.

In Figure A.2 the main outcome of the peak location analysis is reported. Looking at the mapping error as a function of the coordinate Y, there is a clear pattern when the distortion occurs in different position of the image. In particular, the discrepancy between the calculated map and synthetic map changes periodically as increasing in Y-axis, reaching the minimum values in correspondence of the markers. As expected, the method performs better when the dots are inside the distortion region and the correction procedure is less influenced by the relative peak location as the distortion increases in extent. The full test matrix employed in this study was created by applying a synthetic local distortion in an arbitrary location relative to the fiducial mark which is close to the best condition, as revealed by the analysis. In this situation, no errors related to the distortion peak location are included in the performance assessment.

# Appendix B - Supplementary Graphs

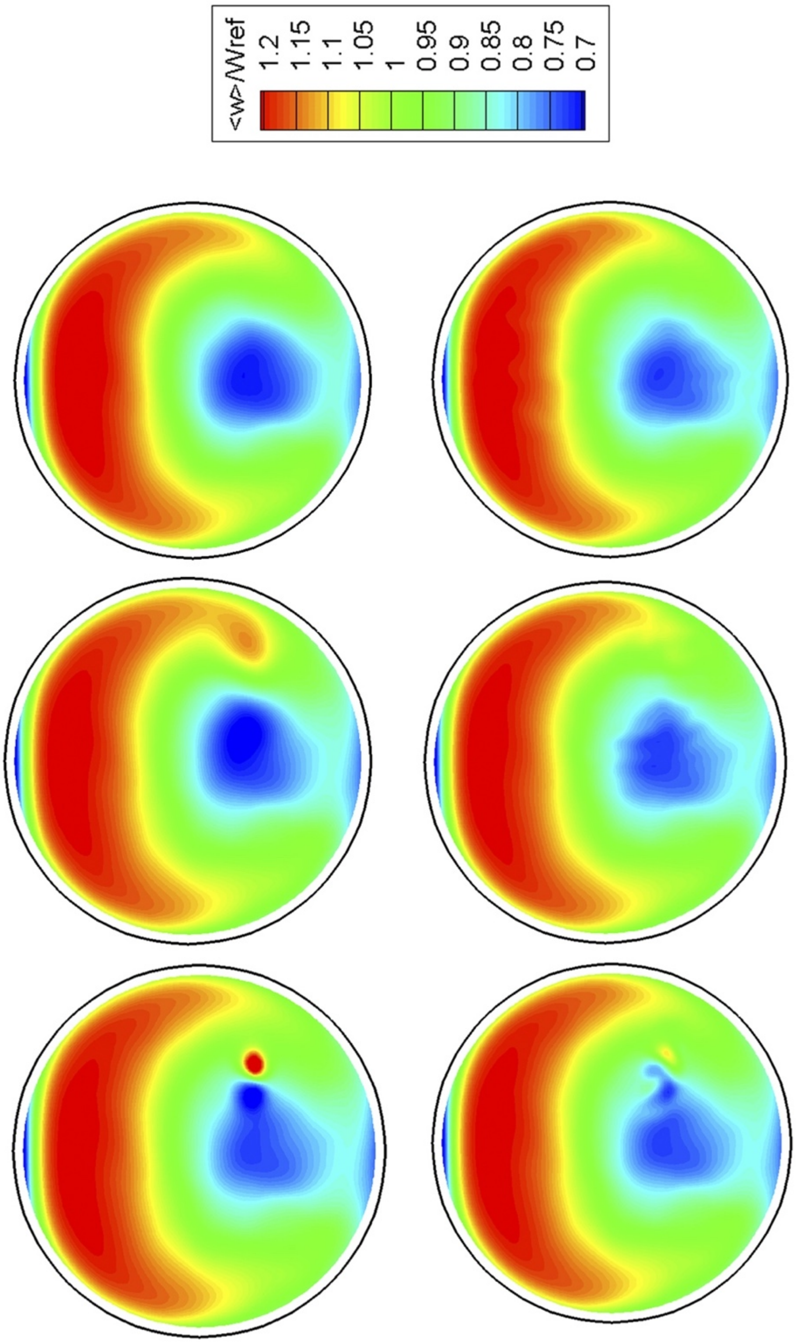

**Figure B.1:** Out-of-plane velocity. Distorted (first row) and corrected (second row) profiles for a = 48px, c = 48px, 128px, 256px.

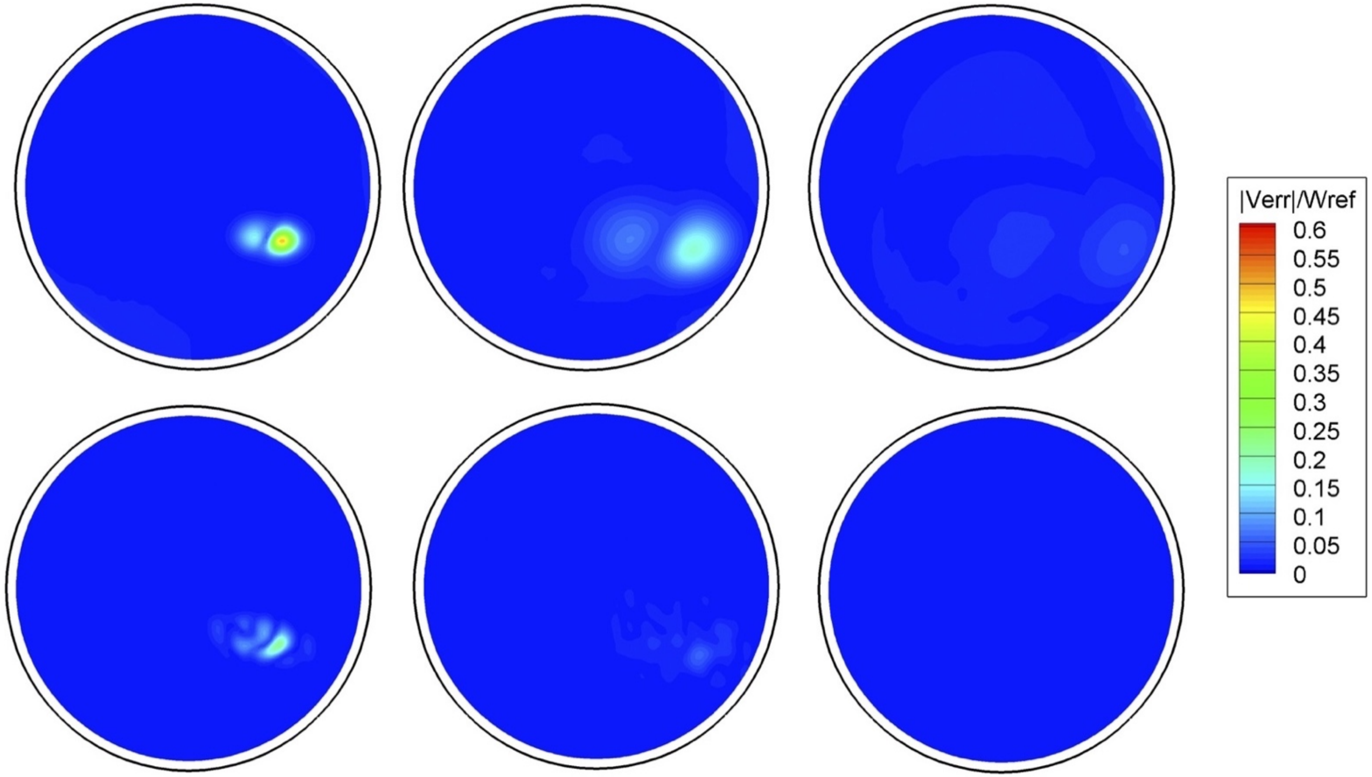

**Figure B.2:** Out-of-plane absolute velocity error. Distorted (first row) and corrected (second row) profiles for a = 48px, c = 48px, 128px, 256px.

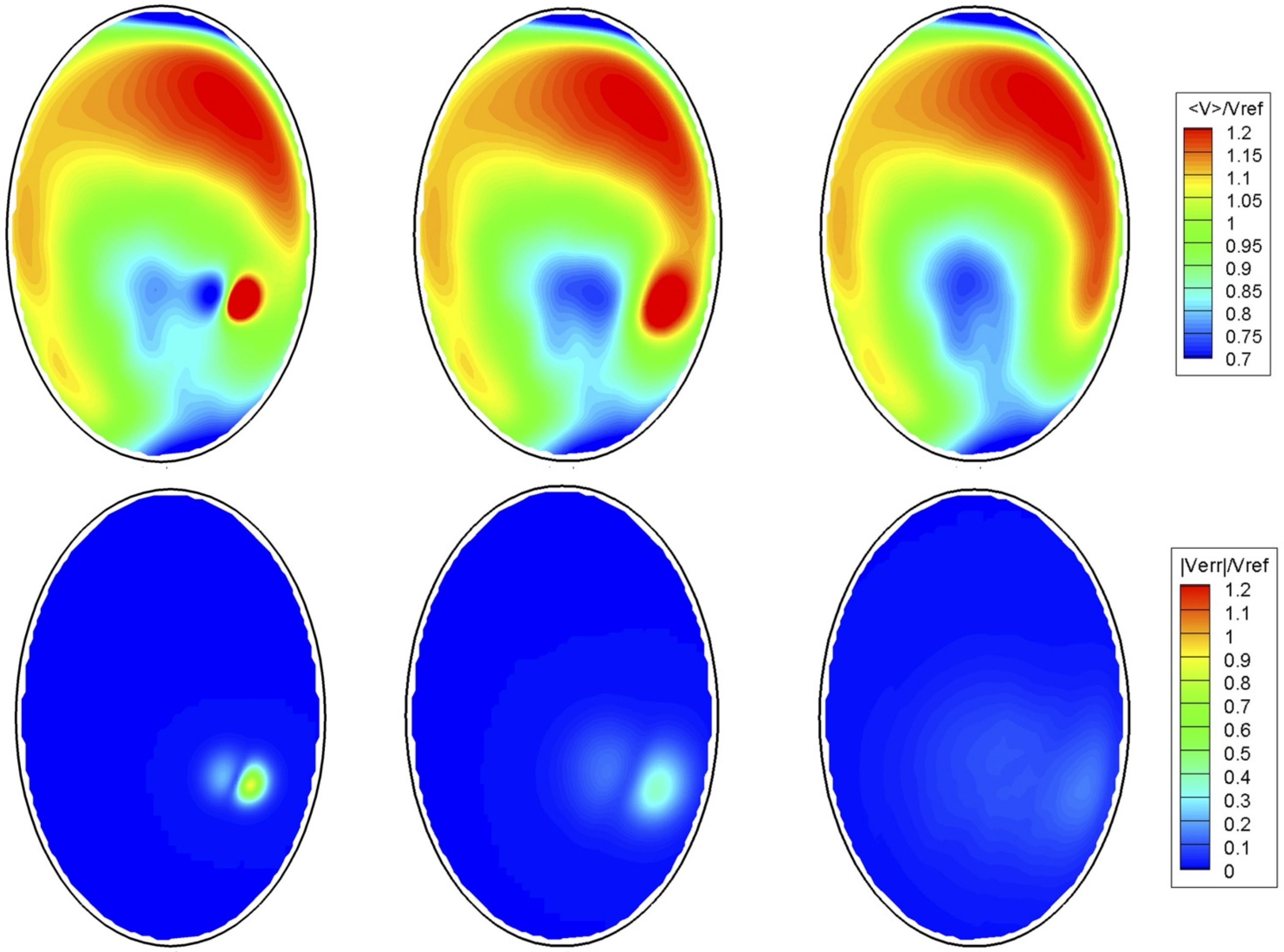

**Figure B.3:** First row, image-plane velocity profiles. Second row, image plane velocity error. Results for a = 48px, c= 64px, 128px, 256px